Structure function studies of the *Plasmodium berghei* circumsporozoite protein repeat region

by

Amanda Balaban

A dissertation submitted to The Johns Hopkins University

in conformity with the requirements for the degree of

Doctor of Philosophy

Baltimore, Maryland

May, 2018

Abstract

Malaria is caused by protozoan parasites of the genus, *Plasmodium*, and is responsible for the death of 400,000 children every year. Infection results from an infected mosquito bite, which transmits the sporozoite stage of *Plasmodium* into the skin, where the sporozoite migrates until finding a blood vessel which it actively enters to use the blood circulation to the liver and establish infection. Circumsporozoite protein (CSP) is a multi-functional protein that covers the sporozoite surface and is composed of three domains: an N-terminal domain, central repeat region, and a thrombospondin repeat type-1 (TSR) domain. Structure and/or function studies have elucidated some functionalities of the N-terminus and TSR domains, but no function has been described for the repeat region linking these two terminal domains. This is particularly surprising as the repeat region of CSP is the antibody target of the only malaria vaccine that has shown efficacy in Phase III clinical trials, RTS,S.

We sought to elucidate the function of the CSP repeat region through mutagenesis in the rodent model system, *Plasmodium berghei*. We replaced the endogenous *csp* locus with *csp* repeat mutations or deletions including: complete deletion of the repeat region, trunctations of the repeats, charge modifications, and a scrambled repeat sequence. Through these mutants we

found that the repeats play a critical role early in sporozoite development and motility, which is critical for infection of the liver. These studies are the first to show that the CSP repeat region has a functional role during sporozoite infection, thus expanding our knowledge of this promising vaccine target.

Thesis Committee

Primary Readers

Photini Sinnis (Primary Advisor)
Professor
Department of Molecular Microbiology and Immunology
Johns Hopkins Bloomberg School of Public Health

Michael J. Matunis
Professor
Department of Biochemistry and Molecular Biology
Johns Hopkins Bloomberg School of Public Health

Sean Prigge
Professor
Department of Molecular Microbiology and Immunology
Johns Hopkins Bloomberg School of Public Health

Douglas Robinson
Professor
Department of Cell Biology
Johns Hopkins School of Medicine

Alternate Readers

Marie Hardwick
Professor
Department of Molecular Microbiology and Immunology
Johns Hopkins Bloomberg School of Public Health

Brendan Cormack
Professor
Department of Molecular Biology and Genetics
Johns Hopkins School of Medicine

Valeria Culotta
Professor
Department of Biochemistry and Molecular Biology
Johns Hopkins Bloomberg School of Public Health

Acknowledgments

First and foremost I have to thank Dr. Photini Sinnis, my mentor and advisor, for all of the support and guidance she has provided throughout my dissertation. Photini has provided me with amazing opportunities and freedoms during this project to which I am extremely grateful. In addition to Photini, I have been fortunate enough to have several other mentors at Hopkins, including Drs. Fidel Zavala and Sean Prigge, who have been mentors to me since my first few months at Hopkins. Finally, I want to thank the rest of my committee, Drs. Douglas Robinson, Marie Hardwick, and Michael Matunis for being engaged in every one of my committee meetings and helping me develop my project.

To complete this project, required the support of several core facilities and staff at Hopkins. I am extremely grateful to Dr. Godfree Mlambo who ensured I had infected mosquitoes every week and was always accommodating to any last minute changes and to Chris Kizito who made sure we had lots of mosquitoes to do our experiments. The microscope facility at the School of Medicine helped establish the reflection interference contrast microscopy method, Imaris software analysis, and always made themselves available for help or advice. I am particularly grateful to Scot Kuo, Barbara Smith, and

Hoku West-Foyle.

For the intravital imaging project, I relied heavily on the help of staff at the NIH. Dr. Bertrand Lucotte taught me to use the 2-photon microscope and was immensely helpful in thinking about analysis. Dr. Joni Taylor helped me with all animal protocols and Dr. Brian Glancy was beyond generous in sharing his microscope. Finally, Dr. Robert Balaban, encouraged me to take on this project and was a motivating source throughout. Thank you all for being so welcoming!

A special thank you to Dr. Friedrich Frischknecht who consistently provided support on this project and helped me develop my ideas and analysis approaches. I am particularly grateful to Freddy for hosting me in his lab to learn new techniques for studying sporozoite motility.

Finally, thank you to all members of the Sinnis Lab, past and present, all of whom have directly or indirectly assisted in this project. Drs. Daniel Ragheb and Christine Hopp helped me get the project up and running and taught me almost everything I know. Dr. Melanie Shears helped with looking at oocyst phenotypes, Natasha Vartak and Jason Gregory performed immunofluorescence assays, and Ariadne Sinnis-Bourozikas assisted with live gliding assays.

Table of Contents

List of Tables

List of Figures

Chapter 1

Introduction

1.1 Life Cycle of the Malaria Parasite

Malaria is a disease caused by protozoan parasites of the genus, *Plasmodium*. The *Plasmodium* genus has over 100 different species, each of which has a tropism for a different vertebrate host species [1]. There are five species that infect humans, *Plasmodium falciparum, Plasmodium vivax, Plasmodium malariae, Plasmodium ovale,* and *Plasmodium knowlesi*.

All *Plasmodium* parasites cycle between mosquito and vertebrate hosts. When an *Anopheles* mosquito takes an infected blood meal, the sexual stages of *Plasmodium*, gametocytes, mate within the mosquito, eventually forming an ookinete, which traverses the epithelium of the mosquito gut, and forms an oocyst. Inside oocysts, sporozoites develop, then migrate out into the open circulatory system of the mosquito, the hemolymph, and a proportion of them actively invade the mosquito salivary glands. During feeding, the mosquito salivates into the dermis of a vertebrate host inoculating sporozoites into the skin. Here, sporozoites migrate within the skin until they find a blood

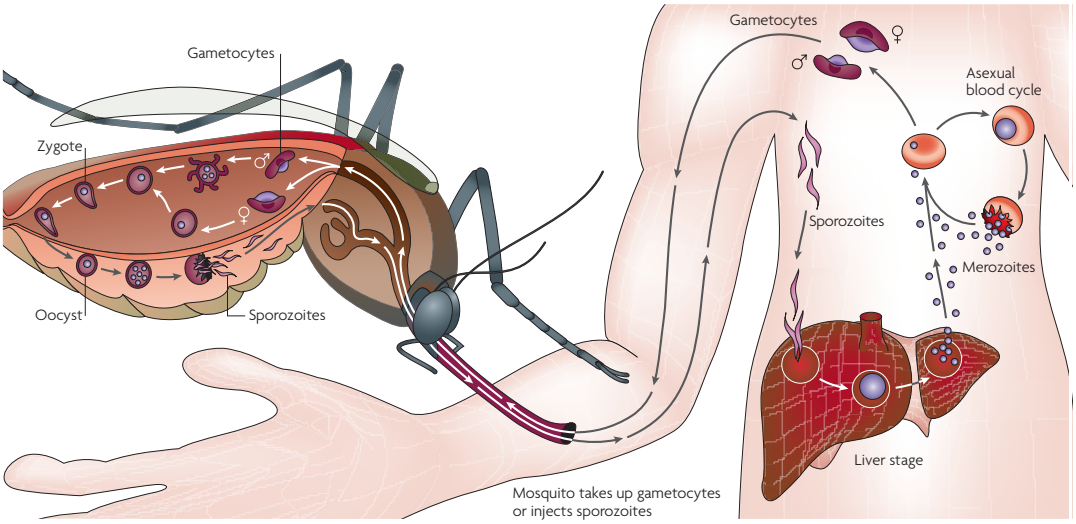

Figure 1.1: *Plasmodium* Life Cycle. Life cycle of the *Plasmodium* parasite. From Su *et al.* [2].

vessel, which they invade to traffic to the liver. Once in the liver, sporozoites actively invade hepatocytes, and develop into exoerythrocytic forms (EEFs) and undergo massive cellular division, resulting in thousands of progeny, merozoites, which are released into the circulatory system to initiate the asexual blood stage of infection. Iterative asexual replication cycles lead to high parasite numbers within the host leading to clinical symptoms. A small proportion of blood stage parasites will differentiate into gametocytes which will infect an *Anopheles* mosquito, continuing the life cycle. See Figure 1.1 for pictorial representation of the life cycle.

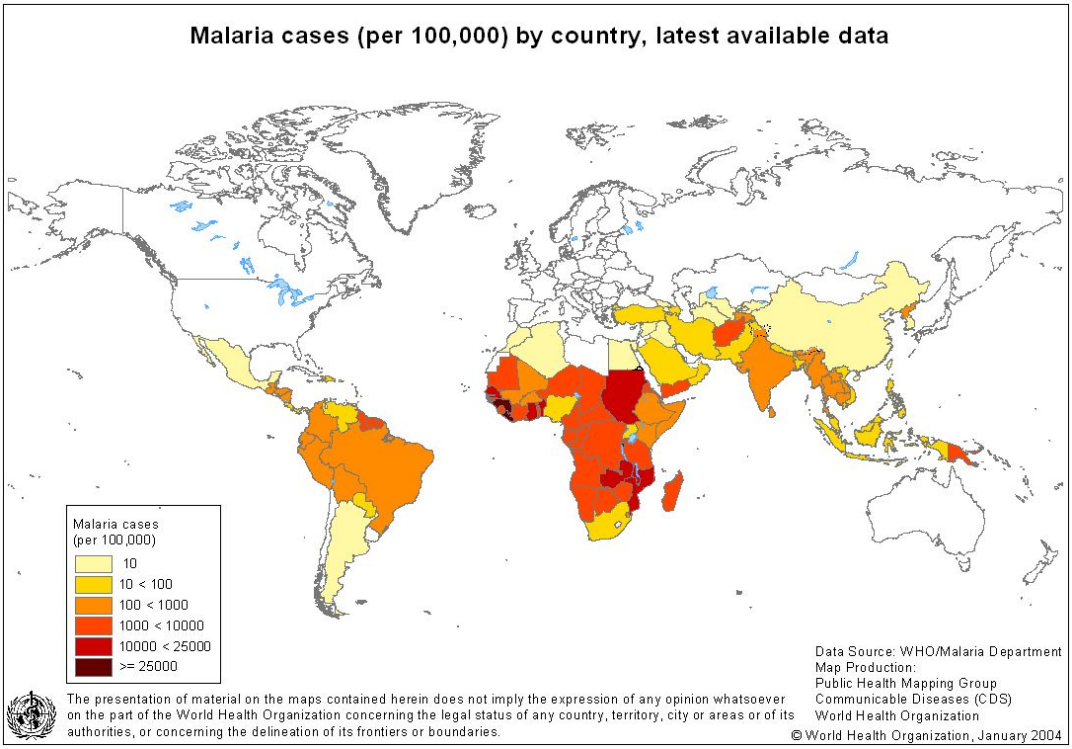

Figure 1.2: Malaria Cases per Country. Map of results of 2004 cross-sectional survey conducted by the WHO screening for evidence of infection.

1.2 Malaria: A Public Health Crisis

Malaria is a disease resulting from infection with *Plasmodium*. Every year there are 214 million new malaria cases and 445,000 deaths from malaria, the majority of whom are children in Sub-Saharan Africa (Figure 1.2) [3]. That correlates to a child dying every 71 seconds. The high burden of malaria calls for interventions, as no vaccine or long-term preventative treatments exist.

Current malaria control efforts include insecticide treated bed nets, indoor spraying of insecticides, and rapid diagnosis followed by drug treatment. These interventions have lead to an $\sim$60% decrease in malaria deaths since the year 2000 [3]. However, in order to remain effective, control efforts must be

maintained. Furthermore, field studies demonstrate that interventions have reached the limit of what is attainable in areas where malaria transmission is as intense as is found in Sub-Saharan Africa [4] (Figure 1.2). Vaccines present the best long term approach to malaria control and eventual eradication. Distinct vaccine efforts targeting pre-erythrocytic stages (sporozoites and EEFs), blood stages, and mosquito stages have been pursued. Thus far, the most traction has been made with pre-erythrocytic stages, likely due to the low number of parasites at these stages and little allelic variation.

The first successful efforts towards a malaria pre-erythrocytic vaccine were conducted in the 1960's and found that immunization with irradiated sporozoites could provide sterilizing protection in mice [5, 6], due to stimulation of both humoral and cell mediated immunity [7, 8]. The primary target of these protective responses was found to be the circumsporozoite protein (CSP), the major sporozoite surface protein [9–11]. These studies paved the way for the development of the only malaria vaccine in Phase III clinical trials, RTS,S. RTS,S is a fusion protein of the hepatitis B surface antigen and two domains within CSP: a repeat region which contains the immunodominant antibody epitope and the carboxy-terminus containing T-cell epitopes found on infected hepatocytes [12].

The Phase III clinical trial with RTS,S was performed in two age groups (5-17 month olds and 6-12 week olds), and in 7 countries with a range of endemicity [13]. Efficacy was measured as protection from preventing clinical symptoms or severe disease. The results of this trial showed that vaccination with RTS,S conferred 30-50% protection from malaria symptoms and 40-45%

protection from severe disease with the vaccine showing stronger efficacies in the older age group one year after vaccination [13]. However, following the first year after vaccination, protection declines, and at four years vaccine efficacy is half that of the one year efficacy against symptoms, with no protection against severe malaria [13]. Vaccine efficacy could be enhanced, with an additional booster [13], however improvements must be made to produce stronger, longer lasting protective immune responses. A better understanding of the function of CSP and its role in sporozoite biology could rationally guide the design of future vaccine candidates.

1.3 Sporozoite Biology

1.3.1 Cell Biology

The sporozoite stage is a crescent shaped cell measuring 10-12 μm in length by 1 μm in width [14, 15]. In addition to the canonical structures of eukaryotic cells, sporozoites also contain unique structures: apical organelles called rhoptries and micronemes, an apical ring, the inner membrane complex (IMC), and the subpellicular network (Figure 1.3).

These unique cellular structures have evolved to optimize sporozoite migration in its hosts. The apical organelles, rhoptries and micronemes, release their contents during parasite motility. Micronemes house adhesive proteins involved in parasite motility, which is required for migration, invasion, and egress. In addition to the micronemes, rhoptry proteins mediate invasion through modulation of host cell membranes. For productive motility, adhesins released from micronemes must interact through adaptor proteins with

the IMC, a series of flattened vesicles underlying the plasma membrane. The side of the IMC facing the plasma membrane houses the actin-myosin motor complex responsible for parasite motility [16, 17], while the cytoplasmic side of the IMC is tethered to the cytoskeleton. The sporozoite cytoskeleton is composed of a subpellicular network of intermediate filaments and microtubules. The subpellicular network consists of intermediate filaments which maintain sporozoite shape and provide an anchor for the IMC, a critical feature for sporozoite motility [18–20]. In *Plasmodium berghei*, a rodent malaria parasite, 15-16 microtubules are anchored at the apical ring and extend two-thirds the length of the sporozoite, forming a protective cage around apical organelles, with one microtubule extending the full body length [21, 22]. The apical ring is also where the apical organelles release their contents during parasite gliding, and in *P. berghei* sporozoites the apical ring is tilted towards the substrate surface, suggesting directed secretory organelle release [15, 18]. While unique cellular structures have been identified and partially characterized, their functions and molecular components need to be further elucidated.

1.3.2 Sporozoite Motility

Motility of *Plasmodium* sporozoites is critical for infectivity in both mosquito and vertebrate hosts, as sporozoites actively migrate within the body of these organisms and actively invade host cells. Sporozoites utilize a substrate-dependent form of motility, called gliding motility, which does not involve cell shape change or locomotory organelles, such as flagella [24]. Forces enabling sporozoite motility are generated through adhesins, which link to

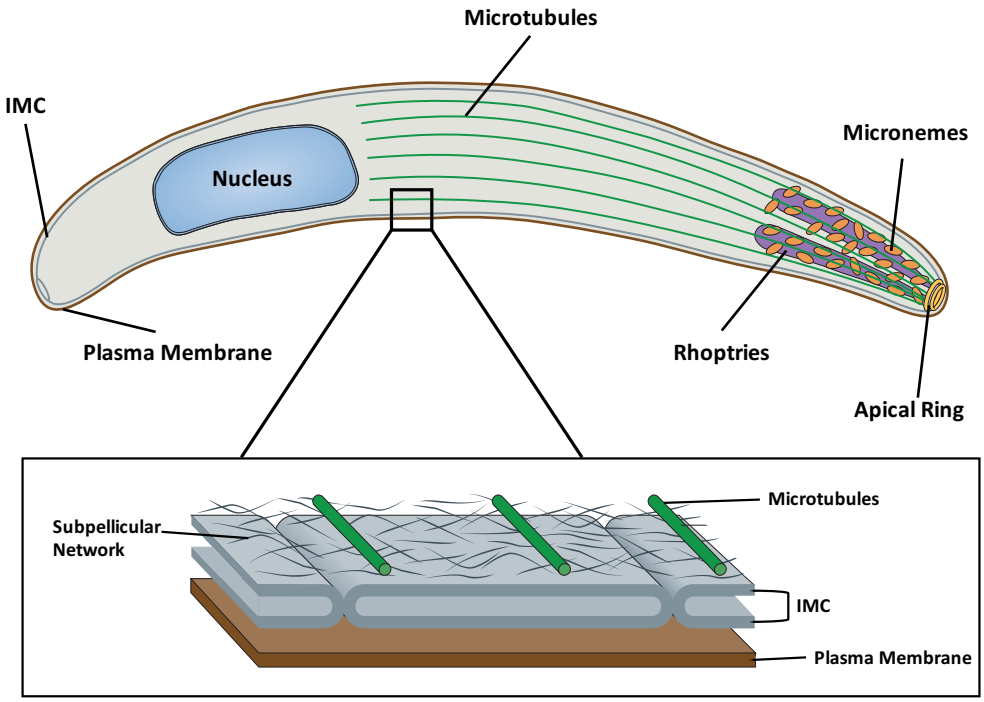

Figure 1.3: ***Plasmodium*** **Sporozoite Cellular Architecture.** Inner membrane complex (IMC) (blue), apical polar ring (yellow), microtubules (green), rhoptries (purple), and micronemes (orange). Blown up view of the IMC boxed below the sporozoite for more detail on cytoskeleton and IMC. Adapted from Frénal *et al.* [23].

the actin-myosin motor complex through adaptor proteins (Figure 1.4). As engaged myosins pull adhesins posteriorly, the sporozoite is pushed forward (Figure 1.4) [16, 24]. In this manner, sporozoites generate adhesion sites that they move over as they glide. Adhesion sites then disassemble as they reach the posterior end of the sporozoite, while new adhesion sites assemble at the apical end [25]. In this way, sporozoites average extraordinary speeds of 1.5-2 μm per second or 12 body lengths per minute. To achieve these extraordinary speeds adhesion site dynamics must be effectively regulated.

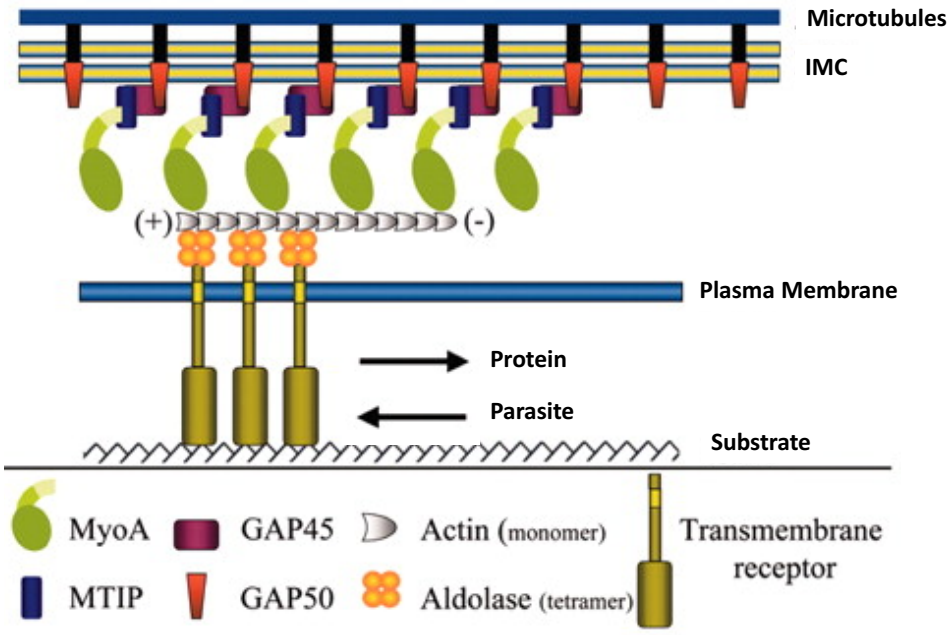

Figure 1.4: Motor Complex of *Plasmodium*. Cartoon of the predicted topology of the *Plasmodium* motor complex adpated from Bosch *et al.* [26]. Extracellular domains of a transmembrane protein (i.e. TRAP) interacts with the substrate. The cytoplasmic tail of the transmembrane protein interacts with aldolase, an actin binding protein, linking extracellular ligands to the actin-myosin motor. The MyoA head binds to actin filaments, and is linked to the IMC through adaptor proteins: MTIP, GAP45, and GAP50. An unidentified, but visualized protein, links the IMC to microtubules and the cytoskeleton of the sporozoite. MyoA pulls engaged actin rearwards, along with aldolase and the transmembrane protein, pushing the sporozoite forward.

The sporozoite's motility machinery matures as it progresses through its life cycle in the mosquito [18, 27]. Sporozoites isolated from the oocysts or hemolymph of infected mosquitoes predominately move in non-productive forms of gliding, patch gliding or waving [28–30]. These motility behaviors result in no displacement of the sporozoite or turn over of adhesion sites [25]. However, once in the salivary glands, the majority of sporozoites exhibit productive gliding motility [28–30], perhaps in part due to the development of the subpellicular network [18, 19]. Though salivary gland sporozoite motility machinery is fully mature, sporozoites exhibit little motility in the acinar cell of the salivary glands or its secretory cavity [31]. However, upon inoculation into the vertebrate host, sporozoites become activated to move at extraordinary speeds [32]. The signals leading to the activation of motility are not known, though studies have shown that albumin and the presence of a substrate are important [33, 34]. Once activated, intracellular calcium stores are released leading to microneme secretion and deposition of proteins required for productive parasite motility [35].

Thrombospondin related anonymous protein (TRAP) is the most abundant secreted protein and is essential for sporozoite motility [36]. TRAP is a transmembrane protein with extracellular adhesion domains: an A-domain (an adhesive motif found in integrins) and a thrombospondin type 1 domain (TSR) [37]. TRAP is localized to the micronemes [38] and upon intracellular calcium signaling, is released onto the sporozoite plasma membrane [39], where it links the sporozoite's molecular motor to the substrate [40]. During sporozoite motility, TRAP is released anteriorly, where it likely forms an adhesion

site which the sporozoite translocates over with TRAP being cleaved at the posterior end of the sporozoite by a rhomboid protease [41]. Without TRAP, sporozoites are only capable of non-productive motility [36], suggesting that TRAP is not essential for initial attachments, but is critical for adhesion site turn over and maturation.

Sporozoite motility has been probed using both *in vitro* and *in vivo* studies, each with their own strengths and limitations. Most of the work on sporozoite motility has been conducted *in vitro*, and consists of imaging their motility on artificial substrates, such as glass, polyethylene glycol (PEG), matrigel, and gold [25, 42–44]. In 2D assays, sporozoites move in circles. The relevance of this circular motility behavior to *in vivo* motility is unclear, however, it correlates to productive motility *in vivo* [32]. In the 3D environment of tissues, this circular motility has been hypothesized to translate to corkscrewing through the tissue and/or replicate circling around blood vessels. The data and insight gained from these *in vitro* studies have greatly expanded our knowledge of the mechanism by which sporozoites move.

In the skin, sporozoites must move within the dermis to find blood vessels and enter the circulation, a process that can occur within minutes of their inoculation, or take 1-2 hours [45]. Methods for imaging at this stage have largely consisted of spinning-disk confocal imaging in the skin of mice after an infected mosquito bite or intradermal inoculation of sporozoites. Using a mosquito to inoculate sporozoites is the most physiologically relevant mechanism of sporozoite inoculation, but is technically difficult. Controlling for the time between inoculation and locating the bite site for imaging prevents

acquisition of parasite behavior immediately following inoculation. Several groups have imaged sporozoites inoculated by mosquito bite or needle and together, these studies have demonstrated: 1) sporozoites move at similar speeds *in vivo* to that observed *in vitro*, 2) sporozoites exhibit more linear motility behavior in the dermis then that observed in *in vitro*, and 3) parasite motility behavior is altered due to *in vivo* environmental changes such as anatomical location or proximity to blood vessels [32, 46, 47].

1.3.3 The Circumsporozoite Protein (CSP)

The circumsporozoite protein (CSP) was first discovered as the target of protective antibodies generated after vaccination with irradiated sporozoites [9]. Subsequent studies showed that these antibodies targeted the central repeat region of CSP, leading to the shedding of CSP in a precipitation-like reaction and immobilization of the sporozoite [48, 49].

CSP structure is conserved among all *Plasmodium* species and is composed of three domains: an N-terminal domain, a central tandem amino acid repeat region, and a type-1 thrombospondin repeat (TSR) domain in the C-terminus (Figure1.5) [50]. Additionally, CSP has a conserved proteolytic cleavage site, Region I, between the N-terminal domain and repeat region (Figure 1.5) [51]. Although it has never been definitively proven, CSP is predicted to be GPI-anchored to the sporozoite surface. Many groups have attempted to ascertain the structure of CSP but [52, 53] crystallization of full length CSP has been unsuccessful. Nonetheless, three crystallization attempts of isolated segments of CSP have been achieved: 1) one repeat-unit [54], 2) three repeat-units

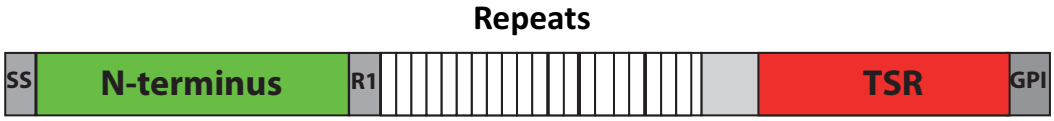

Figure 1.5: Schematic of CSP. SS = signal sequence, RI = Region I, TSR = thrombospondin-type I repeat domain, , GPI = glycosyl phosphatidylinositol anchor sequence.

binding to FAb monomers [55] and 3) the TSR domain [53]. Both crystal structures of the repeats demonstrate a β-turn conformation [54, 55] and that of the TSR domain demonstrated an unexpected hydrophobic pocket and as well as N- and C-terminal domains that are in close proximity to one another [53].

Mutagenesis of the *csp* gene in the parasite has proven to be a reliable approach to elucidating its function. Deleting the gene gave rise to parasites that do not make sporozoites, showing that CSP is essential for sporozoite development [56]. Subsequent studies have shown that C-terminal elements, namely the GPI-anchor sequence and charged region of the TSR, are also critical in sporozoite budding and development, as well as exit from oocysts [57, 58]. Other CSP mutations have not shown sporozoite development impairment, suggesting that it is the C-terminus and membrane organization of CSP which is critical for sporozoite development in the oocyst [50]. Within the oocyst, the TSR domain is exposed and N-terminal domain is masked [50]. However, once sporozoites leave the oocysts, there is a switch in domain exposure, with the N-terminal domain exposed and the TSR domain masked, as determined by immunofluorescence assays [50]. Once out of the oocysts, sporozoites must migrate to the salivary glands. Recombinant peptide work

has suggested that Region-I and its flanking amino acids can specifically bind to salivary glands, implicating CSP in salivary gland targeting [59]. The molecular nature of this interaction, however, is unknown. Once in the salivary glands, CSP is maintained in the conformation with N-terminal exposure and TSR masking until reaching the liver, where the N-terminus is cleaved and the TSR is exposed [50].

Studies of sporozoites in the skin is limited, but work from our lab has investigated the role of the N-terminus of CSP during the skin phase of sporozoite infection. Importantly, when the N-terminus is deleted, the TSR becomes exposed during phases of sporozoite migration in which it is normally masked [50]. These studies have shown that in the absence of the N-terminus, sporozoites do not exit the skin [50]. Intravital imaging of the N-terminal mutants in the skin, showed that these sporozoites move slower in the skin and spend more time on blood vessels but exhibited significantly fewer blood vessel invasion events [32]. Together, these data suggest that the TSR is an adhesive motif, masked during migration in the skin to permit fast motility and invasion of blood vessels.

After invasion of a blood vessel, sporozoites must traffic to the liver, which is likely mediated by CSP-heparan sulfated proteoglycans (HSPGs) interactions [60]. HSPGs of the liver are more highly sulfated than those of other tissues, and work with recombinant proteins, peptides, and sporozoites, suggests that CSP specifically binds HSPGs [60–64]. The TSR of CSP was believed to be the HSPG binding partner, until a recombinant, folded TSR domain exhibited no heparan binding activity [53]. Nonetheless, a hydrophobic pocket

was discovered in the crystal structure of the TSR domain, which might provide a binding site for another hepatic receptor [53]. Further studies have demonstrated that upon interaction with hepatocytes, the N-terminus of CSP is cleaved by a parasite protease, exposing the TSR, likely priming the sporozoite for hepatocyte invasion [50, 51].

Thus far, the best approach to studying CSP domain activity has been through parasite mutagenesis with targeted modifications to CSP. Though these studies have elucidated the roles of the N- and TSR domains of CSP, the role of the central repeat region remains unknown, despite being the epitope of protective antibodies and the RTS,S vaccine.

References

1. CDC. *Malaria* <https://www.cdc.gov/malaria/about/.html> (2016).
2. Su, X., Hayton, K. & Wellems, T. E. Genetic linkage and association analysis for trait mapping in Plasmodium falciparum. *Nature Reviews Genetics* **8,** 497–506 (2007).
3. WHO. *Malaria* <http://www.who.int/malaria/media/en/> (2017).
4. WHO. *World Malaria Report* (WHO, Geneva, Switzerland, 2017).
5. Nussenzweig, R. S., Vanderberg, J., Most, H. & Orton, C. Protective Immunity Produced by the Injection of X-irradiated Sporozoites of Plasmodium berghei. *Nature* **216,** 160–162 (1967).
6. R. S. Nussenzweig, R., Vanderberg, J. P., Most, H. & Orton, C. Specificity of protective immunity produced by x-irradiated Plasmodium berghei sporozoites. *Nature* **222,** 488–489 (1969).
7. Nussenzweig, R. S., Vanderberg, J. P., Y.Sanabria & Most, H. Plasmodium berghei: Accelerated Clearance of Sporozoites from Blood as part of Immune-Mechanism in Mice. *Experimental Parasitology* **31,** 88–97 (1972).
8. Spitalny, G. L., Verhave, J. P., Th.Meuwiseen, J. H. E. & Nussenzweig, R. S. Plasmodium berghei : T Cell Immunity Dependence of Sporozoite-Induced in Rodents. *Experimental Parasitology* **42,** 73–81 (1977).
9. Yoshida, N., Nussenzweig, R. S., Potocnjak, P., Nussenzweig, V. & Aikawa, M. Hybridoma produces protective antibodies directed against the sporozoite stage of malaria parasite. *Science* **207,** 71–73 (1980).
10. Schofield, L. *et al.* γ Interferon, CD8+ T cells and antibodies required for immunity to malaria sporozoites. *Nature* **330,** 664 (1987).
11. Romero, P. *et al.* Cloned cytotoxic T cells recognize an epitope in the circumsporozoite protein and protect against malaria. *Nature* **341,** 323 (1989).

12. Casares, S., Brumeanu, T. D. & Richie, T. L. The RTS,S malaria vaccine. *Vaccine* **28,** 4880–4894 (2010).

13. WHO. Background paper on the RTS, S/AS01 malaria vaccine (2015).

14. Vanderberg, J., Rdodin, J. & Yoeli, M. Electron microscopic and histochemical studies of sporozoite formation in Plasmodium berghei. *Journal of Eukaryotic Microbiology* **14,** 82–103 (1967).

15. Niz, M. D. *et al.* Progress in imaging methods: insights gained into Plasmodium biology. *Nature Reviews Microbiology* **15,** 37–54 (2017).

16. Baum, J., Gilberger, T. W., Frischknecht, F. & Meissner, M. Host-cell invasion by malaria parasites: insights form Plasmodium and Toxoplasma. *Trends in Parasitology* **24,** 557–563 (2008).

17. Mann, T. & Beckers, C. Characterization of the subpellicular network, a filamentous membrane skeletal component in the parasite Toxoplasma gondii. *Molecular and Biochemical Parasitology* **115,** 257–268 (2001).

18. Kudryashev, M. *et al.* Structural basis for chirality and directional motility of Plasmodium sporozoites. *Cellular Microbiology* **14,** 1757–1768 (2012).

19. Khater, E. I., Sinden, R. & Dessens, J. T. A malaria membrane skeletal protein is essential for normal morphogenesis, motility, and infectivity of sporozoites. *Journal of Cell Biology* **167,** 425–432 (2004).

20. Tremp, A. Z. & Dessens, J. T. Malaria IMC1 membrane skeleton proteins operate autonomously and participate in motility independently of cell shape. *Journal of Biological Chemistry* **286,** 5383–5391 (2011).

21. Vanderberg, J., Rdodin, J. & Yoeli, M. Electron microscopic and histochemical studies of sporozoite formation in Plasmodium berghei. *Journal of Eukaryotic Microbiology* **14,** 82–103 (1967).

22. Cyrklaff, M. *et al.* Cryoelectron tomography reveals periodic material at the inner side of subpellicular microtubules in apicomplexan parasites. *Journal of Experimental Medicine* **204,** 1281–1287 (2007).

23. Frénal, K., Dubremetz, J., Lebrun, M. & Soldati-Favre, D. Gliding motility powers invasion and egress in Apicomplexa. *Nature Reviews Microbiology* **15,** 645 (2017).

24. Heintzelman, M. B. Cellular and Molecular Mechanics of Gliding Locomotion in Eukaryotes. *International Review of Cytology* **251,** 79–129 (2006).

25. Münter, S. *et al.* Plasmodium sporozoite motility is modulated by the turnover of discrete adhesion sites. *Cell Host & Microbe* **6,** 551–562 (2009).

26. Bosch, J. *et al.* Structure of the MTIP–MyoA complex, a key component of the malaria parasite invasion motor. *Proceedings of the National Academy of Sciences* **103,** 4852–4857 (2006).

27. Khater, E. I, Sinden, R. E. & Dessens, J. T. A malaria membrane skeletal protein is essential for normal morphogenesis, motility, and infectivity of sporozoites. *Journal of Cell Biology* **167,** 425–432 (2004).

28. Hegge, S. *et al.* Multistep adhesion of Plasmodium sporozoites. *The FASEB Journal* **24,** 2222–2234 (2010).

29. Vanderberg, J. P. Studies on the motility of Plasmodium sporozoites. *Journal of Eukaryotic Microbiology* **21,** 527–537 (1974).

30. Hegge, S., Kudryashev, M., Smith, A. & Frischknecht, F. Automated classification of Plasmodium sporozoite movement patterns reveals a shift towards productive motility during salivary gland infection. *Biotechnology Journal* **4,** 903–913 (2009).

31. Amino, R. *et al.* Quantitative imaging of Plasmodium transmission from mosquito to mammal. *Nature medicine* **12,** 220 (2006).

32. Hopp, C. S. *et al.* Longitudinal analysis of Plasmodium sporozoite motility in the dermis reveals component of blood vessel recognition. *eLife* **4,** e07789 (2015).

33. Kebaier, C. & Vanderberg, J. P. Initiation of Plasmodium sporozoite motility by albumin is associated with induction of intracellular calcium signaling. *International Journal for Parasitology* **40,** 25–33 (2010).

34. Perschmann, N., Hellmann, J. K., Frischknecht, F. & Spatz, J. P. Induction of malaria parasite migration by synthetically tunable microenvironments. *Nano Letters* **11,** 4468–4474 (2011).

35. Carey, A. F. *et al.* Calcium dynamics of Plasmodium berghei sporozoite motility. *Cellular Microbiology* **16,** 768–783 (2014).

36. Sultan, A. A. *et al.* TRAP is necessary for gliding motility and infectivity of Plasmodium sporozoites. *Cell* **90,** 511–522 (1997).

37. Kappe, S. H., Buscaglia, C. A. & Nussenzweig, V. Plasmodium sporozoite molecular cell biology. *Annual Review of Cell and Developmental Biology* **20,** 29–59 (2004).

38. Rogers, W. O. *et al.* Characterization of Plasmodium falciparum sporozoite surface protein 2. *Proceedings of the National Academy of Sciences* **89,** 9176–9180 (1992).

39. Gantt, S. *et al.* Antibodies against thrombospondin-related anonymous protein do not inhibit Plasmodium sporozoite infectivity in vivo. *Infection and Immunity* **68,** 3667–3673 (2000).

40. Buscaglia, C. A., Coppens, I., Hol, W. G. J. & Nussenzweig, V. Sites of interaction between aldolase and thrombospondin-related anonymous protein in Plasmodium. *Molecular Biology of the Cell* **14,** 4947–4957 (2003).

41. Ejigiri, I. *et al.* Shedding of TRAP by a rhomboid protease from the malaria sporozoite surface is essential for gliding motility and sporozoite infectivity. *PLoS Pathogens* **8,** e1002725 (2012).

42. Perschmann, N., Hellmann, J. K. & Spatz, F. F.J. P. Induction of malaria parasite migration by synthetically tunable microenvironments. *Nano letters* **11,** 4468–4474 (2011).

43. Akaki, M. & Dvorak, J. A. A chemotactic response facilitates mosquito salivary gland infection by malaria sporozoites. *Journal of Experimental Biology* **208,** 3211–3218 (2005).

44. Amino, R. *et al.* Host cell traversal is important for progression of the malaria parasite through the dermis to the liver. *Cell Host & Microbe* **3,** 88–96 (2008).

45. Yamauchi, L. M., Coppi, A., Snounou, G. & Sinnis, P. Plasmodium sporozoites trickle out of the injection site. *Cellular Microbiology* **9,** 1215–1222 (2007).

46. Amino, R. *et al.* Quantitative imaging of Plasmodium transmission from mosquito to mammal. *Nature Medicine* **12,** 220 (2006).

47. Hellmann, J. K. *et al.* Environmental constraints guide migration of malaria parasites during transmission. *PLoS Pathogens* **7,** e1002080 (2011).

48. Zavala, F., Cochrane, A. H., E. H, N., Nussenzweig, R. S. & Nussenzweig, V. Circumsporozoite proteins of malaria parasites contain a single immunodominant region with two or more identical epitopes. *Journal of Experimental Medicine* **157,** 1947–1957 (1983).

49. Cochrane, A. H., Aikawa, M., Jeng, M. & Nussenzweig, R. S. Antibody-induced ultrastructural changes of malarial sporozoites. *The Journal of Immunology* **116,** 859–867 (1976).

50. Coppi, A. *et al.* The malaria circumsporozoite protein has two functional domains, each with distinct roles as sporozoites journey from mosquito to mammalian host. *Journal of Experimental Medicine* **208,** 341–356 (2011).

51. Coppi, A., Pinzon-Ortiz, C., Hutter, C. & Sinnis, P. The Plasmodium circumsporozoite protein is proteolytically processed during cell invasion. *The Journal of Experimental Medicine* **201,** 27–33 (2005).

52. Plassmeyer, M. L. *et al.* Structure of the Plasmodium falciparum circumsporozoite protein, a leading malaria vaccine candidate. *Journal of Biological Chemistry* **284,** 26951–26963 (2009).

53. Doud, M. B. *et al.* Unexpected fold in the circumsporozoite protein target of malaria vaccines. *Proceedings of the National Academy of Sciences* **109,** 7817–7822 (2012).

54. Ghasparian, A., Moehle, K., Linden, A. & Robinson, J. A. Crystal structure of an NPNA-repeat motif from the circumsporozoite protein of the malaria parasite Plasmodium falciparum. *Chemical Communications* **2,** 174–176 (2006).

55. Oyen, D. *et al.* Structural basis for antibody recognition of the NANP repeats in Plasmodium falciparum circumsporozoite protein. *Proceedings of the National Academy of Sciences,* 201715812 (2017).

56. Menard, R. *et al.* Circumsporozoite protein is required for development of malaria sporozoites in mosquitoes. *Nature* **385,** 336 (1997).

57. Wang, Q., Fujioka, H. & Nussenzweig, V. Mutational analysis of the GPI-anchor addition sequence from the circumsporozoite protein of Plasmodium. *Cellular Microbiology* **7,** 1616–1626 (2005).

58. Wang, Q., Fujioka, H. & Nussenzweig, V. Exit of Plasmodium Sporozoites from Oocysts Is an Active Process That Involves the Circumsporozoite Protein. *PLoS Pathogens* **1,** 72–79 (2005).

59. Sidjanski, S. P., Vanderberg, J. P. & Sinnis, P. Anopheles stephensi salivary glands bear receptors for region I of the circumsporozotie protein of Plasmodium falciparum. *Molecular and Biochemical Parasitology* **90,** 33–41 (1997).

60. Coppi, A. *et al.* Heparan sulfate proteoglycans provide a signal to Plasmodium sporozoites to stop migrating and productively invade host cells. *Cell Host and Microbe* **2,** 316–327 (2007).

61. Pancake, S. J., Holt, G. D., Mellouk, S. & Hoffman, S. L. Malaria sporozoites and circumsporozoite proteins bind specifically to sulfated glycoconjugates. *The Journal of Cell Biology* **117,** 1351–1357 (1992).

62. Frevert, U. *et al.* Malaria circumsporozoite protein binds to heparan sulfate proteoglycans associated with the surface membrane of hepatocytes. *The Journal of Experimental Medicine* **177,** 1287–1298 (1993).

63. Rathore, D. *et al.* Direct measurement of the interactions of glycosaminoglycans and a heparin decasaccharide with the malaria circumsporozoite protein. *Biochemistry* **40,** 11518–11524 (2001).

64. Ancsin, J. B. & Kisilevsky, R. A Binding Site for Highly Sulfated Heparan Sulfate Is Identified in the N Terminus of the Circumsporozoite Protein: Significance for malaria sporozoite attachment to hepatocytes. *Journal of Biological Chemistry* **279,** 21824–21832 (2004).

Chapter 2

The Repeat Region of the Circumsporozoite Protein is Critical for Sporozoite Motility and Infectivity

2.1 Introduction

Antibodies specific for the repeat region of CSP can protect from infection [1], but we know little about the role of the repeat region in sporozoite biology. The repeat region of CSP consists of tandem amino acid repeats that vary among *Plasmodium* species (Table 2.1) [2]. Interestingly, the repeats of different *Plasmodium* species are exchangeable, with no observable phenotype, as has been shown through chimeric parasite lines [3, 4]. These data suggest that the repeats have a conserved function across species despite variant sequences.

Comparison of the CSP repeats from different *Plasmodium* species demonstrated that this region has a conserved pI, between 3-4, and is composed of a subset of amino acids, with 80-90% of the residues being a combination of

proline, glycine, alanine, asparagine or occasionally glutamine. Negatively charged amino acids, aspartic acid and glutamic acid, are always present in the repeats, providing the conserved negative pI. Interestingly, when negatively charged residues comprise greater than ∼10% of the region, positively charged residues are present (lysine and arginine). Finally, valine is occasionally observed in low abundance. We hypothesized that these features of the repeat region are crucial for sporozoite biology and protein function.

Previous studies on CSP repeat structure have been conducted using recombinant CSP repeats. These studies have indicated the repeats may form a β-turn confirmation [5–9]. Additionally, two features may coordinate repeat conformation: 1) the flanking of the repeats with hydrophobic domains (as is the case on full length CSP) [10] and 2) the binding of calcium to the repeats [9, 11]. However, because these studies have been conducted on recombinant peptides, not full length protein, and no functional assays exist for CSP to confirm proper folding, the consensus in the field has been that the repeats are a disordered, non-functional region. We sought to probe the function of native CSP in the parasite by making parasites with truncated or altered repeats.

We generated a panel of mutant parasite lines in the rodent model system, *Plasmodium berghei*. First we deleted the repeats entirely, ΔRep, and found severe defects in sporozoite development within the mosquito, with few sporozoites fully developing but never leaving the oocyst [12]. Early stages of sporogony in ΔRep showed no obvious defects by electron microscopy, however at later stages, sporozoites underwent cell death [12]. It is likely that deletion of the repeats leads to misfolding of CSP such that sporozoites do

Mammalian Host	Genius Species	CSP Repeat Sequence
Human	***Plasmodium falciparum***	GDGNPDP NANP NVDP NANP NVDP NANP NANP NANP NANP NANP NANP NANP NANP NANP NANP NANP NANP NANP NVDP NANP NANP NANP NANP NANP NANP NANP NANP NANP NANP NANP NANP NANP NANP NANP NANP NANP NANP NANP NANP NANP NANP NANP NANP NANP N
	Plasmodium vivax	EDGAGNQP GANGAGNQP GTNGAGNQP GANGAGNQP GANGADDQP GANGAGNQP GANGAGNQP GANGAGNQP GANGAGDQP GANGAGNQP GANGAGNQP GANGAGNQP GANGAGNQP GANGAGNQP GANGAGNQP GANGAGNQP GANGAG
	Plasmodium malariae	PGDDDGAG NDAG NDAG NDAG NAAG NAAG NAAG NAAG NAAG NAAG NAAG NAAG NAAG NAAG NDAG NAAG NAAG NAAG NAAG NAAG NDAG NAAG NAAG NAAG NAAG NAAG NAAG NAAG NAAG NAAG NAAG NDAG NAAG NAAG NAAG NAAG NAAG NAAG NAAG NAAG NAAG NAAG NAAG NAAG NAAG NAAG NAAG NAAG NAAG NAAG NAAG NAAG NAAG NAAG
	Plasmodium ovale	EREND PPAPQGEGN PPAPQGEGN PPAPQGEGN PPAPQGEGN PPAPQGEGN PPAAQGEGN PPAAQGNGN PPAAQGNGN PPAAQGNGN PPAPA
Rodent	***Plasmodium berghei***	PPPP NPNDPPPP NPNDPPPP NPNDPPPP NPNDPAPP NANDPAPP NANDPAPP NANDPAPP NANDPAPP NANDPAPP NANDPAPP NANDPPPP NPNDPAPP QGNNN PQPQ PRPQ PQPQ PQPQ PQPQ PQPQ PRPQ PQPQ P
	Plasmodium yoelii	VVADENVDQ GPGAPQ GPGAPQ GPGAPQ GPGAPQ GPGAPQ GPGAPQ GPGAPQ GPGAPQ GPGAPQ GPGAPQ GPGAPQ GPGAPQ GPGAPQ GPGAPQ GPGAPQ E PPQQ PPQQ PPQQ PPQQ PPQQ PPQQ PPQQ P
	Plasmodium chabaudi	GGQGGQ GVQGDQ GGQGVQ GDQGGQ GVQGDQ GGQGVQ GDQGGQ GVQGDQ GGQGVQ GDQGGQ GVQGDQ GGQGVQ GDQGGQ GVQGDQ GGQGGQ GGQGAQ GAQGGQ GGQGVQ GDQGGQ GGQGGQ GGQGGQ GGQGGQ GDQGAQ GADGNRAPVVPAAPGGGG
Non-Human Primate	***Plasmodium knowlsei***	PNE GQPQAQGDGANA GQPQAQGDGANA GQPQAQGDGANA GQPQAQGDGANA GQPQAQGDGANA GQPQAQGDGANA GQPQAQGDGANA GQPQAQGDGANA GQPQAQGDGANA GQPQAQGDGANA GQPQAQGDGANA GQPQAQGDGANA GQPQAQGDGANV PRQGRNGGGAPA
	Plasmodium cynomolgi	VENADG NAGG NAGG NAGG NAGG NAGG NADG NAGG NAGG NAGG NAGG NAGG NADG NAGG NAGG NAGG NADG NAGG NAGG NAGG NADG NAGG NAGG NAGG NADG NAGG NAGG NAGG NADG NAGG NAGG NAGG NADG NAGG NAGG NAGG NADG NAGG NAGG NAGG NAGG NAGG NAGG NAGG NAGG NAGG NAGG NAGG NAGG NAGG NAGG NAGG NAGG NAGG NAGG NAGG NAGG NAGG NAGG NAGG NAGG NAGG NAGG NAG

Table 2.1: CSP Repeat Regions from Various *Plasmodium* Species.

not develop efficiently, but future experiments are required to interrogate this hypothesis [12]. Hence, the ΔRep parasites did not enable us to elucidate the function of the repeats during sporozoite migration and infection of the liver.

We aimed to create mutants with more subtle phenotypes than the ΔRep so that we could begin to understand the role of the repeats in sporozoite biology. We first probed whether the length of the repeats was important, hypothesizing that the repeats might serve as a flexible linker between the two terminal domains, coordinating changes in domain exposure. For these studies we generated three CSP repeat truncation mutants: ΔRep1, ΔRep2, and ΔRep3 in which different lengths or regions of the repeats were deleted (Figure 2.1). We also generated a mutant to test the hypothesis that the repetitive nature of the repeats contain important structural features, ΔScr, in which we randomly scrambled the amino acid sequence of the repeats, avoiding introduction of new secondary structure, but maintaining amino acid content and length (Figure 2.1). Finally, we probed the possibility that charge of the repeats played a functional role. For this aim, we made the ΔDtoN parasite in which all of the negatively charged aspartic acids (D) were replaced with the most structurally similar neutral amino acid, asparagine (N) (Figure 2.1). Through the study of these mutants, we have found a critical role for the repeats in sporozoite motility, resulting in impaired infectivity of these lines *in vivo*.

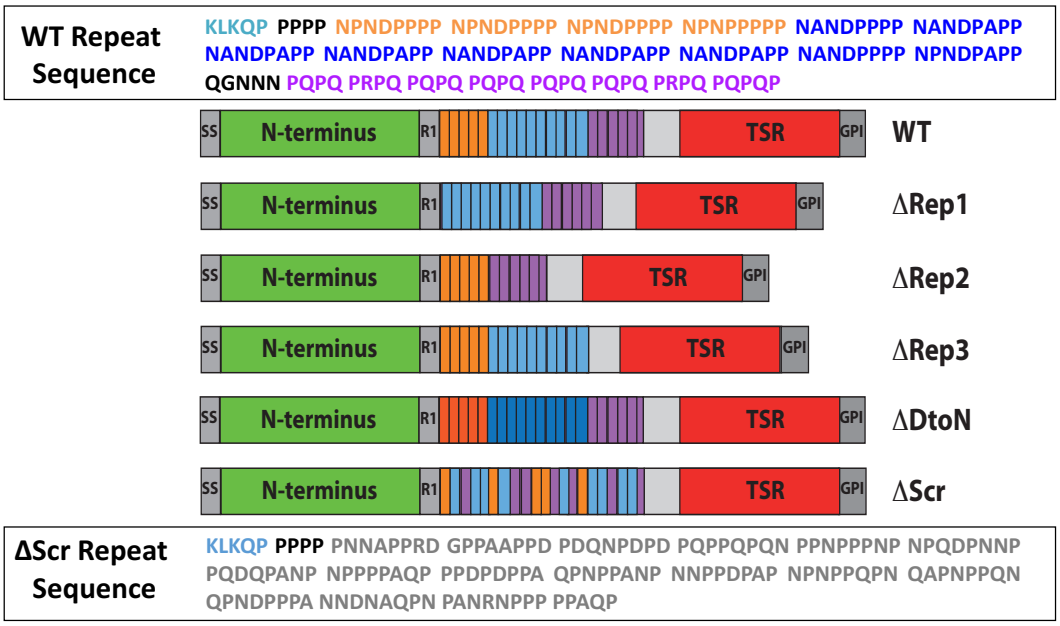

Figure 2.1: CSP Repeat Mutants. The amino acid sequence above the diagram is the WT *Plasmodium berghei* repeat sequence, with the region I cleavage sight in light blue. The three repeated sequences are color coded: orange = first repeat, blue = second repeat, and purple = third repeat. The color coding of the repeats in the amino acid sequence on top coordinates to the color coding in the CSP diagrams. The charge changes in the ΔDtoN parasite are indicated by darker colors of the first and second repeats. The scrambled repeats are indicated with mixing of the different repeat block colors, but the repeats of each block are not mixed, the entire amino acid sequence is scrambled. To clarify, the scrambled sequence is in gray below the diagram.

2.2 Methods

2.2.1 Antibodies

Anti-N and anti-C terminal antisera were previously generated against 100 amino acid peptides representing the entire N- or C-terminal domains and described in Coppi *et al.* [13]. Interestingly, the anti-C sera recognizes peptides from the TSR domain better than those of the predicted disordered region upstream of the TSR [14]. mAb 3D11 is specific for the *P. berghei* CSP repeats [15], and mAb 2E6 is directed against *Plasmodium* Hsp70 [16]. Antisera against the *P. berghei* TRAP repeats was previously generated as described in Ejigiri *et al.* [17] and raised against the peptide $(AEPAEPAEPAEPAEPAEPCNH)_2$. Antisera to the predicted disordered region of the C-terminus (anti-Cdis) of CSP, upstream of the TSR, was generated in a New Zealand White rabbit using a peptide produced by RS Synthesis (Louisville, KY). The sequence of the peptide was CDDSYIPSAEKILEFVKQIRDSITE and conjugated to keyhole limpet hemocyanin.

2.2.2 Generation of Mutant Parasites

2.2.2.1 Plasmid Generation

All CSP mutant parasite lines were developed using the transfection strategy outlined below. CSP repeat region sequences were commercially synthesized by Genscript (Piscataway, NJ) and provided in pUC57 plasmid. Repeat sequences were then digested from the pUC57 plasmid using HindIII-HF and SexAI restriction enzymes (Figure 2.2). The digested repeat sequences were

then ligated into the CSP workhorse vector in a Bluescript SK- plasmid which has the full *csp* sequence, but with HindIII-HF and SexaI restriction sites engineered into the regions flanking the repeats, and KpnI and PacI sites flanking the *csp* sequence (Figure 2.2 and 2.3). Once the mutant repeat sequences were ligated into the CSP workhorse vector, a KpnI and PacI digest was performed to cut out the mutant *csp* sequence, which was then ligated into transfection vector, pCSRep, previously described in Ferguson *et al.* [12] (Figure 2.3). pCSRep contains a 724 bp 5′ UTR homology arm followed by an hDHFR drug selection cassette flanked by the 5′ and 3′ UTRs of *P. berghei* DHFR-TS. After the selection cassette are: a *csp* cassette containing 637 bp of the csp 5′ UTR immediately upstream of *csp*, the *csp* ORF, and 1.5 kbp of the 3′ UTR of *csp* for homologous recombination (Figure 2.4). We found that having a longer 3′ UTR homology arm was necessary for effective integration of CSP repeat mutant sequences.

2.2.2.2 Transfection and Cloning

For transfection, pCSRep containing the desired repeat mutant sequence was linearized by digesting with XhoI and KasI. 5-10 μg of linearized construct was then electroporated into schizonts of the *P. berghei* ANKA 507 cl1 line which has a transgene GFP under the *eef1-α* promoter at the 230p locus (WT-GFP) [18]. Before electroporation, schizonts were isolated from overnight cultures of parasites collected from 5 Swiss Webster mice [18]. Following electroporation, schizonts were injected intravenously into a Swiss Webster mouse, selected with pyrimethamine, and cloned using limiting dilution into Swiss Webster mice as previously described [18].

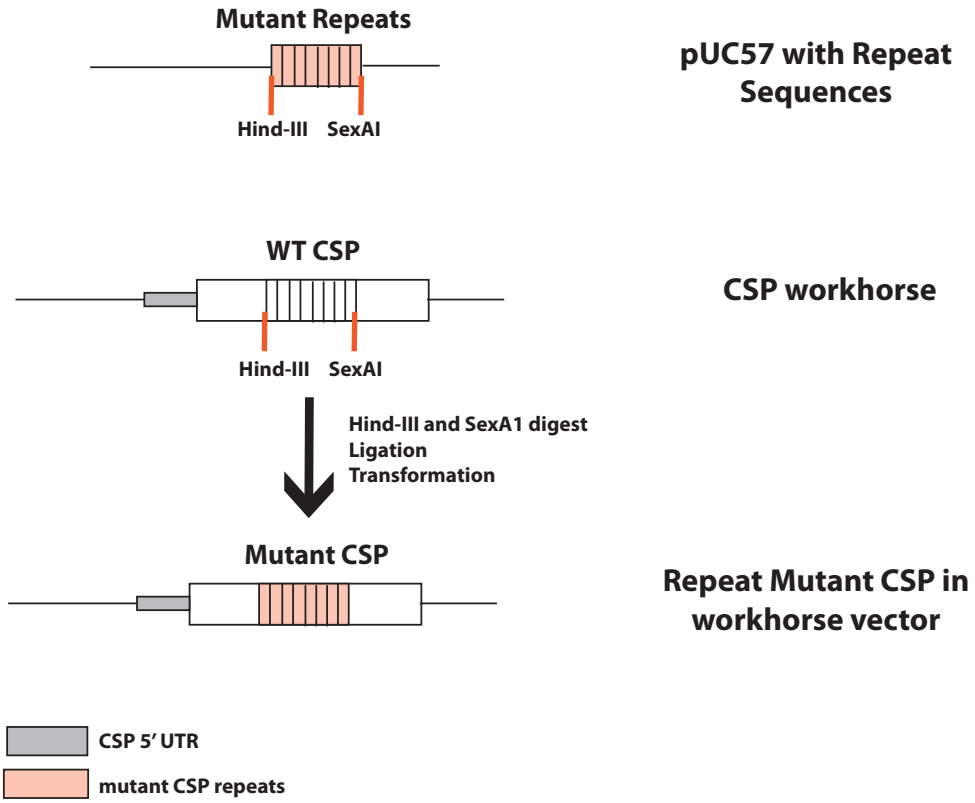

Figure 2.2: Molecular Cloning Step 1: Mutant Repeats into Workhorse Vector. CSP mutant repeats were synthesized by Genscript and provided in a pUC57 vector. Repeat sequences were then digested from the pUC57 plasmid using HindIII-HF and SexA1 restriction enzymes. The digested repeat sequences were then ligated into the CSP workhorse vector in a Bluescript SK- plasmid which has the full *csp* sequence, but with HindIII-HF and Sexa1 restriction sites engineered into the regions flanking the repeats.

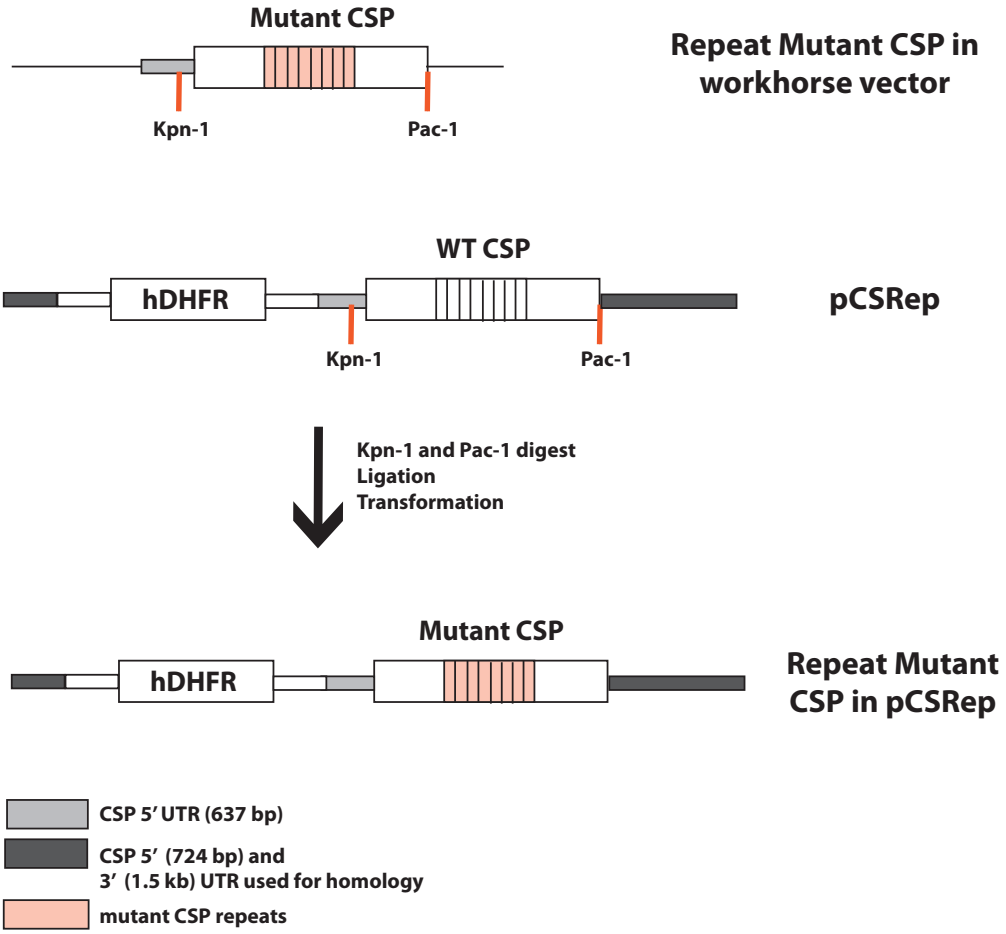

Figure 2.3: Molecular Cloning Step 2: Mutant Repeats into pCSRep. CSP workhorse vector has Kpn1 and Pac1 restriction sites flanking the *csp* sequence. CSP workhorse vector with repeat mutants and the pCSRep transfection vector were digested Kpn1 and Pac1 for mutant CSP ligation into pCSRep.

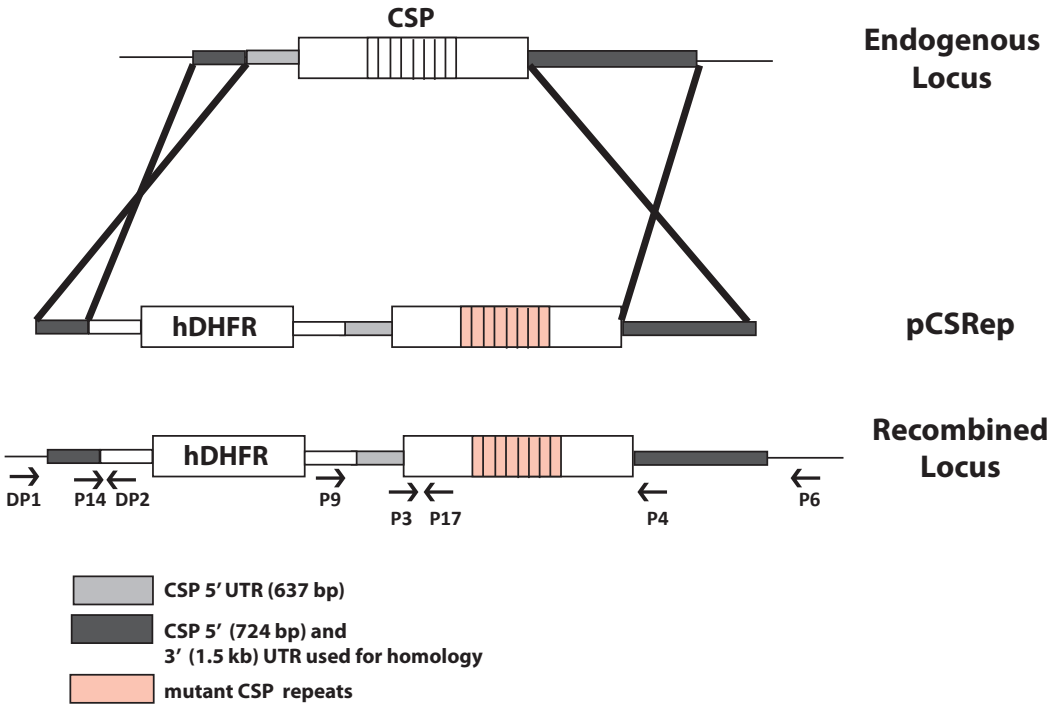

Figure 2.4: CSP Repeat Transfection Strategy. Transfections were done to replace the endogenous *csp* locus with *csp* that contained mutated repeats. pCSRep constructs contain a 5′ UTR homology arm, an hDHFR selection cassette, and CSP with 5′ and 3′ elements, the 3′ UTR of CSP being used for homologous recombination. Binding sites of primers described in the genotyping section are also shown above

2.2.2.3 Genotyping

Repeat mutant genotypes were confirmed by PCR and sequencing. See Figure 2.4 for primer binding sites and Figure 2.5 for PCR products. 5′ integration was confirmed using primers DP1 (5′-AATGAGACTATCCCTAAGGG-3′) and DP2 (5′-TAATTATATGTTATTTTATTTCCAC-3′), giving rise to a 1.1 kb PCR product in the mutant parasites. 3′ integration was confirmed

using primers P6 (5′-TGATTCATAAAT-AGTTGGACTTGATTT-3′) and P9 (5′-TCGAAATGGGCGCTGACAAGAA-3′) giving rise to a ∼4.8 kb product in mutant parasites (Figure 2.5A). Amplification of the *csp* locus was utilized to confirm repeat truncations using primers P3 (5′-CCATTTTAGTTGTAGCGTCACTTTT-3′) and P4 (5′-ACAAATCCTAATGAATTGCTTACA-3′). Expected sizes were as follows: WT-GFP (979 bp), ΔRep1 (832 bp), ΔRep2 (784 bp), ΔRep3 (856 bp), ΔDtoN (955bp), ΔScr (955 bp), and Rcon (955 bp) (Figure 2.5B). A size shift PCR was utilized to ensure no WT contamination of mutant clonal populations by utilizing the incorporation of the hDHFR to increase the amplicon size. P14 (5′-CGTGCATTTTGTGTCCTCATGTTGC-3′), binds the 5′ UTR of *csp* used as a homology arm, and P17 (5′-GCTCGTTTAAGTTCCTTTGGGCTTGG-3′), binds the N-terminus of *csp*, were used for this PCR so that WT amplification resulted in a 1.46 kbp product and CSP mutants gave a 4.810 kbp product (Figure 2.5C). After PCR confirmation, *csp* was amplified by PCR and sent for sequencing to confirm there were no undesired mutations.

2.2.3 Mosquito Infection and Sporozoite Isolation

Anopholes stephensi mosquitoes were reared in standard laboratory conditions and infected by feeding on anesthetized Swiss Websters with comparable gameotocytemia of either wild type or mutant parasites. For salivary gland sporozoite assays, salivary glands were dissected in Lebowitz media (L-15, Gibco #11415-064) 21-25 days after mosquito feeds. Dissected salivary glands were spun at 4°C (∼6 sec) to pellet salivary glands before removing the media from the pellet and adding fresh L-15. This protocol was utilized to

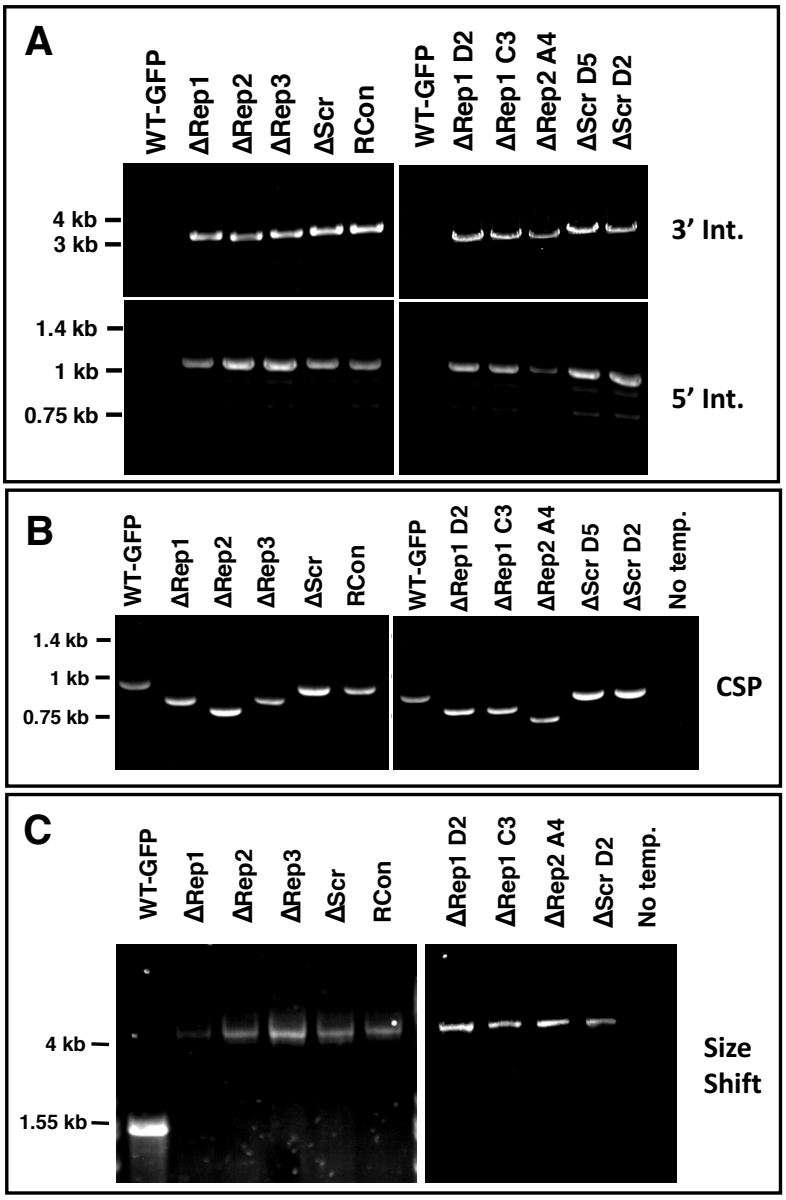

Figure 2.5: PCR Confirmation of Genotypes. A) 3′ and 5′ integration PCRs using DP1 and DP2 for 5′ integration, P6 and P9 for 3′ integration B) CSP PCR using P3 and P4 with size changes due to truncation and C) Size shift PCR using P14 and P17 which amplify the region 5′ of the *csp* open reading frame. If the hDHFR cassette is present, the product is 4.81 kbp while at an unmodified locus the product is 1.46 kbp. This PCR confirms there are no WT contaminants of the mutant lines. For all panels, on the left side are mutants clones used in most experiments and right side panels are from second independent transfection clones.

increase sporozoite concentration by resuspending the salivary glands in small volumes and to remove excess mosquito debris. Sporozoites were released from salivary glands by homogenization and centrifuged at 4°C for 4 minutes at 100g. The sporozoite supernatant was then collected and sporozoites were counted on a hemocytometer and then kept on ice in a fresh tube.

2.2.4 Sporozoite Progression Through the Mosquito

All mutants were assessed for oocyst number, sporozoite development in oocysts, release into the hemolymph, and entry into salivary glands. Approximately 20 mosquitoes from each parasite line were analyzed from cages with >85% infected mosquitoes. Oocyst numbers were assessed at 10-14 days post blood meal (pbm). Midguts of mosquitoes were dissected and wet-mounted on a glass slide with a 22 x 50 coverslip and imaged with a 4x objective on a Nikon Eclipse E600 upright microscope with a DS-Ri1 digital camera utilizing the GFP fluorescence of parasites. Oocysts numbers were then quantified using the multi-point function in Fiji (http://fiji.sc). For midgut, hemolymph, and salivary gland sporozoite numbers, mosquitoes were sorted by GFP fluorescence before dissection to ensure only infected mosquitoes were used for quantification. After sorting, midguts (day 16 pbm) or salivary glands (day 21 pbm) were dissected in L-15 and homogenized to release sporozoites for counting on a hemocytometer. Hemolymph (day 18 pbm) was collected by perfusion of the mosquito thorax and abdomen followed by counting on a hemocytometer. The total number of collected sporozoites was then

divided by the number of mosquitoes to calculate average number of sporozoites/mosquito.

For ΔRep2 and ΔScr the salivary glands of infected mosquitoes were imaged to confirm that sporozoites invaded the glands. Salivary glands were cleanly dissected from infected mosquitoes and then added to a 5 μl drop of L-15 media on a Matek well (MatTek #P35G-0-14C). After all glands were dissected, 5 μl of matrigel (BD #356231) was added and an 8 mm coverslip (Warner Instruments #64-0701) was placed on top and matrigel was allowed to polymerize at room temperature for $\sim$10 minutes. Z-stacks of salivary glands were then acquired using a 3i spinning disk confocal microscope (Zeiss Axio Observer Z1 microscope with Yokogawa CSU222 spinning disk), utilizing a 472 nm laser to observe GFP expressing sporozoites and DIC to observe the gland architecture.

2.2.5 Western Blots

For ΔRep1, ΔRep3, ΔDtoN, and RCon lines, salivary gland sporozoites were isolated as described above along with matched WT-GFP controls. For ΔRep2 and ΔScr, hemolymph sporozoites were used, as low parasite abundance in the salivary glands prevented clean western blots. Sporozoites were pelleted and resuspended in sample buffer (0.125M Tris-HCl, 20% glycerol, 4% SDS, .002% bromophenol blue, 50 mM DTT, and 1x protease inhibitors (Roche #11-836-153-001)) at a concentration of 1×10^7 sporozoites/mL, and 100,000 sporozoites were loaded per well. Samples were run on a 10% handcast SDS-PAGE gel and transferred to a nitrocellulose membrane. The membrane was

blocked with 2% milk/3% goat serum/0.1% tween/PBS before cutting just below the 75 kDa marker so that the top and bottom of the membranes could be probed separately. The bottom membrane was detected with anti-Cdis polyclonal sera diluted 1:100 and the top membrane with 1:500 anti-TRAP polyclonal sera in 2% goat serum/0.1% Tween/PBS. Both membranes were then incubated with 1:10,000 dilution of goat anti-rabbit HRP antibody (GE Healthcare #NA934V) and then detected with ECL reagent (GE Healthcare #RPN2106).

2.2.6 Immunofluorescence Assays (IFAs)

Salivary gland sporozoites were isolated from mosquitoes as described above and spun onto 12 mm coverslips (Fisherbrand #12-545-80) in a 24-well plate at 300g for 3 minutes at 4°C with low acceleration and no brake. For TRAP staining assays, media was exchanged for 2% BSA/L-15, pH 7.4 and sporozoites were allowed to glide on coverslips for 1 hour at 37°C with 5% CO_2. Sporozoites were then fixed for 1 hour with 4% PFA at room temperature, washed and blocked with 1% BSA/PBS for CSP antibodies or 1% BSA/5% goat serum/PBS for TRAP antisera before 1 hour incubation at 37°C with primary antibody. Primary antibody was either anti-N or -C terminal antisera (1:100) in 1% BSA/PBS or anti-TRAP repeat antisera (1:100) in 1% BSA/5% goat serum/PBS. To break intra-molecular interactions on the surface of the sporozoite, 0.1% saponin was incorporated into primary antibody dilutions when necessary. The appropriate secondary antibody was then utilized before mounting with Prolong Gold. Image acquisition was performed using

a 100x objective on a Nikon Eclipse E600 upright microscope with a DS-Ri1 digital camera under identical acquisition settings for each treatment condition. Sporozoites were identified by phase and then fluorescence imaging was performed in order to avoid bias acquisition. Intensity measurements were quantified using NIS Elements Br 3.2 software by using the "Auto ROI" function to identify the sporozoites in phase before switching to the fluorescence channel for intensity quantification.

2.2.7 Metabolic Labeling

Sporozoites were dissected from mosquitoes in DMEM without L-methionine or L-cysteine (Corning #17-204-C1) and 5x penicillin-streptomycin. All procedures were performed in a cold room to prevent pre-mature activation of sporozoites. Sporozoites were resuspended to a concentration of 150,000 sporozoites per condition (in 200-300 μl). [^{35}S]-Cys/Met (MP Biomedicals #0151006) was added in excess (>400 μCi/ml) to sporozoite suspensions and sporozoites were incubated at 28°C in a thermocycler for 45 minutes (ΔRep1) or 1.5 hr (ΔRep2), with mixing every 15 minutes by tapping the tube. Volumes were then increased to 500 μl with DMEM without L-methionine or L-cysteine and sporozoites were washed 3x in DMEM without L-methionine or L-cysteine to remove unincorporated ^{35}S-Cys/Met. After final wash, sporozoite pellets were resuspended in 400 μl of lysis buffer (150 mM NaCl, 50 mM Tris-HCl pH 8, 1% Triton X-100, 1x protease inhibitors (Roche #1836153)) and sporozoites were lysed for 1 hour with shaking. The lysate was centrifuged to pellet cell debris and the supernatant was added to a 10 μl bed of 3D11-agrose

beads and incubated overnight. Beads were washed with : 1) 500 μl of lysis buffer, 2) 500 μl high salt lysis Buffer (500 mM NaCl, 50 mM Tris-HCl pH 8.0, 1% Triton X-100, 1x protease inhibitors), 3) 500 μl low salt lysis buffer (50 mM Tris-HCl pH 8.0, 1% Triton X-100, 1x protease inhibitors), 4) 500 μl pre-elution buffer (10 mM Tris-HCl pH 6.8 and 0.55% Triton X-100). CSP was eluted from beads by adding 15 μl of elution buffer (0.1 M glycine pH 1.5 and 1% SDS) and collecting the supernatant. 10 μl of 6x SDS-PAGE sample buffer (0.35 M Tris-HCl pH 6.8, 0.35 M SDS, 30% glycerol, 0.175 mM bromophenol blue) was added to beads and the supernatent was collected and added to the supernatant collected from elution buffer washes before running on a 10% SDS-PAGE gel. The gel was then fixed (25% methanol and 12% glacial acetic acid) and incubated in Amplify (Amersham-Pharmacia Biosciences #NAMP100). The gel was then dried onto Whatman paper and exposed to film (Kodak BioMax MR film #162-2034) with Kodak BioMax Transcreen LE intensifying screen (#162-2034).

2.2.8 Pre-Patency and Liver Loads

5,000 sporozoites were injected intravenously into the tail vein of mice in 200 μL of cell culture media or intradermally into the ear of mice in 2 μL of cell culture media with a nanofil syringe (#nanofil with 36-gauge needle, #NF36BV). For pre-patency experiments, blood smears were made from days 3-9 after inoculation of sporozoites, stained with Giemsa (Sigma-Aldrich #GS500), and screened for 5 minutes for the presence of parasites. For liver load experiments, mice were sacrificed 39 hours post sporozoite inoculation,

livers were harvested and RNA was extracted [19]. Parasite liver load was quantified by RT-qPCR using primers specific for *P. berghei* 18s rRNA and compared to a plasmid standard curve. 4-5 week old Swiss Webster mice (Taconic) were used for pre-patency experiments and 4-5 week old C57BL/6 mice (Taconic) were used for liver load experiments.

2.2.9 Hepatocyte Infection Assays

Hepa1-6 cells (ATCC #CRL-1830), a mouse hepatocyte cell line, were seeded on collagen I coated LabTek wells (Lab-Tek #17745) with 100,000 cells/well in 400 μl of cell culture media (DMEM, 10% fetal calf serum, and 2 mM gentamycin) 1 day before infection with sporozoites. 20,000 sporozoites were added to hepatocytes and centrifuged onto cells at 300g for 3 minutes at room temperature with low acceleration and no brake. Sporozoites were then allowed to invade hepatocytes for 1 hour at 37°C with 5% CO_2, after which the media was replaced and cultures were maintained with 1x penicillin-streptomycin (Gibco #15140-122). Media was changed 2x daily and at either 24 or 48 hours post-infection, hepatocytes were fixed with 4% PFA for 1 hour at room temperature. Cells where then permeabilized with 100% methanol for 30 minutes at -20°C followed by blocking with 1% BSA/PBS at 37°C for 1 hour. Parasites were then stained with 10 μg/mL 2E6 (anti-HSP70) in 1% BSA/PBS for 1 hour at 37°C followed by 30 minutes with 0.1% tween/PBS at 37°C and 1 hour at 37°C with secondary antibody Alexa-488 goat anti-mouse (1:500) (Life Technologies #A11029) in 1% BSA/PBS before mounting with Prolong Gold with DAPI (Invitrogen #P36935).

The number of EEFs per 50 fields at 24 hours post-infection was quantified for each well, with technical duplicates or triplicates, for each condition. For quantification of EEF size within hepatocytes, the 2D area was measured with a 40x objective on a Nikon Eclipse E600 upright microscope with a DS-Ri1 digital camera and analyzed using NIS Elements "Auto ROI" function.

2.2.10 *In vitro* Live Gliding Assays

Salivary gland sporozoites were dissected as previously outlined. Concentrated sporozoite suspension (7 μl) was mixed with an equal volume of 2% BSA (Sigma #A788) in L-15, pH 7.4 and incubated at 37°C for 5 minutes to activate sporozoites. Activated sporozoite suspension (5 μl) was placed between a glass slide or 22 X 50 cover glass and a 22 x 50 cover glass (Fisherbrand #2-543-C) after cleaning these surfaces with a kimwipe to remove any debris. Sporozoites were allowed to settle for 2 minutes before imaging. Live gliding assays were done on a Nikon Eclipse E600 upright microscope using a 40x phase objective and imaging using phase contrast microscopy. Reflection interference contrast microscopy (RICM) imaging was done on a LSM 780 inverted confocal microscope using a 63x oil objective and excitation with a 488 laser. All movies were acquired with a 1 frame per second acquisition speed for 2.5 minutes. Fiji (http://fiji.sc) was used to manually track sporozoites by tracking displacement of the posterior end. For RICM analysis of adhesion sites, each frame was manually categorized as a sporozoite with small, large, or multiple adhesion sites. Small adhesion sites were were considered to be less than half the sporozoite body length, while large adhesion sites were

larger than half of the sporozoite body length. Data was presented as percent of time with small (assembly), large (disassembly), or multiple adhesion sites by dividing the number of frames observed for each adhesion state by the total number of frames (150), and multiplying by 100.

2.2.11 Single Molecule Studies

To generate the peptide-oligomer constructs which had Cy3 and Cy5 at either end of the construct, thus allowing for the utilization of FRET to measure distances between the two ends of a peptide, the following protocol was adapted from Brenner *et al.* [20] and diagrammed in Figure 2.6A. First, the DNA-oligo, ACCGCTGCCGTCGCTCCG, with 5' amine modification, was incubated with 200x molar excess of succinimidyl 4-[N-maleimidomethyl]cyclohexane-1-carboxylate (SMCC-Sigma-Aldrich #M5525) for 2.5 hours at room temperature to generate malemimide-DNA capable of sulfhydryl-reactive crosslinker chemistry with peptides with terminal cysteines. SMCC-Oligo conjugates were isolated using ethanol precipitation and dissolved in T150 (25 mM Tris, 150 mM NaCl, 1 mM EDTA) buffer and then run through Bio-Spin 6 columns (Bio-Rad #7326002) twice. Peptides with terminal cysteines were synthesized by GenScript and diluted to 200 μM in T150 buffer: WT (C-NANDPAPPNANDPAPPNANDPAPP-C) or Scrambled (C-NNNAPDDNAAANPPANPPPPD
C). Peptide was added to SMCC-Oligo at a 1:2.5 molar ratio and incubated overnight at 4°C for conjugation. Unreacted SMCC-Oligo was removed by polyacrylamide gel-electrophoresis followed by extraction from the gel.

250 pmoles of oligo-peptide conjugate was added to 250 pmoles 5′ -biotin-TGGCGACGGCAGCGAGGC-Cy5- 3′ and 300 pmoles 5′ -GGGCGGCGACCTGCTGGGTAGTC Cy3- 3′ and incubated overnight at 4°C for conjugation by complementary base pairing with the DNA conjugated to the peptide. For fluorescence force experiments, 16 nM λ-DNA (NEB #N3011S) in 0.120 M NaCl was heated to 80°C for 10 minutes followed by 5 minutes on ice. The Cy3-Cy5-peptide construct was added at 10 nM with 0.2 mg/mL BSA and incubated at 4°C for 3 hours followed by addition of 200 nM 5′ -AGGTCGCCGCCCTTT-digoxygenin- 3′ and overnight incubation at 4°C.

For single-molecule force spectroscopy (SMFS) experiments, an imaging chamber was made by sandwiching polyethylene-glycol (PEG) (a mixture of PEG-valeric acid and biotin-PEG-valeric acid, Laysan Bio) between a passivated quartz slide and coverslip. The imaging chamber was then incubated with 0.2 mg/mL neutravidin (Pierce) in blocking buffer (10 mM Tris-HCl pH 7.5, 50 mM NaCl, 1 mg/mL BSA , 1 mg/mL tRNA (Ambion)) for 1 hour. The peptide constructs were then diluted to 20 pM and immobilized on the surface via biotin-neutravidin interaction. 1 M anti-digoxygenin coated polystyrene beads (Polysciences) were conjugated to the peptide construct through λ-DNA of the peptide construct by incubation in a buffer containing 10 mM Tris HCl pH 7.5 and 150 mM NaCl for 30 minutes (Figure 2.6 A).

Microscope setup consisted of a trapping laser (1064 nm, 800 mW, Spectra Physics) to catch a bead. As the microscope stage was moved along the X-plane, a confocal laser (532 nm, 30 mW at maximum average power (World StarTech) was used to follow Cy3/Cy5 emission profiles. To apply tension,

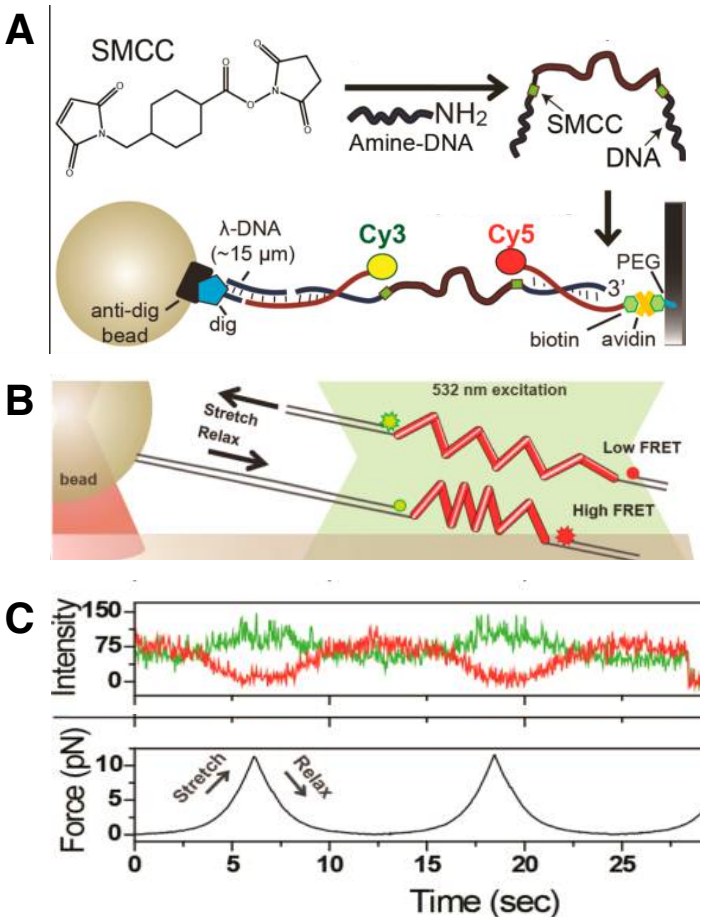

Figure 2.6: Single Molecule Force Spectroscopy using Optical Tweezers. Figures are adapted from Brenner *et al.* [20]. A) Cartoon of construct development. First, SMCC is conjugated to DNA to allow for sulfhydryl-reactive crosslinker chemistry to conjugate DNA to the peptides. Then the DNA-peptide conjugate can be paired with modified oligos through complementary base-pairing, to add fluorophores and binding partners for beads or glass slide. B) Cartoon of an SMFS experiment with bead conjugated to peptide in optical trap. As the bead is pulled, it stretches the peptide, increasing the distance between the two fluorophores. This results in a decrease in FRET signal. Upon relaxation, the fluorophores are brought closer together and FRET signal increases. C) Example measurements from an SMFS experiment. Top graph shows fluorescence intensity readings of both the Cy3 and Cy5 and bottom graph shows force applied to the bead. During peak stretching, Cy3 fluorescence intensity is highest as there is minimal energy transfer to Cy5 (low FRET). However, during relaxation phases, peaks in Cy5 intensity are observed (high FRET signal) as the Cy3 fluorophore is in closer proximity and can excite Cy5.

the stage was moved between 14 and 16.8 μm at a constant rate of 445 nm/sec as Cy3/Cy5 emission profiles were measured with an exposure time of 20 milliseconds (Figure 2.6B). The applied force was measured by a quadrant photodiode (UDT/SPOT/9DMI) from the position of the tethered bead. FRET trajectories as a function of force applied to peptides were then binned by 0.5 pN increments and plotted using Origin software (OriginLab) (Figure 2.6C).

2.3 Results: Phenotypes of Repeat Region Mutants

2.3.1 Mosquito Phenotypes of CSP Repeat Mutants

Previous stuides have shown that deletion of *csp* results in oocysts that do not produce sporozoites [21]. Furthermore, deletion of the CSP repeats leads to decreased sporozoite development and sporozoites dying prior to exiting the oocyst [12]. We therefore first characterized sporozoite development of our CSP repeat mutants. All parasite lines showed normal prevalence and intensity of mosquito infection compared to WT-GFP controls (Figure 2.7A&B), an expected result since CSP does not appear to be required for oocyst formation [21].

We then tested CSP repeat mutant sporozoite infectivity of salivary glands. ΔRep1 and ΔRep3 had comparable salivary gland infections to WT-GFP, while ΔRep2 and ΔScr parasites were severely inhibited in their capacity to invade the salivary glands and ΔDtoN parasites were moderately inhibited (Figure 2.8A). We confirmed that ΔRep2 and ΔScr sporozoites were inside the salivary glands, as opposed to attached to the glands (Figure 2.8B).

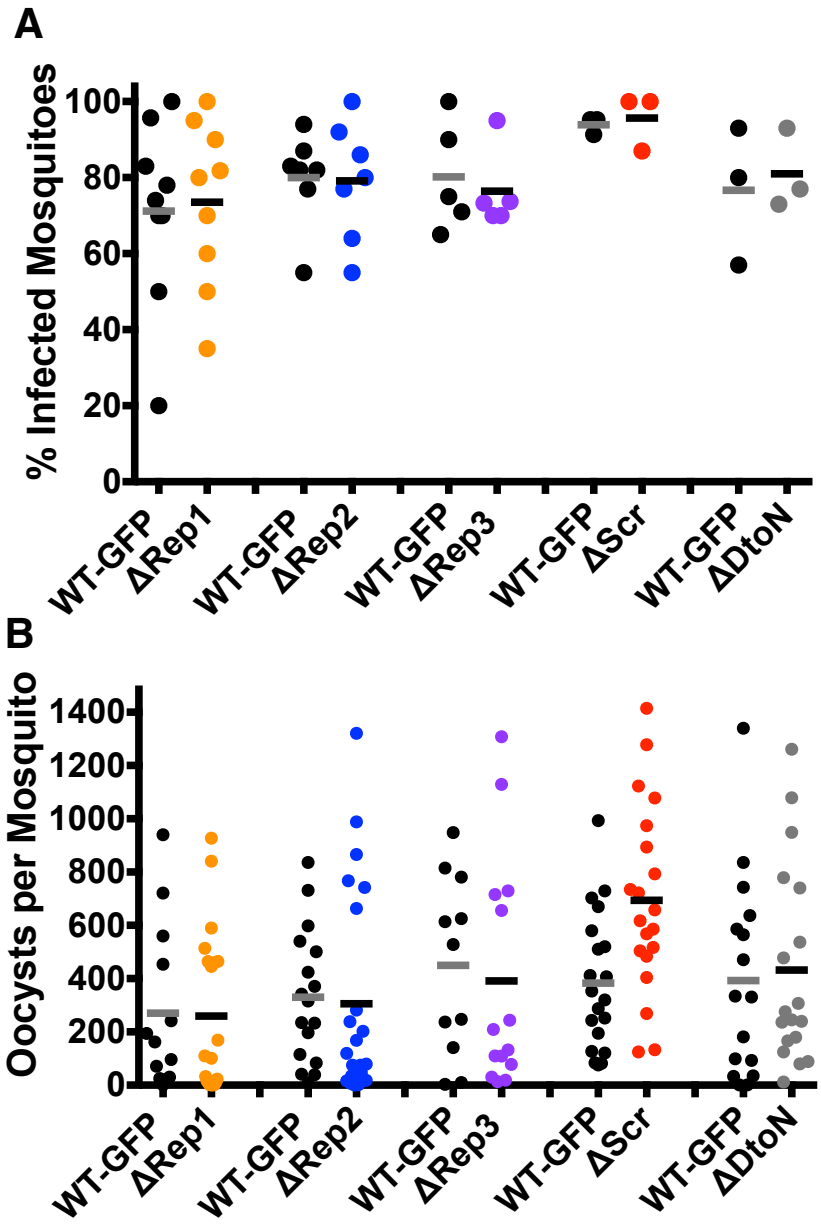

Figure 2.7: CSP Repeat Mutants Establish Normal Infection of Mosquito Midgut. At least 20 mosquito midguts were dissected from mosquitoes and wet mounted for observation of oocysts by GFP fluorescence at 10 days pbm. A) Percent of total mosquito midguts with oocysts, mutant cycles are matched with WT-GFP controls. Each dot represents an independent mosquito cycle. B) One representative cycle with oocysts per mosquito quantified from at least 20 midguts per line with matched WT-GFP controls.

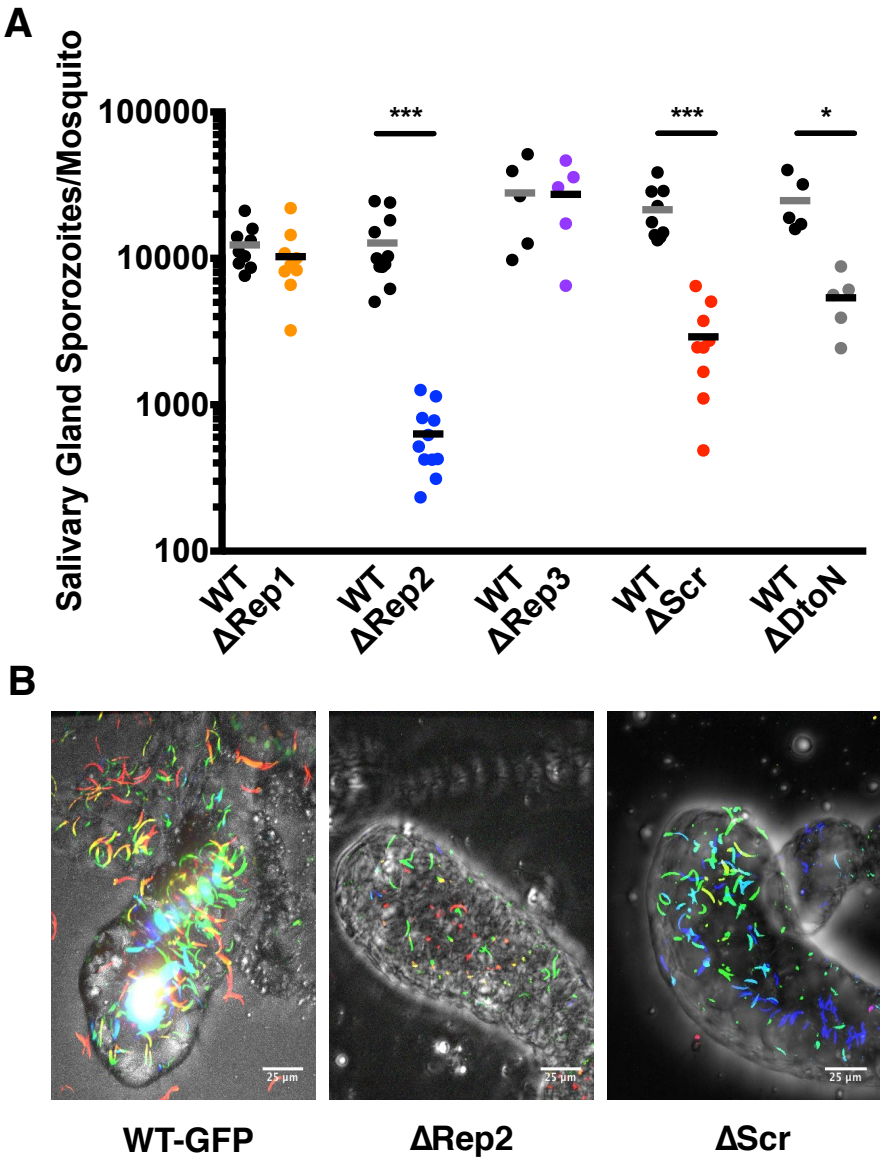

Figure 2.8: CSP Repeat Mutant Invasion of Salivary Glands. A) Sporozoites were isolated from the salivary glands of 20 infected mosquitoes. Salivary gland sporozoites per mosquito was calculated by dividing the total number of sporozoites by number of mosquitoes. Each data point is from an independent mosquito cycle with matched WT-GFP and mutant lines. Paired t-test: $p<0.05$. B) Live confocal imaging of infected mosquito salivary glands of WT-GFP, ΔRep2, and ΔScr. Overlay of GFP channel (sporozoites) and DIC. GFP channel is pseudocolored with different colors representing different positions in Z, allowing for visualization of sporozoite distribution through depth of salivary gland tissue.

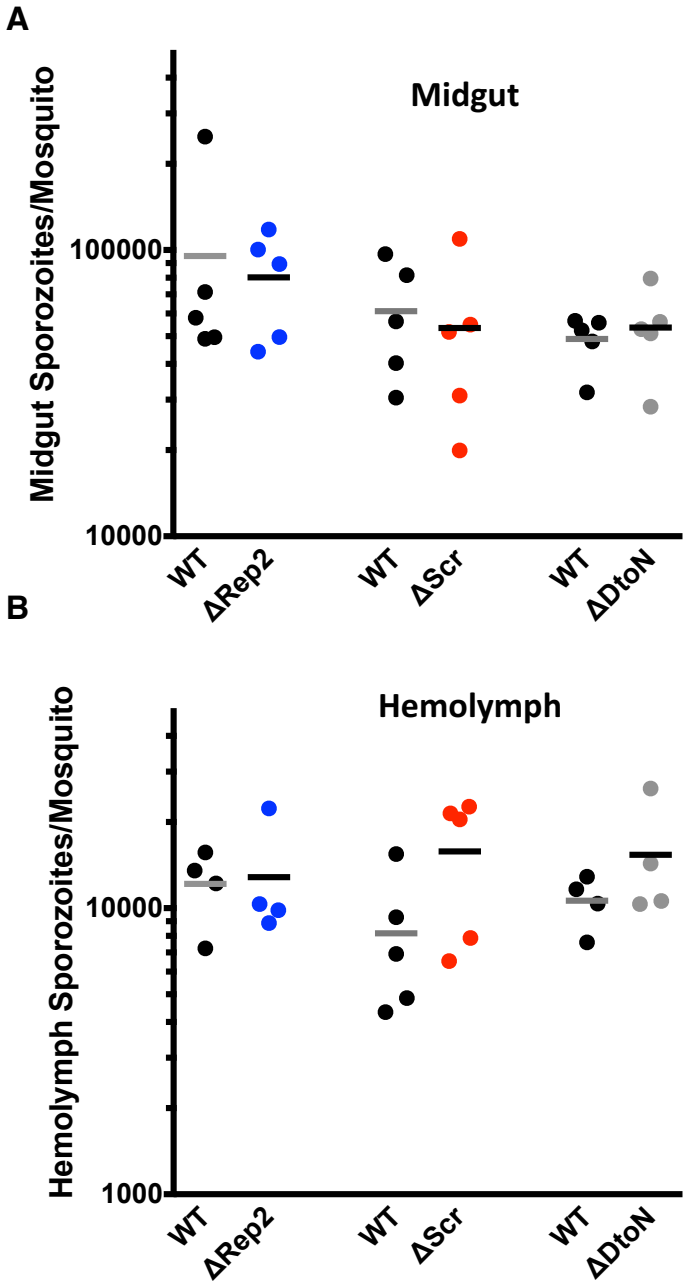

Figure 2.9: Repeat Mutants Exhibit Normal Sporozoite Development in the Mosquito Prior to Salivary Gland Invasion. A) Midgut and B) Hemolymph sporozoites were collected from 20 mosquitoes and expressed as the average number of sporozoites per mosquito. Each data point is from an independent mosquito cycle with matched WT-GFP and mutant lines. Paired t-test: $p<0.05$.

Since ΔRep2, ΔScr, and ΔDtoN exhibited salivary gland defects, we characterized their mosquito phenotypes in more detail (Figure 2.9A&B). First we determined whether sporozoite development in oocysts was normal by counting the number of sporozoites associated with mosquito midguts. As shown in Figure 2.9A, the number of midgut sporozoites for all three mutants was similar to controls, indicating no defect in sporozoite development. Next we quantified sporozoites released from the oocysts into the hemolymph and found equivalent sporozoite numbers in the hemolymph, of the repeat mutants compared to WT-GFP controls (Figure 2.9B), suggesting that the observed lower salivary gland sporozoites per mosquito observed in these mutants is due to defective invasion of the salivary glands.

2.3.2 CSP Expression in Repeat Mutant Sporozoites

To confirm that the CSP in our mutants was expressed at similar levels to that of WT-GFP, we performed western blotting of salivary gland or hemolymph sporozoites (Figure 2.10). For these assays, we generated a new antibody, αCdis, which targets a predicted disordered region between the repeats and TSR of CSP (see methods). A new antibody was required for these assays as the antibody normally used is mAb 3D11, which recognizes the CSP repeats and thus could not be used for our mutants. For mutants which generated particularly low numbers of salivary gland sporozoites (ΔRep2 and ΔScr), hemolymph sporozoites were used as we found that the enhanced amounts of mosquito debris resulting from the higher number of mosquitoes required interfered with the assay. TRAP was used as a loading control and lanes are

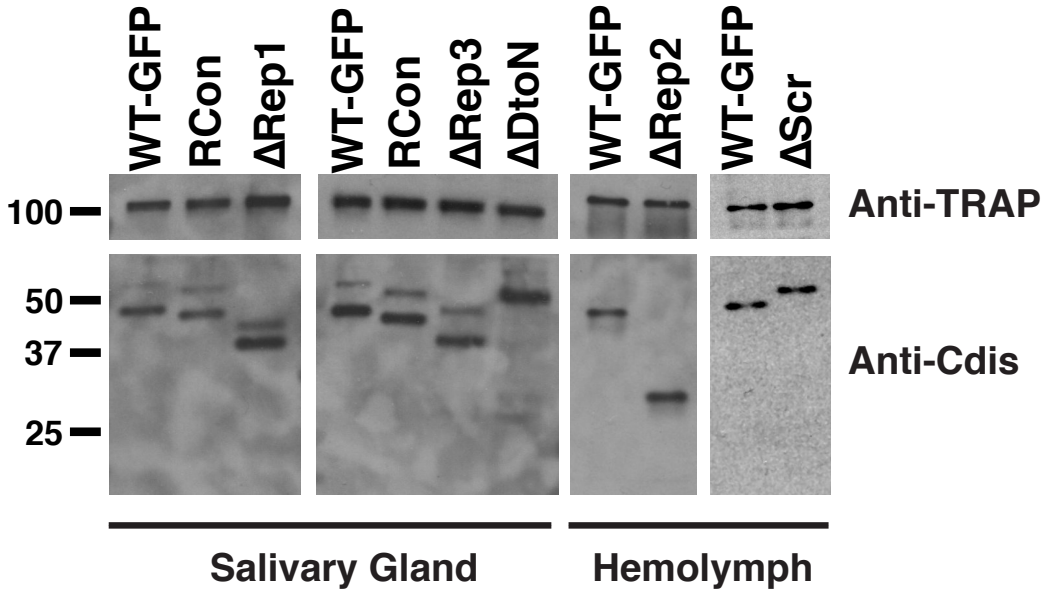

Figure 2.10: CSP Expression in Repeat Mutants. Western blots of CSP repeat mutants and WT-GFP or RCon controls. Membranes were cut along the 75 kDa marker so that the high molecular weight portion could be probed with anti-TRAP repeat sera while the lower molecular weight portion was probed with anti-Cdis antisera. Enough sporozoites were collected to use salivary gland sporozoites for ΔRep1, ΔRep3, and ΔDtoN blots, but ΔRep2 and ΔScr blots required the use of hemolymph sporozoites for a cleaner prep. Molecular weight markers are indicated on the left.

loaded with the same sporozoite equivalents per well. No observable differences in CSP abundance was detected (Figure 2.10). Additionally, comparable amounts of TRAP were detected between mutant and WT-GFP sporozoites (Figure 2.10).

2.3.3 CSP Conformation and Processing

Polyclonal sera against the N- and C-terminal domains of CSP have previously been developed and used to probe CSP conformational changes on the surface of the sporozoite [14]. Previous studies found that the C-terminal adhesion

domain was exposed only during sporozoite development in the oocysts and when sporozoites reached the liver [14]. In between, the N-terminal domain was exposed and the C-terminal domain was masked [14]. We utilized these antibodies to probe conformational changes in CSP in our repeat mutants. Except for ΔRep2 and ΔScr, repeat mutants exhibited a similar staining pattern as WT-GFP, with exposure of the N-terminus and masking of the C-terminus (Figure 2.11). In contrast, ΔScr salivary gland sporozoites showed diminished exposure of both terminal domains, while ΔRep2 salivary gland sporozoites had an exposed C-terminus, but the N-terminal domain was not recognized. Overall, CSP repeat mutants had comparable levels of CSP on the plasma membrane, as determined by treating sporozoites with 0.1% saponin with the anti-C-terminal antibody to break intramolecular interactions on the surface, exposing the C-terminal domain and allowing for the comparison of total CSP on the surface of CSP mutant sporozoites and that of WT-GFP (Figure 2.11C).

The ΔRep2 phenotype could be explained by two mechanisms: 1) conformational changes of CSP on the surface of ΔRep2 sporozoites or 2) proteolytic processing of the N-terminus of CSP, which would lead to exposure of the C-terminal domain [13]. To determine if premature cleavage of the N-terminus could account for the premature exposure of the C-terminus, we metabolically labeled CSP in WT-GFP, ΔRep1 (as an additional control), and ΔRep2 salivary gland sporozoites to observe the rate of CSP cleavage. No differences in CSP cleavage were observed in ΔRep2 sporozoites (Figure 2.12). Thus, we hypothesize that the repeats form a linker between the N- and C-terminal domain and must be of a certain length to achieve masking of the C-terminal domain.

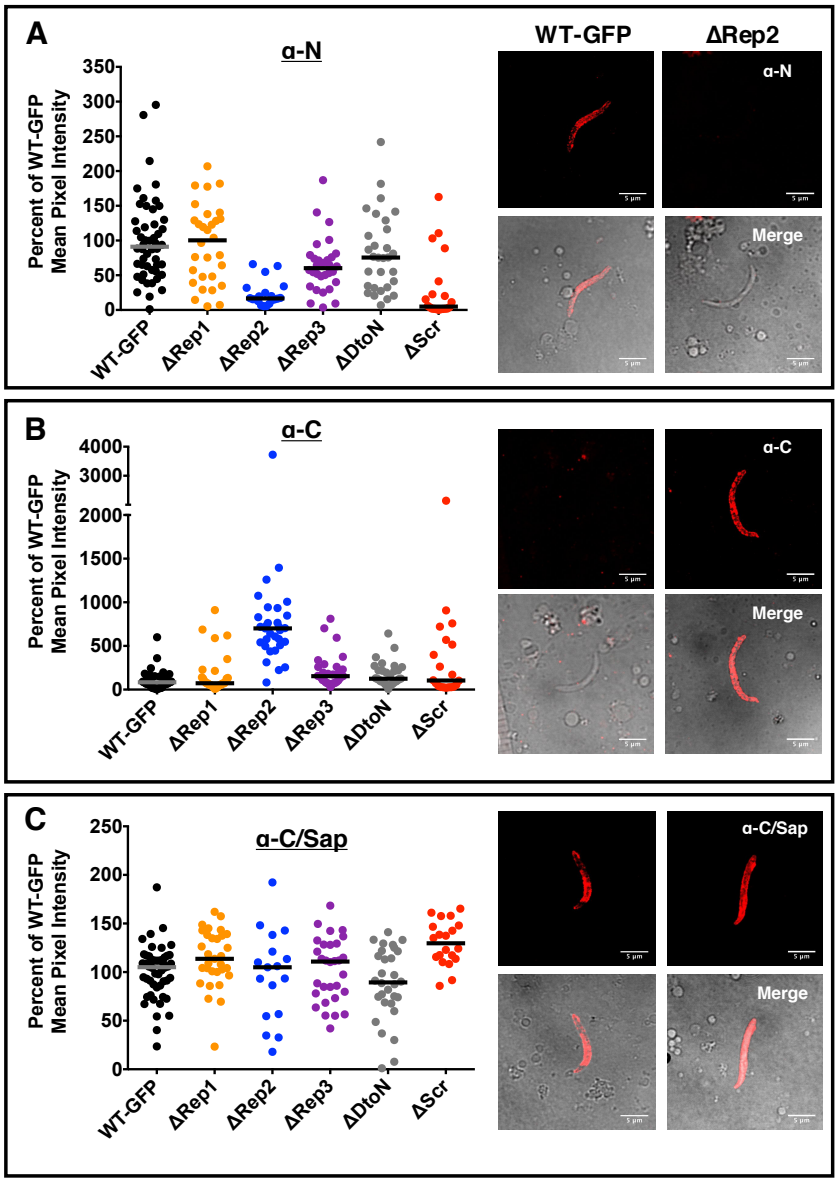

Figure 2.11: CSP Domain Exposure of Repeat Mutants. Unpermeabilized salivary gland sporozoites were stained with antibodies specific to the N- (A) or C-terminus (B) of CSP. As a positive control, 0.1% saponin was included with anti-C sera (labeled as αC/Sap) (C). 20-30 sporozoites per condition were quantified for mean pixel intensity and presented as percent of the mean pixel intensity of matched WT-GFP salivary gland sporozoites. Representative sporozoite staining of WT-GFP and ΔRep2 for each antibody condition is shown to the right of each panel with fluorescence and merge (fluorescence + DIC) images.

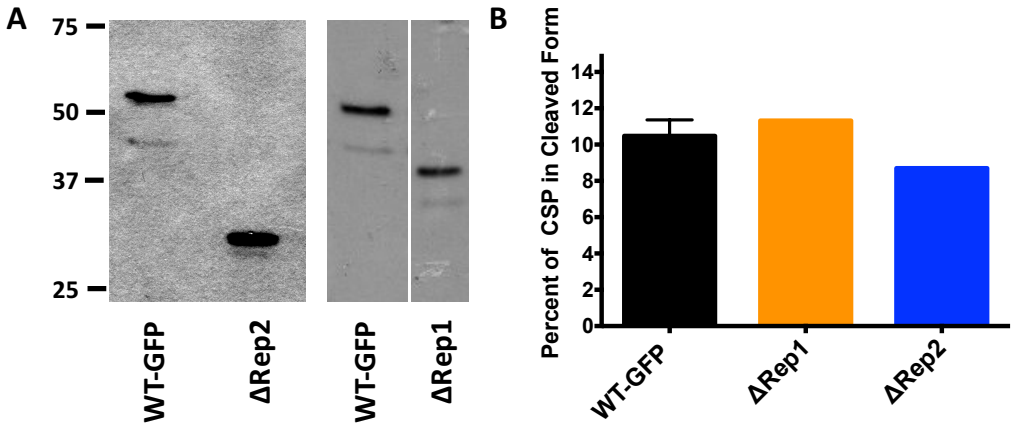

Figure 2.12: Metabolic Labeling to Monitor CSP Cleavage in ΔRep2. WT-GFP, ΔRep2, and ΔRep1 sporozoites were metabolically labeled with [^{35}S]-Cys/Met and CSP was immunoprecipitated and run on an SDS-PAGE gel followed by autoradiography. Band intensities were measured by densitometry and percent of total CSP detected in the bottom band (cleaved) is expressed in the graph in panel B. WT-GFP is pooled from both blots.

2.3.4 Sporozoite Infectivity of CSP Repeat Mutants

To assess the capacity of mutant salivary gland sporozoites to infect mice, we intravenously inoculated 5,000 sporozoites per mouse into 5 Swiss Webster mice with matched WT-GFP controls. Development of blood stage infection (patency) was then assessed by blood smears to determine whether mutants were infectious. We found that ΔRep2 sporozoites were severely defective in initiating blood stage infections, with only one of ten mice becoming patent (Table 2.2). ΔRep1, ΔRep3, ΔScr, and ΔDtoN lines did not exhibit dramatic phenotypes in this assay (Table 2.2). Therefore, we utilized a more sensitive measure of sporozoite infection utilizing RT-qPCR of parasite RNA from total liver RNA extraction. We discovered that upon intravenous inoculation, ΔRep1, ΔScr, and ΔDtoN parasites were less abundant in the livers of mice

Parasite	# of Mice Patent	Time to Patency (days)
WT-GFP	15/15	3.6
ΔRep1	15/15	4.2
WT-GFP	10/10	3.4
ΔRep2	1/10	5
WT-GFP	5/5	3.8
ΔRep3	4/5	3.25
WT-GFP	15/15	3.3
ΔScr	12/15	4.75
WT-GFP	5/5	3.8
ΔDtoN	4/5	4.5

Table 2.2: Pre-Patency of CSP Repeat Mutants. 5,000 sporozoites of the indicated mutant or WT-GFP line were inoculated intravenously into Swiss Webster mice and mice were monitored by blood smear to determine the number of mice that became patent and of these, the average day of patency is shown. For each mutant 1-3 experiments are pooled.

in comparison to their matched WT-GFP controls. While the recombinant control (RCon) did not show any defects in liver infection by this assay, when RCon and ΔRep1 experiments were done side-by-side, no infection defect was observed in the ΔRep1 (Figure 2.13A), suggesting that ΔRep1 either does not have a liver infection defect, or if it does it is too subtle to be reliably detected by the available assays. To test whether the ΔRep1 and ΔRep3 would have infectivity phenotypes upon inoculation into the skin, we also tested their infectivity after intradermal inoculation and found that no significant infection defects were observed (Figure 2.13B).

To confirm that the defects in parasite abundance in the liver of the ΔScr and ΔDtoN were due to defects in infection of hepatocytes, we performed *in vitro* hepatocyte infection assays with Hepa1-6 cells, a mouse carcinoma cell line. As expected, both CSP repeat mutant lines showed fewer EEFs *in vitro* than matched WT-GFP controls (Figure 2.14A), but did not show defects in EEF development/growth (Figure 2.14B), suggesting that CSP repeat mutant liver infection defects are the result of inefficient invasion of hepatocytes.

2.3.5 Gliding Motility of CSP Repeat Mutants

ΔRep2, ΔScr, and ΔDtoN sporozoites exhibited a diminished capacity to infect two very different tissues: the salivary glands of mosquitoes and the liver of mice. Lack of tissue specificity in the infectivity phenotype of the CSP repeat mutants suggests these phenotypes are not the result of interrupted receptor-ligand interactions, but due to a feature required of sporozoites at both stages. Previous studies have shown that sporozoites with motility defects cannot

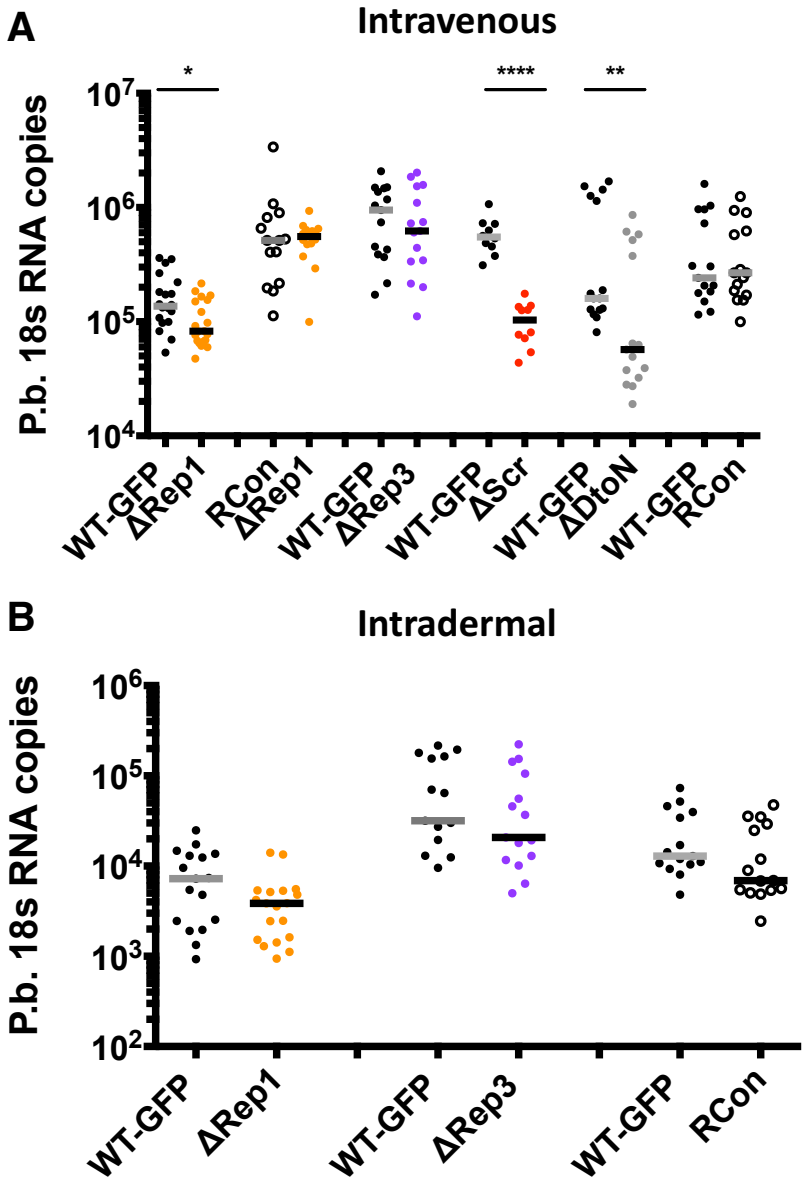

Figure 2.13: CSP Repeat Mutant Sporozoite Infectivity of the Liver. *In vivo* infection assays were performed in C57B/6 mice. Relative parasite abundance in the livers of mice infected A) intravenously or B) intradermaly with 5,000 sporozoites was determined by P.b. 18s RNA copy number. Pooled data from 2 or 3 experiments with 5 mice per condition in each experiment. Mann-Whitney test: $p<0.05$.

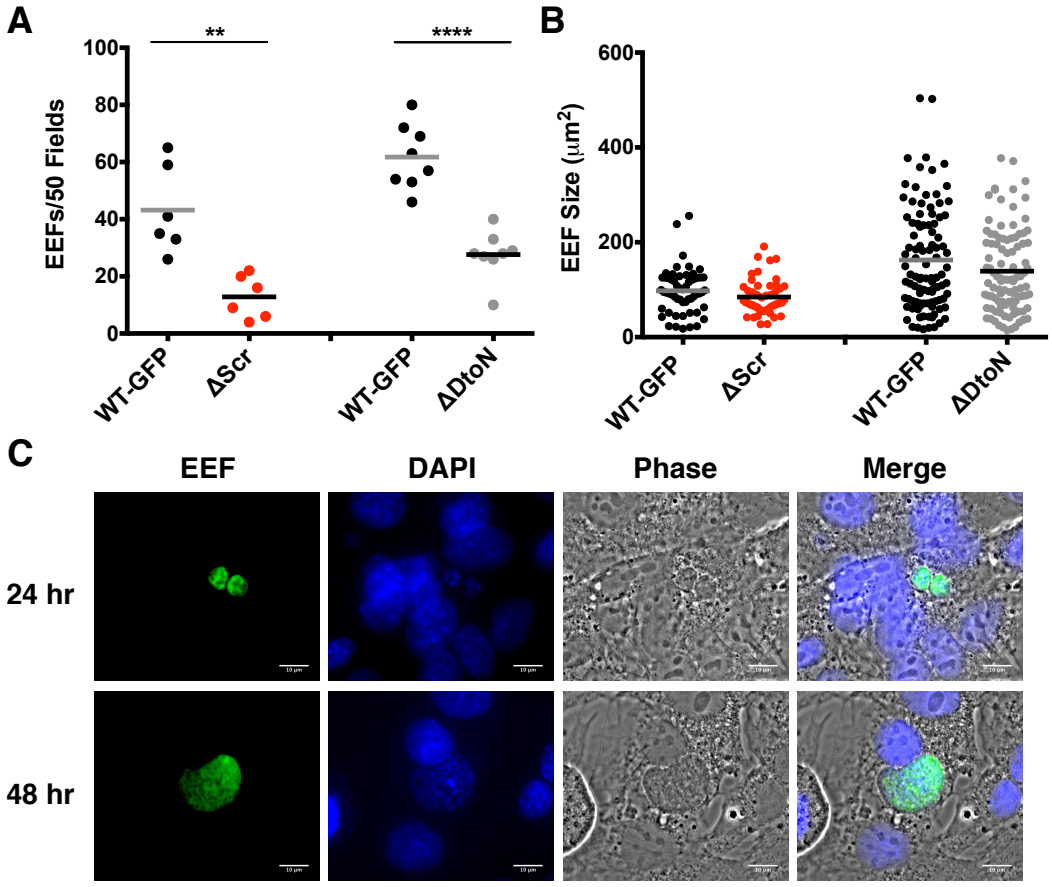

Figure 2.14: CSP Repeat Mutant Sporozoite Infectivity of Hepatocytes *in vitro*. Sporozoites of the indicated lines were added to Hepa1-6 cells and EEFs were allowed to develop for 24 or 48 hours and then cells were fixed and EEFs were stained with anti-HSP70 for quantification of A) number of EEFs per 50 fields at 24 hours and B) EEF size at 48 hours. Data from two to three independent experiments are pooled. Unpaired t-test with Welch's correction: $p<0.05$. C) Representative images of EEFs at 24 hrs and 48 hours post infection with sporozoites.

invade salivary glands or hepatocytes efficiently [17, 22, 23]. Therefore, we investigated the motility of the CSP repeat mutants.

2.3.5.1 CSP Repeat Mutant Motility Behavior

To investigate parasite motility, we utilized several *in vitro* assays. First, we performed live gliding assays with salivary gland sporozoites, pre-incubating sporozoites in BSA at 37°C to activate them for gliding and then adding them to coverslips for imaging and recording their motility in 2.5 minute movies [24]. First we determined the percent of total visualized sporozoites that were motile and, as shown in Figure 2.15A, did not observe any significant differences in percent of motile parasites. Next we categorized sporozoite motility in these movies according to previously observed motility phenotypes: patch gliding, waving, or circling as shown in Figure 2.15B and as described on page 9 [24]. Patch gliding consists of parasites moving back and forth without any net displacement, while waving parasites are attached at one end and flex the other [24]. WT-GFP parasites predominantly move in circles *in vitro* (Figure 2.15C) [24], as do ΔRep1 and ΔRep3 (Figure 2.15C). By contrast, ΔRep2 and ΔScr sporozoites had an increase in the number of sporozoites patch gliding or waving (Figure 2.15). ΔDtoN sporozoites showed an intermediate phenotype with approximately 30% of sporozoites patch gliding or waving in comparison to the 12% seen in WT-GFP (Figure 2.15C). If we consider productive motility to be motility that results in displacement, the smaller truncation mutants ΔRep1 and ΔRep3, move productively, while ΔRep2, ΔScr, and ΔDtoN parasites have an enhanced proportion of sporozoites moving unproductively (Figure 2.15C).

A

Parasite Line	WT-GFP	ΔRep1	ΔRep2	ΔScr	ΔDtoN
% Moving (Mean +/- SEM)	90.2 +/- 1.8	85.4	91.8 +/- 2.8	77. 5 +/- 9.3	88.00

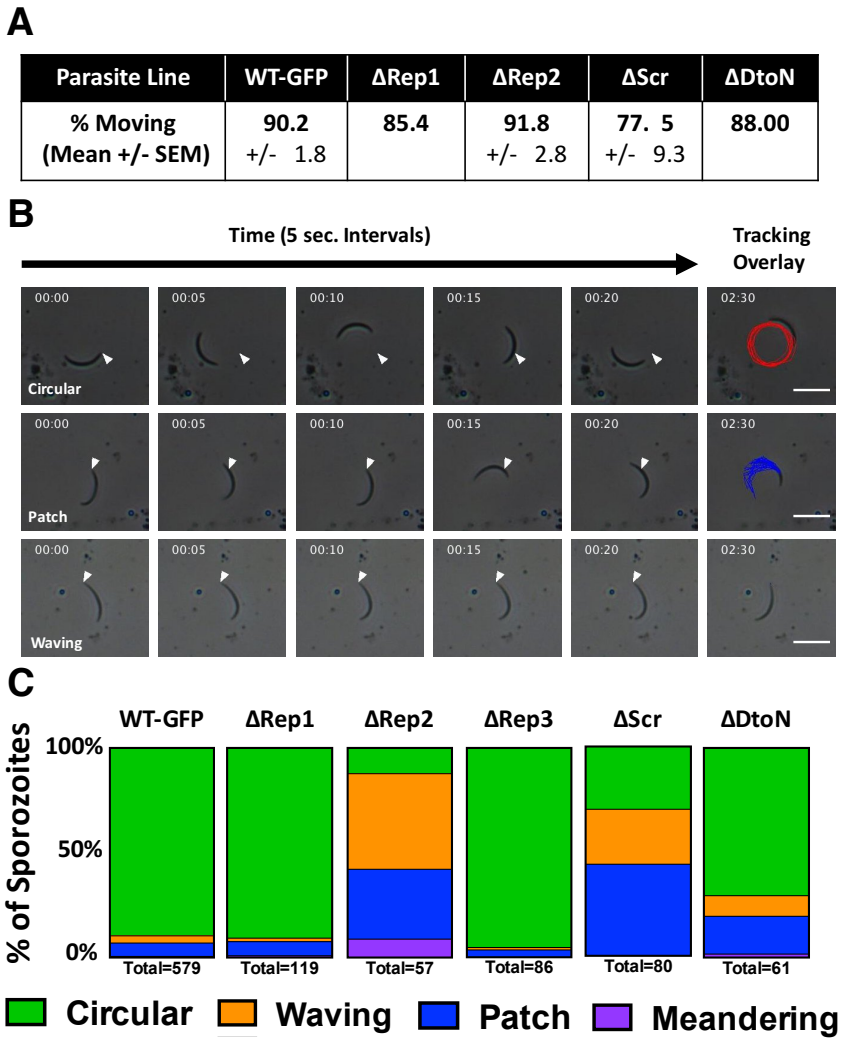

Figure 2.15: Motility Behavior of CSP Repeat Mutants. A) Table showing percent of sporozoites moving out of 55 sporozoites per experiment. Moving included productive or non-productive motility. Floating or still parasites were considered non-motile. If multiple independent experiments were conducted, percents are displayed as mean +/- SEM. Unpaired t-test with Welch's correction: $p<0.05$. B) Examples of the three predominate classes of motility behavior observed: circular gliding, patch gliding, and waving. First 20 seconds of a movie are shown at 5 second intervals with the tracking overlay from the entire movie in the final column. White arrow indicates posterior end location at the beginning of the movie for orientation. C) Binned motility behaviors for each mutant. Percent of bar occupied by a given motility behavior corresponds to percent of sporozoites exhibiting that motility behavior. Mutant assays were always done side-by-side with WT-GFP controls. At least three experiments per mutant were done. Total number of sporozoites analyzed is indicated below each bar.

2.3.5.2 Speed of Gliding CSP Repeat Mutants

We then used the movies of mutant and WT-GFP sporozoites to determine their median and maximum speeds as well as the distribution of instantaneous speeds. These data were separately analyzed for circular gliding and patch gliding parasites. Instantaneous speed distributions were generated by extrapolating the speed of parasites from every frame of a movie, such that each parasite had 149 speeds per movie. Data from several movies were combined and then the amount of time parasites spent at each 0.5 μm\second interval was extrapolated. We found that both the circular gliding ΔRep2 and ΔScr sporozoites spent more time not moving, as determined by the intersection with the y-axis, than their WT-GFP counterparts (Figure 2.16A), and more time moving at slower speeds (Figure 2.16A), resulting in a lower median speed (Figure 2.16B). However, no severe defects in maximum speed were observed in ΔRep2 (Figure 2.16), suggesting that the motor machinery was still functional. Patch gliding ΔRep2 and ΔScr parasites also exhibited faster speeds than WT-GFP patch gliders and spent more time moving (Figure 2.17A). These data were also observable in the median and maximum speed of ΔRep2 and ΔScr patch gliding parasites, both of which were higher than WT-GFP (Figure 2.17B&C).

2.3.5.3 TRAP Secretion During Sporozoite Motility

As thombospondin-related anonymous protein (TRAP) is believed to be the adhesin that links to the motor complex for parasite motility, we hypothesized that CSP repeat mutants which exhibited enhanced non-productive motility,

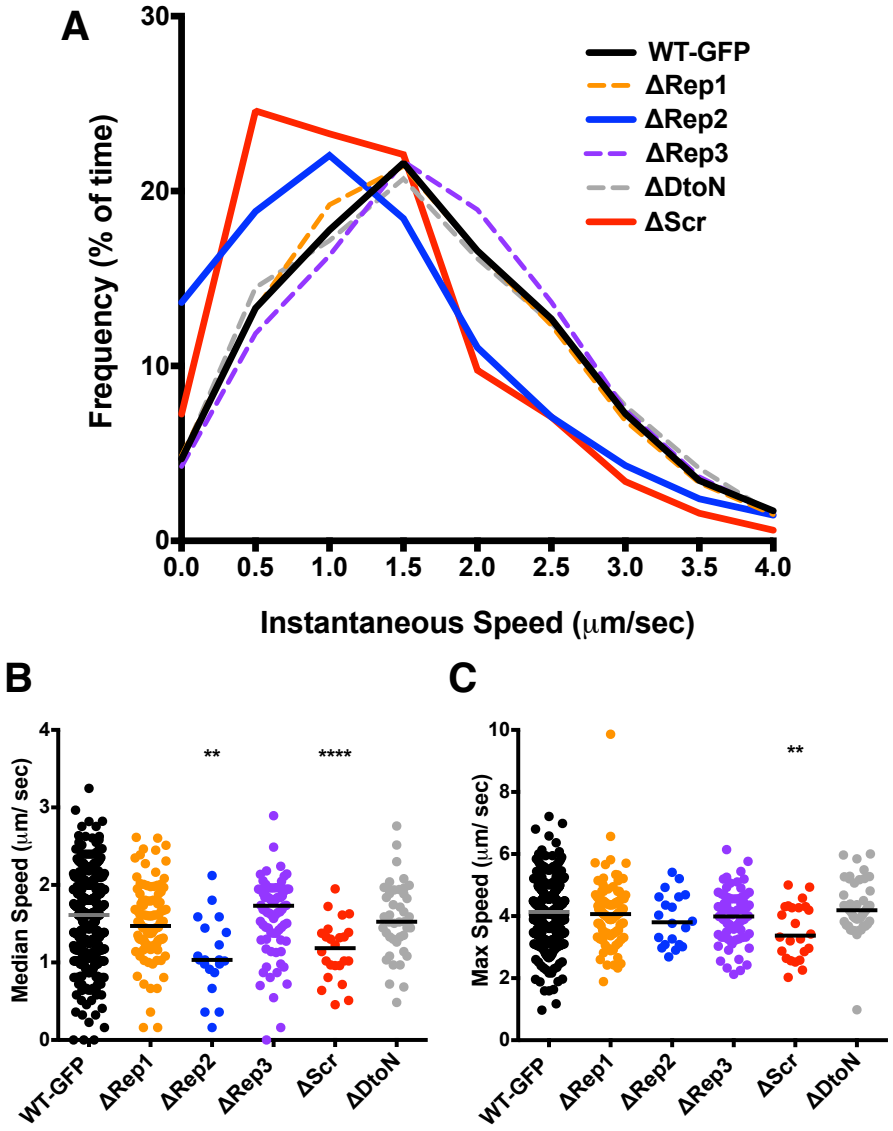

Figure 2.16: Analysis of CSP Repeat Mutants Circular Gliding Speeds. Speed analysis of circular gliding parasites from each mutant and WT-GFP line. Movies of gliding salivary gland sporozoites were imaged for 2.5 minutes at 1 frame per second and the posterior end of each gliding sporozoite was tracked. A) All circular gliding speeds recorded were pooled to determine the frequency that sporozoites spent in each 0.5 μm per second speed bin. B) Median and C) maximum speeds for each circular gliding parasite recorded with pooled WT-GFP controls. Each experiment was performed at least three times with independent mosquito cycles for each experiment. Mann-Whitney test= $p<0.05$. Number of circular gliding sporozoites analyzed for each parasite line are as follows: WT-GFP = 522, ΔRep1=108, ΔRep2=20, ΔRep3=82, ΔScr=24, ΔDtoN=43.

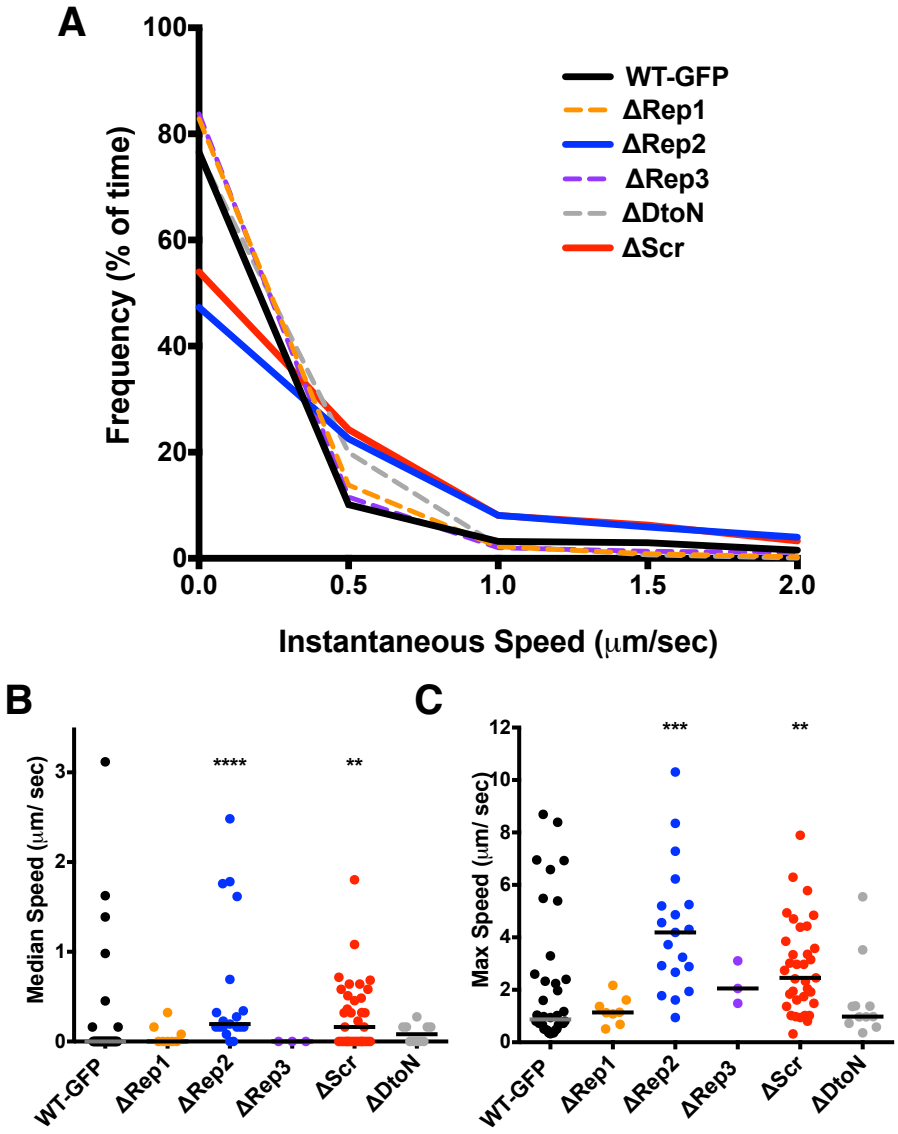

Figure 2.17: Analysis of CSP Repeat Mutants Patch Gliding Speeds. Speed analysis of patch gliding parasites from each mutant and WT-GFP line. Movies of gliding salivary gland sporozoites were imaged for 2.5 minutes at 1 frame per second and the posterior end of each gliding sporozoite was tracked. A) All patch gliding speeds recorded were pooled to determine the frequency that sporozoites spent in each 0.5 μm per second speed bin. B) Median and C) maximum speeds for each patch gliding parasite recorded with pooled WT-GFP controls. Each experiment was done at least three times with independent mosquito cycles for each experiment. Mann-Whitney test= $p<0.05$. Number of patch gliding sporozoites analyzed for each parasite line are as follows: WT-GFP = 38, ΔRep1=8, ΔRep2=19, ΔRep3=3, ΔScr=35, ΔDtoN=10.

did so due to the disorganization of TRAP on their surface. To test this we performed immunofluorescence assays on unpermeabilized gliding sporozoites using polyclonal antisera specific for TRAP. Interestingly, we found that mutants exhibiting a significant amount of non-productive motility (ΔRep2, ΔScr, and ΔDtoN), had a marked decrease in detectable TRAP on the sporozoite surface (Figure 2.18), even though TRAP was observed to be expressed at comparable levels to control sporozoites (Figure 2.10). These data suggest that TRAP function has been perturbed in the CSP repeat mutants with enhanced non-productive motility.

2.3.5.4 Adhesion Site Assembly in Circling CSP Repeat Mutant Parasites

To better understand the differences in motility among the CSP repeat mutants, we explored adhesion site turnover. Gliding motility is thought to involve the assembly and rapid turn over of adhesion sites, with assembly and disassembly phases as sporozoites move forward (Figure 2.19A). An adhesion site first forms at the anterior end of the sporozoite, it then grows (assembles), sometimes becoming as large as the full length of the sporozoite, and then disassembles, becoming smaller at the rear end of the sporozoite (Figure 2.19A & B). This is then rapidly followed by the formation of another adhesion site that assembles at the anterior end of the sporozoite (Figure 2.19A & B). We visualized sporozoite motility by reflection interference contrast microscopy (RICM). RICM utilizes properties of reflected light such that cell membranes which are closer to the coverslip (adhesion sites) are dark and those further away are white or gray (Figure 2.19B)[25]. Since parasites exhibiting non-productive gliding patterns do not turn over adhesion sites these sporozoites

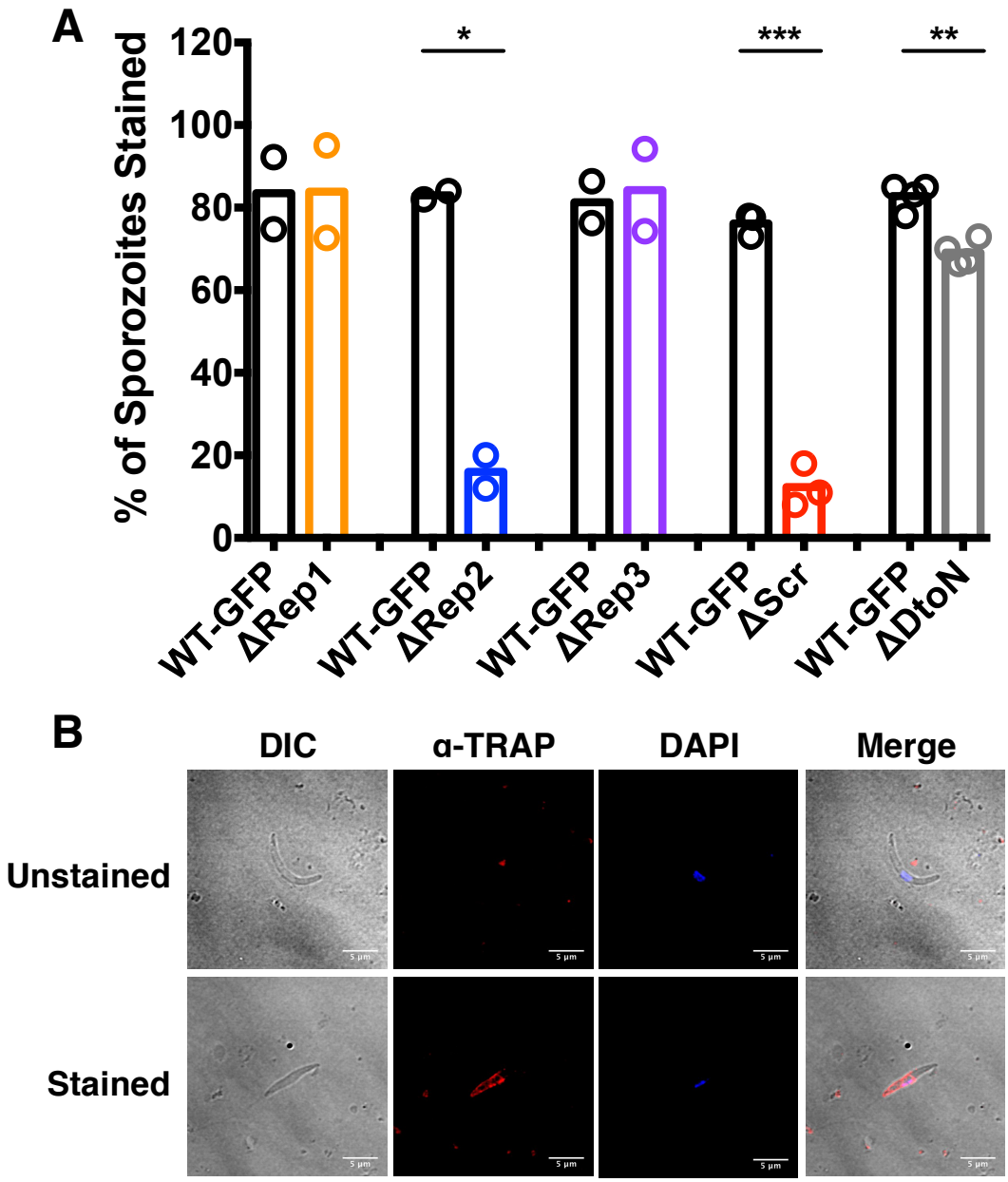

Figure 2.18: TRAP Staining of Motile Sporozoites. Salivary gland sporozoites were allowed to glide for 1 hour before fixation and staining for TRAP without permeabilization. A) Percent of sporozoites stained with TRAP after gliding with matched WT-GFP controls. Dots represents an independent mosquito cycle. n=100 sporozoites, Unpaired t-test: $p<0.05$. C) Representative examples of unstained and stained sporozoites after gliding with TRAP staining, DAPI, DIC and merge images shown.

could not be analyzed in this assay, so we focused on circular gliding sporozoites (Figure 2.20). We defined an adhesion turn over event as an adhesion site forming at the anterior end of the sporozoite, translocating to the posterior end, and finally disassembling (Figure 2.19B). The number of these events per movie (2.5 minutes) was quantified and we found that adhesion site turnover in ΔRep2, and ΔScr was decreased, with fewer turn over events per unit time (Figure 2.19C).

We then went on to dissect adhesion site assembly and disassembly in the CSP repeat mutants. By observing RICM movies frame-by-frame we binned each time point as an assembly, disassembly, or multiple adhesion site phase (Figure 2.21A). Analysis of adhesion site assembly and disassembly with WT-GFP sporozoites, showed that they spend ∼70% of gliding time with multiple adhesion sites (Figure 2.21B). We hypothesized that if mutant lines spent more time with small adhesion sites, they had an assembly defect, because it takes longer to develop larger adhesion sites and if they spent more time with large adhesion sites, then they had a disassembly phenotype, because it takes them longer to break down adhesion sites (Figure 2.21A). We found a subtle phenotype with ΔRep2 and ΔScr sporozoites spending more time with small adhesion sites and less time with multiple adhesion sites, as compared to WT-GFP (Figure 2.21), suggesting they had an adhesion site assembly defect. No defects were seen in disassembly (Figure 2.21D) and surprisingly, ΔDtoN sporozoites showed no defect in adhesion site dynamics (Figure 2.19 & 2.21).

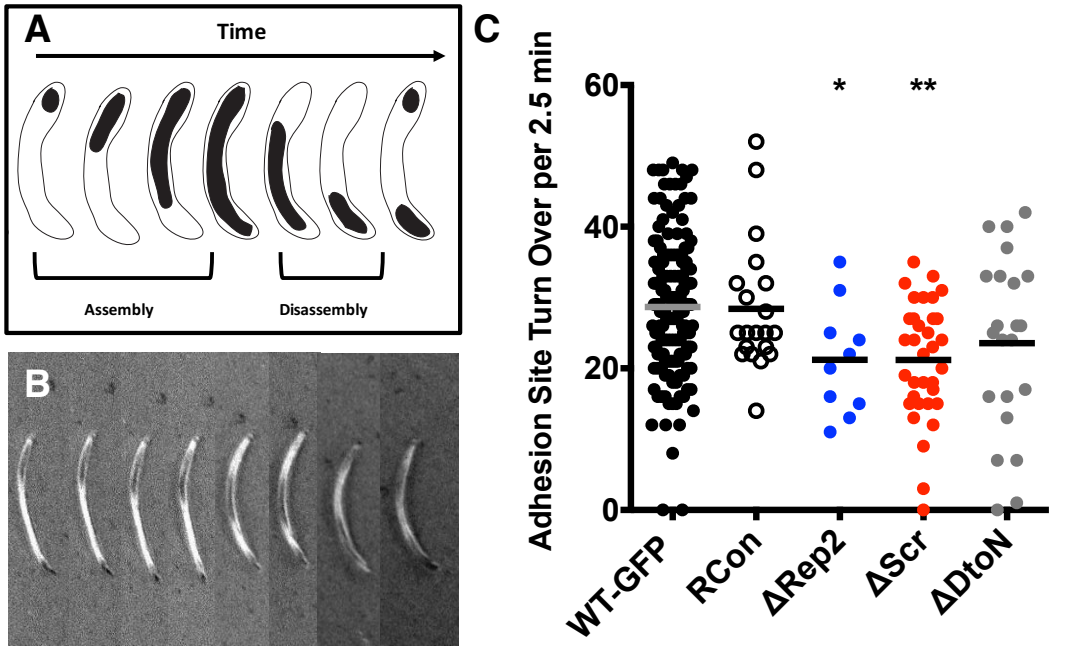

Figure 2.19: CSP Repeat Mutants with Defective Adhesion Site Dynamics. A) Cartoon of adhesion site cycle during gliding motility. Adhesion sites indicated in black. Periods of adhesion site assembly and disassembly are indicated. B) Example of adhesion site (black) moving from anterior to posterior end of sporozoite during productive gliding. Parasite aligned and repositioned so that change in adhesion site location along the length of the sporozoite is clear. C) Number of adhesion turn over events (adhesion site moving from anterior to posterior end) per movie/parasite. Student's t-test, $p<0.05$. Data from $\geq$3 independent experiments are pooled with the following number of parasites for each line: WT-GFP=169, RCon=20, ΔRep2=10, ΔScr=34, ΔDtoN=22.

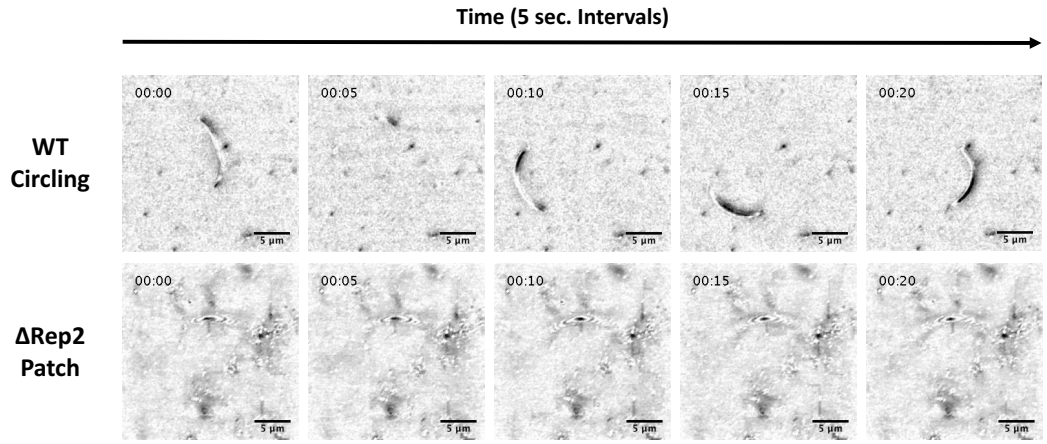

Figure 2.20: Adhesion Site Turn Over in Productive and Non-Productive Gliding. Examples of adhesion sites (black) in a WT, productive, circular gliding parasite (top) and a ΔRep2, non-productive, patch gliding parasite (bottom). Images are still frames from movies, every 5 seconds for 20 seconds.

2.3.6 Single Molecule Studies of the CSP Repeats

Lastly, we investigated whether the CSP repeats have structural properties which are similar to those found in elastomeric proteins. Interestingly, CSP repeats have features in common with elastomeric proteins such as spider silk, titin, and abductin [26]. These proteins are difficult to crystallize due to flexibile repeats, high in proline and glycine content [26]. Elastic regions frequently have a β-turn conformation and the length of the repeat region is important for function/mechanical properties [26]. Finally, these proteins usually crosslink to form a network and are defined by their ability to unfold and fold without energy loss or protein rupture [26]. The currently available data on the CSP repeats fit these criteria: 1) a few peptide structure studies have suggested the CSP repeats have a β-turn conformation [5–9], 2) CSP repeats are high in proline or glycine content and 3) the density of CSP on the

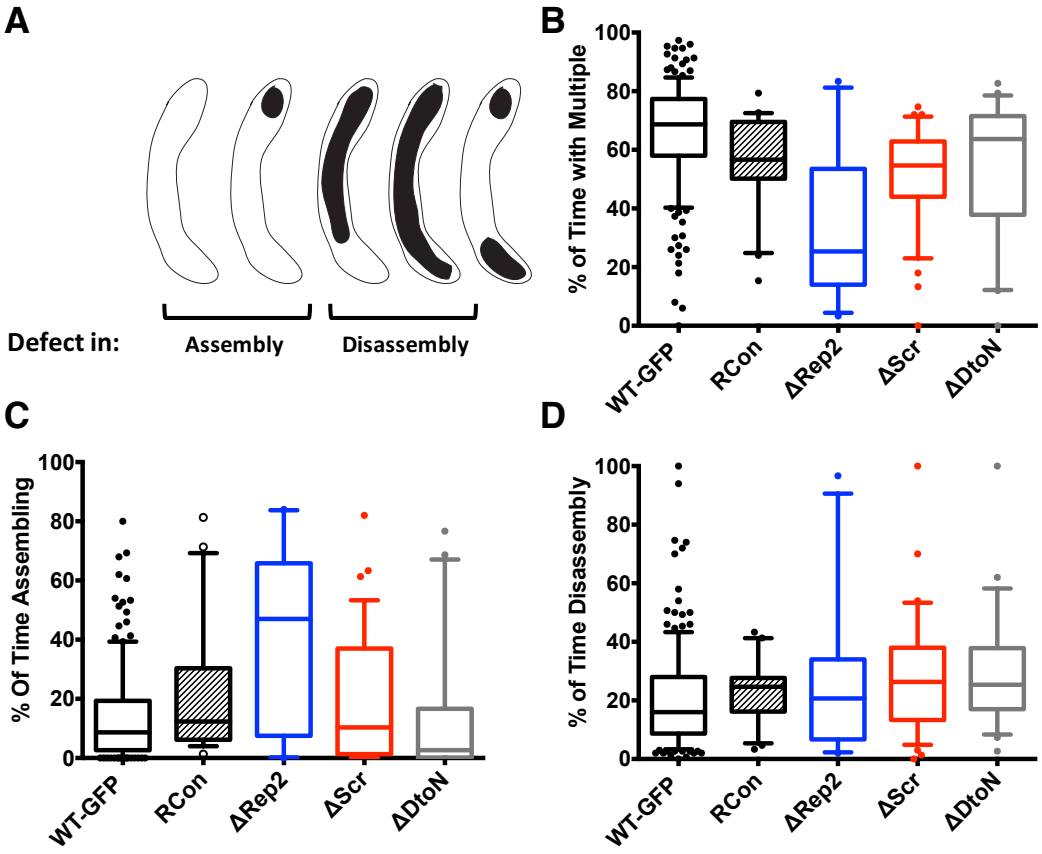

Figure 2.21: CSP Repeat Mutants with Defective Adhesion Site Assembly. Quantification of sporozoite adhesion "states" as seen in frames of each movie. Percent of time spent in each state was quantified by going frame-by-frame of RICM movies and binning sporozoites as having one small adhesion site (<50% of the sporozoite body length), one large adhesion site (>50% of the sporozoite body length), or multiple adhesion sites. A) Cartoon showing that an increase in the amount of time parasites spent with small or large adhesion sites indicate defects in assembly or disassembly respectively. B-D) Box-and-whisker plots of quantification of percent of time with B) multiple sites, C) assembling, or D) disassembling adhesion sites. Plots are with 10-90th percentile, horizontal line inside the box is the median and dots are outliers. Data from 3 experiments are pooled with the following number of parasites for each parasite line: WT-GFP=169, RCon=20, ΔRep2=10, ΔScr=34, ΔDtoN=22.

surface, could lend itself to crosslinking. To interrogate the elastic properties of the repeats, we utilized optical tweezers for single-molecule force spectroscopy (SMFS) on repeat peptides as previously performed for spider silk [20]. In these experiments, FRET signal is measured by flanking the peptide of interest between a Cy3 and Cy5 fluorophore. One end of the peptide-fluorophore product is conjugated to biotin and immobilized on a substrate containing avidin while the other end is conjugated to digoxigenin and is bound by an anti-digoxigenin bead in an optical trap (Figure 2.6). Upon moving the microscope stage, force is applied to the peptide and peptide extension can be measured by changes in the FRET signal. When the peptide is relaxed the FRET signal is high, as the Cy3 and Cy5 are in close proximity. However, upon application of force and stretching of the peptide, the fluorophores move apart with measurable loss of FRET signal (Figure 2.6).

To assess the elasticity of the CSP repeats, we compared the FRET signals of the stretch and relax phases of peptide pulling. If CSP repeat peptides were elastic, then the FRET signal from the stretch and relax phases of pulling should overlap due to energy conservation. We find that the WT peptide has complete overlap of FRET signal between the stretch and relax phases, in contrast, the scrambled peptide had a relax phase with a lower FRET signal than the stretch phase, indicating that the peptide was less compact after pulling and energy was lost (Figure 2.22). Together these data suggest that the CSP repeats region has properties of an elastic spring and that the elasticity of the region is dependent on the repeated amino acid sequence. These data are in agreement with another study which used an atomic force spectroscopy

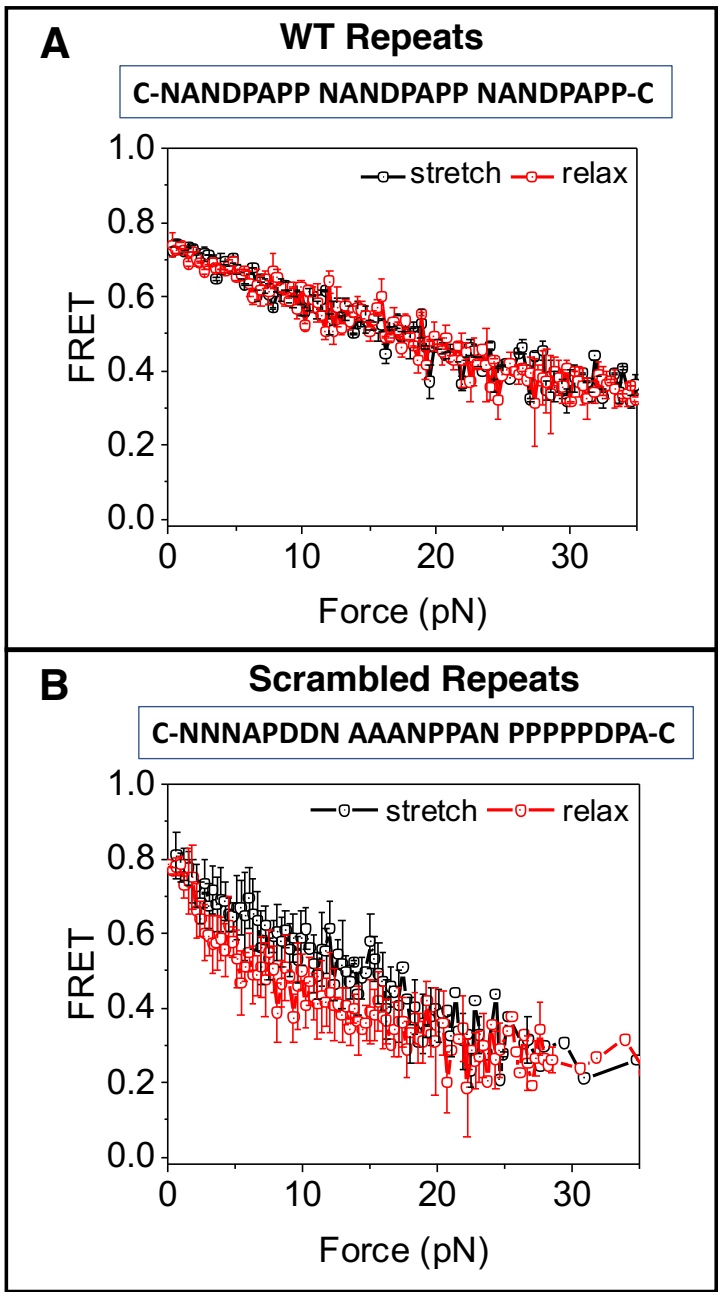

Figure 2.22: Single Molecule Force Spectroscopy of CSP Repeat Peptides. A) WT and B) scrambled CSP repeat sequences were synthesized and prepared for SMFS studies as indicated in the methods. Peptide sequences for the WT and scrambled construct are boxed at the top of each panel with the data corresponding to those peptides below their respective peptide sequence. FRET signal during stretch (black) and relax (red) phases of peptide pulling. WT peptide: n=22. scrambled peptide: n=5. Error bars are standard error of the data.

(AFM) approach to suggest an elastic CSP repeat region [27]. In this study the constructs used for AFM had I27 domains from titin flanking the CSP repeats in order to provide a molecular fingerprint in the stress-strain curves so that the peaks associated with the CSP repeats could be identified [27]. However, they found that the CSP repeats unfolded before the I27 bands, meaning that contributions of the I27 domains on the CSP data cannot be confidently excluded [27]. As our constructs have no such domains, we can confidently extrapolate the mechanical properties of the CSP repeats.

2.4 Discussion

2.4.1 Interpretation of Results

Using a mutagenesis approach to probe CSP repeat region function *in vivo*, we present the first evidence that the CSP repeats have a functional role in sporozoite biology. Our data demonstrate that the CSP repeats serve as a functional linker between the two terminal domains of CSP and is required for sporozoite motility and infectivity.

WT salivary gland sporozoites have a masked TSR domain and exposed N-terminus, until reaching the liver, at which point the the N-terminus is cleaved, exposing the TSR [14]. However, we found that ΔRep2 salivary gland sporozoites had diminished N-terminal domain exposure and enhanced TSR exposure compared to WT-GFP controls, which was not explained by CSP cleavage (Figures 2.11 & 2.12). The ΔRep2 truncation, which removes ∼50% of the repeats, suggests that there is a length requirement for masking of the TSR in salivary gland sporozoites, as the ΔRep1 and ΔRep3 truncations, which

remove ∼25% of the repeats, had no alteration in domain exposure (Figure 2.11). In field isolates, the number of CSP repeats can vary up to ∼12% of the repeat length and modeling of repeat region length has suggested that length may be important for stabilizing repeat region structure [28, 29]. Thus, it seems the repeats can tolerate small truncations, but require at least 75-90% of its length to maintain structural features.

Before these studies, the function of the repeats was unappreciated, and the region was believed to serve as an immunological decoy. While previous studies have shown that upon incubation with Fab monomers targeting the repeats, sporozoite motility was inhibited [30], there was no known linker between CSP and the motor complex, and thus CSP was not thought to play a role in parasite motility. Here we show that the CSP repeats are critical for sporozoite motility.

The predominant phenotype of the CSP repeat mutants is a diminished capacity to glide productively. The ΔRep2, ΔScr, and ΔDtoN have an enhanced proportion of sporozoites waving or patch gliding (Figure 2.15). Substantial defects in infectivity of both the mosquito salivary glands and the mouse liver in these mutants (Figures 2.8, 2.2, 2.13, & 2.14) are likely due to the the higher proportion of sporozoites which are incapable of productive motility.

WT sporozoites predominately glide productively (∼90%) (Figure 2.15C), due to the maturation of motility machinery [31]. The few WT sporozoites which do not display productive motility, have likely not fully developed and thus exhibit slower speeds (Figure 2.17) [31, 32]. However, CSP repeat mutants which predominately move non-productively, ΔRep2 and ΔScr, move

faster than patch gliding WT sporozoites (Figure 2.17), and those that do move productively are capable of reaching maximum speeds comparable that of WT (Figure 2.16), suggesting these parasites have fully developed their motility machinery, but lack the capacity to utilize it.

To determine the mechanisms leading to defects in CSP repeat mutant motility, we probed the behavior of adhesion sites in these mutants utilizing two approaches: 1) a TRAP immunofluorescence assay (IFA) and 2) RICM of circular gliding sporozoites. The TRAP IFA suggests that ΔRep2, ΔScr, and ΔDtoN do not properly organize adhesion sites as clusters of TRAP were not seen on the surface of gliding sporozoites, as is seen in WT-GFP sporozoites or CSP repeat mutant lines without gliding phenotypes (Figure 2.18). TRAP is believed to be the dominant adhesin of mature adhesion sites during productive sporozoite motility, and thus, it is likely that disorganization of TRAP on the surface would lead to defective motility. Upon imaging of adhesion sites using RICM, we found that circling ΔRep2 and ΔScr turn over their adhesion sites at a slower rate than WT-GFP or RCon sporozoites, suggesting that even when these sporozoites move productively there are defects in adhesion site assembly or disassembly (Figure 2.19). Upon quantification of adhesion site state, we found evidence for defects in adhesion site assembly due to the increased amount of time these CSP repeat mutant sporozoites spent with one small adhesion site and less time with multiple adhesion sites (Figure 2.21). Taken together, we hypothesize that those CSP repeat mutants which exhibit enhanced non-productive motility do so as a result of defects in adhesion site assembly.

To better understand how the CSP repeat mutants might function in adhesion site assembly we probed structural features of the repeats, under the hypothesis that the repeats may be elastic. Through SMFS of small repeat peptides, we found that the repeats are likely compact and elastic and that the repeated organization of amino acids was critical for maintaining elasticity (Figure 2.22). Exactly why the elasticity of the repeats are involved in adhesion site assembly or dynamics is not answered by this study, but these properties may be important for protein organization on the surface or energy storage during motility. Further studies are required to determine the exact mechanism.

2.4.2 Limitations and Future Studies

The interpretation of our results is limited by our current understanding of sporozoite motility and molecular biology. This study emphasizes the need to dissect parasite surface proteins, interacting partners, and the motility machinery. Of particular interest, would be the composition of adhesion sites. The sporozoite likely utilizes different types of adhesion sites to attach and glide in 2D assays. This is supported by parasites which show no defect in sporozoite attachment to the substrate, but do not turn over adhesion sites or move productively (ΔRep2 and ΔScr) (Figure 2.15 & 2.20) [22, 23]. Identifying what proteins compose an adhesion site used for sporozoite attachment versus those that compose an adhesion site for productive motility would greatly enhance our understanding of parasite motility. To do so requires characterization of sporozoite surface proteins for the identification of candidate adhesins

and a recent sporozoite surface proteome provides a starting point for these studies [33].

Due to these limitations, we cannot differentiate direct versus indirect effects of CSP on sporozoite motility. As CSP coats the sporozoite surface, it is likely to dramatically influence the other proteins on the surface of the sporozoite, and thus if CSP conformation or organization is perturbed, adhesion site maturation could be affected, a hypothesis that is supported by our TRAP IFAs and RICM studies (Figure 2.18 & 2.21). However, it is also possible that CSP, or even the repeats, are directly interacting with the substrate such that in our mutants, the perturbation of the repeats leads to defective substrate interactions and motility. Future studies will be required to dissect sporozoite-substrate molecular interactions as well as the intermolecular interactions on the sporozoite surface in order to differentiate between these possibilities.

2.5 Appendix: Additional Information

2.5.1 Troubleshooting Molecular Cloning of Repeats

CSP repeat mutant transformation attempts into the bacterial cell line typically used in our lab (XL10 Gold) were frequently unsuccessful with no colonies developing after overnight incubation or large deletions in the recovered plasmids. Alternative cell lines (DH5α, NEB C4030I, SURE2, and PMC103) were tried and many trial and error attempts were made with each cell line, modifying ligation and culturing conditions. Ultimately, continual troubleshooting was required, with careful sequencing of plasmids, before successful molecular cloning was achieved with each vector. No cell line was clearly optimal for

all CSP repeat vectors.

2.5.2 CSP Repeat Mutants in Brightly Fluorescent Parental Line

Due to the motility phenotypes of the CSP repeat mutants, we wanted to observe mutant parasite motility *in vivo*. However, to do so required a brighter, fluorescent parasite line than the 507 cl1 line (expressing GFP under the *eef1-α* promoter). Our lab has previously generated a *P. berghei* expressing mCherry under the *uis4* promoter, which is selection marker-free for intravital imaging [34]. We aimed to generate the CSP repeat mutants in this fluorescent line so that we could study their motility *in vivo*. However, all attempts to do so were unsuccessful. Interestingly, these transfection attempts all seemed to have recombinants which had integrated the construct, but had repaired the repeats back to WT sequence. We observed a similar problem when using a smaller 3' UTR (500 bp vs. 1.5 kbp) for transfections into the 507cl1 line. We hypothesize that the background genome of the mCherry expressing line was refractory to repeat region mutations as a CSP recombinant control and a CSP N-terminal deletion mutant were previously made in this line [34]. We hypothesized that an endonuclease specific for repeat region maintenance could have a mutation or altered expression in the mCherry line in comparison to the 507 cl1 line. In a paper by Verstrepen et al., they show that FLAP endonuclease 1 is responsible for maintenance or repeats in yeast [35]. By blasting the FLAP endonucelase 1 amino acid sequence from yeast to that of *Plasmodium*, I found a homologue, FEN1, that is currently annotated as the FLAP endonuclease 1 in PlasmoDB. I also found FEN1 to be conserved across all *Plasmodium* and Apicomplexa

genomes currently available.

Under the hypothesis that FEN1 may be different between our *P. berghei* lines, we sequenced FEN1 in the 507 cl1 parental line as well as four clones from transfections in either the 507cl1 or the mCherry lines. No obvious differences were seen in the sequence, but clean reads through the entire open reading frame were not achieved. If these studies are of interest, follow up should include: 1) further sequencing for clean reads 2) analysis of FEN1 expression between different lines and 3) a knock-out study of FEN1. We received a a knockout construct from PlasmoGEM which we have not yet utilized, but could be used for these purposes.

2.5.3 ΔScr Clonal Variation

Initial clones acquired from the first ΔScr transfection exhibited a stronger phenotype than that observed in the subsequent transfection clones described above. Given the phenotypes of the subsequent transfection clones, we believe the background genome of the initial transfection parental line had alterations compounding the ΔScr phenotype. The unique phenotype of these original ΔScr lines was lower oocyst numbers (Figure 2.23A), which lead to lower midgut and hemolymph sporozoite numbers (Figure 2.23B). However, similar to the other ΔScr clones, no defects in oocyst morphology or sporozoite development were observed, and we showed that lower midgut and hemolymph sporozoite numbers were due to lower oocyst numbers (Figure 2.23 C-E). In addition, these clones showed enhanced defects in salivary gland invasion

(Figure 2.23 D & E) and enhanced defects in motility and infectivity in comparison to the subsequent ΔScr clones. Thus, we hypothesize that these original ΔScr clones had one or more unintended mutations in the background genome and the population expanded after a bottleneck of the parasite population during drug selection.

2.5.4 Anti-C terminal Antisera and CSP Repeat Mutant Western Blots

The CSP anti-C terminal antisera used in the CSP immunofluorescence assays was also tested by western blot on several of the CSP repeat mutants. However, this antisera showed detection of an additional CSP band for ΔRep3 and ΔRep2 lysates, which we were unable to interpret (Figure 2.24). Interestingly, this band runs at the same MW in both the ΔRep2 and ΔRep3 samples, just below the cleaved form of WT CSP. This band was not detected in ΔRep1 samples and was not tested for with ΔDtoN or ΔScr parasites. Detection of CSP by western blot with this antisera has previously demonstrated abnormal banding patterns in WT midgut sporozoites, likely due to additional cleavage products or to cross-reactivity to another TSR-domain containing protein. However, as 3D11 does not recognize the additional band, one could also hypothesize that this band is the result of a cleavage product in which everything 5' of the C-terminus was removed, but this band migrates higher than the N-terminal cleavage product, which should have a higher molecular weight. Thus, the identity of this band would be an interesting area of study in order to better understand CSP conformation, function, and processing.

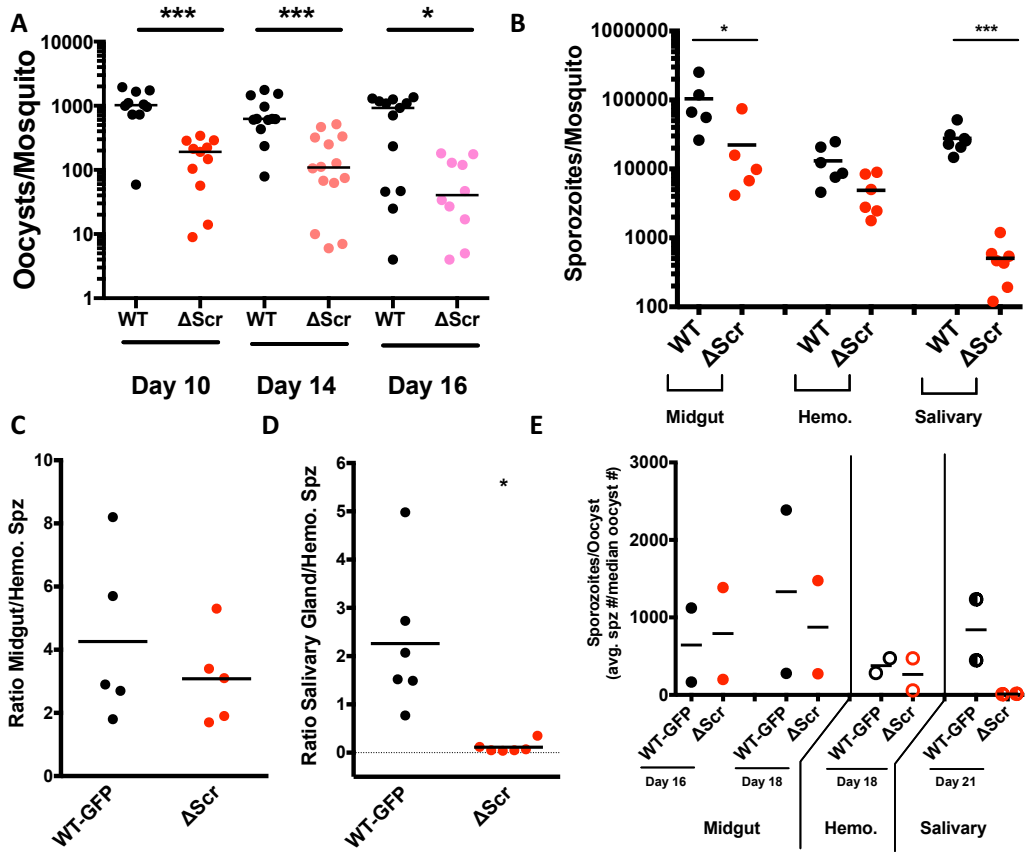

Figure 2.23: Unique Oocyst Phenotype of Initial ΔScr Clones One and Two. A) Representative mosquito cycle, in which oocysts numbers followed over several days. Mann-Whitney Test: $p \leq 0.05$. B) Midgut, hemolymph (Hemo.), and salivary gland (Salivary) sporozoites per mosquito in these clones with matched WT-GFP controls. Paired t-test: $p \leq 0.05$. C) Ratio of midgut sporozoites to hemolymph sporozoites from cycles in which sporozoite numbers were taken from both stages. This is a measurement of the efficiency of sporozoite exit from oocysts. Paired t-test: $p \leq 0.05$. D) Ratio of salivary gland sporozoites to hemolymph sporozoites from cycles in which sporozoite numbers were taken from both stages. This is a measurement of efficiency of sporozoite invasion of salivary glands. Paired t-test, $p \leq 0.05$. E) Sporozoite number per oocyst is shown for midgut, hemolymph, and salivary gland sporozoites. Paired t-test, $p \leq 0.05$.

2.5.5 RICM Automated Analysis of Adhesion Sites

In attempts to analyze the RICM data presented above, I wanted to generate an automated mechanism of adhesion site detection and measurement. To do so, I used Fiji to create macro routines, which would remove background and threshold so that only adhesion sites were remaining, and could then be measured (area). However, I was unable to achieve consistent, reliable results. This was primarily due to differences in background between, and even within movies. Additional problems came from mosquito debris in the field of view, but I was able to generally handle this by manually removing areas with mosquito debris from the movie before running the macro. Thus, as I was unable to attain direct size measurements of adhesion sites, I attempted

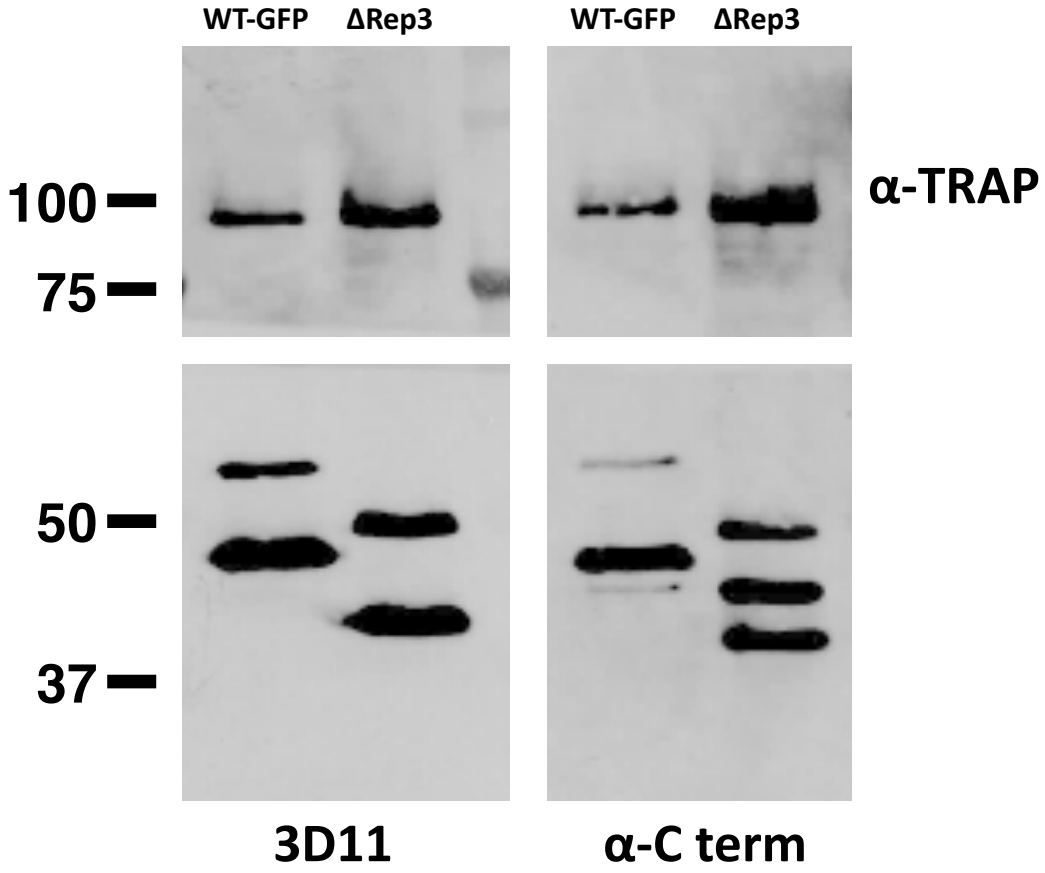

Figure 2.24: Extra CSP Band Detected in Repeat Mutants by anti-C Terminal Antisera. Western Blot of samples WT-GFP or ΔRep3 sporozoite lysate run side by side and detected with either 3D11 (targets CSP repeats) or α-C terminal antisera and TRAP loading controls.

other manual mechanisms of extrapolating information about adhesion site size and dynamics as described in the main text above. These methods were largely supported by Dr. Freddy Frischknecht, who provided many ideas and insight into how to handle these data.

References

1. Zavala, F. *et al.* Rationale for development of a synthetic vaccine against Plasmodium falciparum malaria. *Science* **228,** 1436–1440 (1985).
2. Kemp, D. J., Coppel, R. L. & Anders, R. F. Repetitive proteins and genes of malaria. *Annual Reviews Inc.* **41,** 181–208 (1987).
3. Espinosa, D. A. *et al.* Development of a chimeric Plasmodium berghei strain expressing the repeat region of the P. vivax circumsporozoite protein for in vivo evaluation of vaccine efficacy. *Infection and Immunity* **81,** 2882–2887 (2013).
4. Persson, C. *et al.* Cutting Edge: A New Tool to Evaluate Human Pre-Erythrocytic Malaria Vaccines: Rodent Parasites Bearing a Hybrid Plasmodium falciparum Circumsporozoite Protein. *The Journal of Immunology* **169,** 6681–6685 (2002).
5. Ghasparian, A., Moehle, K., Linden, A. & Robinson, J. A. Crystal structure of an NPNA-repeat motif from the circumsporozoite protein of the malaria parasite Plasmodium falciparum. *Chemical Communications* **2,** 174–176 (2006).
6. Fasman, G. D., Park, K. & Schlesinger, D. H. Conformational analysis of the immunodominant epitopes of the circumsporozoite protein of Plasmodium falciparum and knowlesi. *Biopolymers* **29,** 123–130 (1990).
7. Dyson, H. J., Satterthwait, A. C., Lerner, R. A. & Wright, P. E. Conformational preferences of synthetic peptides derived from the immunodominant site of the circumsporozoite protein of Plasmodium falciparum by proton NMR. *Biochemistry* **29,** 7828–7837 (1990).
8. Plassmeyer, M. L. *et al.* Structure of the Plasmodium falciparum circumsporozoite protein, a leading malaria vaccine candidate. *Journal of Biological Chemistry* **284,** 26951–26963 (2009).

9. Verdini, A. S., Chiappinelli, L. & Zanobi, A. Toward the elucidation of the mechanism of attachment and entry of malaria sporozoites into cells: synthetic polypeptides from the circumsporozoite protein of Plasmodium falciparum bind Ca2+ and interact with model phospholipid membranes. *Biopolymers* **31,** 587–594 (1991).

10. Armali, G. E. *et al.* Conformation and immunogenicity of engineered repeating segment of the circumsporozoite surface protein of Plasmodium falciparum. *Molecular and Biochemical Parasitology* **38,** 135–140 (1990).

11. Topchiy, E. & Lehmann, T. Chelation of Ca2+ ions by a peptide from the repeat region of the Plasmodium falciparum circumsporozoite protein. *Malaria Journal* **13,** 195 (2014).

12. Ferguson, D. J. P. *et al.* The repeat region of the circumsporozoite protein is critical for sporozoite formation and maturation in Plasmodium. *PLoS One* **9** (2014).

13. Coppi, A., Pinzon-Ortiz, C., Hutter, C. & Sinnis, P. The Plasmodium circumsporozoite protein is proteolytically processed during cell invasion. *The Journal of Experimental Medicine* **201,** 27–33 (2005).

14. Coppi, A. *et al.* The malaria circumsporozoite protein has two functional domains, each with distinct roles as sporozoites journey from mosquito to mammalian host. *Journal of Experimental Medicine* **208,** 341–356 (2011).

15. Yoshida, N., Nussenzweigt, R. S., Potocnjak, P., Nessenzweig, V. & Aikawa, M. Hybridoma produces protective antibodies directed against the sporozoite stage of malaria parasite. *Science* **207,** 71–73 (1980).

16. Tsuji, M., Mattei, D., Nussenzweig, R. S., Eichinger, D. & Zavala, F. Demonstration of heat-shock protein 70 in the sporozoite stage of malaria parasites. *Parasitology Research* **80,** 16–21 (1994).

17. Ejigiri, I. *et al.* Shedding of TRAP by a rhomboid protease from the malaria sporozoite surface is essential for gliding motility and sporozoite infectivity. *PLoS Pathogens* **8** (2012).

18. Janse, C. J., Ramesar, J. & Waters, A. P. High-efficiency transfection and drug selection of genetically transformed blood stages of the rodent malaria parasite Plasmodium berghei. *Nature Protocols* **1,** 346–356 (2006).

19. Bruna-Romero, O. *et al.* Detection of malaria liver-stages in mice infected through the bite of a single Anopheles mosquito using a highly sensitive real-time PCR. *International Journal of Parasitology* **208,** 341–356 (2011).

20. Brenner, M. D. *et al.* Spider silk peptide is a compact, linear nanospring ideal for intracellular tension sensing. *Nano Letters* **16,** 2096–2102 (2016).

21. Menard, R. *et al.* Circumsporozoite protein is required for development of malaria sporozoites in mosquitoes. *Nature* **385,** 336 (1997).

22. Bane, K. S. *et al.* The actin filament-binding protein coronin regulates motility in Plasmodium sporozoites. *PLoS Pathogens* **12,** e1005710 (2016).

23. Sultan, A. A. *et al.* TRAP is necessary for gliding motility and infectivity of Plasmodium sporozoites. *Cell* **90,** 511–522 (1997).

24. Vanderberg, J. P. Studies on the Motility of Plasmodium Sporozoites. *The Journal of Protozoology* **21,** 527–537.

25. Weber, I. in *Methods in Enzymology* 34–47 (Academic Press, 2003).

26. Tatham, A. S. & Shewry, P. R. Elastomeric proteins: biological roles, structures and mechanisms. *Trends in Biochemical Sciences* **25,** 567–571 (2000).

27. Patra, A. P., Sharma, S. & Ainavarapu, S. R. K. Force spectroscopy of the Plasmodium falciparum vaccine candidate circumsporozoite protein suggests a mechanically pliable repeat region. *Journal of Biological Chemistry* **292,** 2110–2119 (2017).

28. Gandhi, K. *et al.* Variation in the circumsporozoite protein of Plasmodium falciparum: vaccine development implications. *PloS one* **9,** e101783 (2014).

29. Escalante, A. A. *et al.* A study of genetic diversity in the gene encoding the circumsporozoite protein (CSP) of Plasmodium falciparum from different transmission areasâĂŤXVI. Asembo Bay Cohort Project. *Molecular and biochemical parasitology* **125,** 83–90 (2002).

30. Stewart, M. J., Nawrot, R. J., Schulman, S. & Vanderberg, J. P. Plasmodium berghei sporozoite invasion is blocked in vitro by sporozoite-immobilizing antibodies. *Infection and Immunity* **51,** 859–864 (1986).

31. Hegge, S., Kudryashev, M., Smith, A. & Frischknecht, F. Automated classification of Plasmodium sporozoite movement patterns reveals a shift towards productive motility during salivary gland infection. *Biotechnology Journal* **4,** 903–913 (2009).

32. Khater, E. I., Sinden, R. & Dessens, J. T. A malaria membrane skeletal protein is essential for normal morphogenesis, motility, and infectivity of sporozoites. *Journal of Cell Biology* **167,** 425–432 (2004).

33. Lindner, S. E. *et al.* Total and putative surface proteomics of malaria parasite salivary gland sporozoites. *Molecular & Cellular Proteomics* **12,** 1127–1143 (2013).

34. Hopp, C. S. *et al.* Longitudinal analysis of Plasmodium sporozoite motility in the dermis reveals component of blood vessel recognition. *eLife* **4,** e07789 (2015).

35. Verstrepen, K. J., Jansen, A., Lewitter, F. & Fink, G. R. Intragenic tandem repeats generate functional variability. *Nature Genetics* **37,** 986–990 (2005).

Chapter 3

2-Photon Intravital Imaging of Sporozoites in the Dermis

3.1 Introduction

The skin stage of malaria provides a promising target for vaccine control strategies as sporozoites spend up to several hours in the skin before finding a blood vessel and infecting the liver [1]. Indeed it is in the skin that the malaria parasite is extracellular for the longest period of time in the mammalian host. Additionally, a mosquito bite site is the only point in the malaria life cycle in which all three organisms interact: the host, the parasite, and the vector. Strategies targeting each of these organisms during parasite transmission can be designed to prevent infection, but to target transmission, we must first understand the host-parasite interactions of the skin phase of infection.

As indicated in the introduction some of the most informative work on sporozoites in the skin have utilized intravital microscopy to observe sporozoite behavior [2, 3]. Nonetheless, these studies have been constrained by

the limitations of acquisition speed as well as methods of parasite inoculation. The exceptional speed of sporozoites ($\sim$1-2 μm\second) means that to observe their motility in the skin, rapid acquisition speeds must be achieved. However, the 3D environment of the skin, provides the additional challenge of capturing the entire volume of the tissue, 80 μm, at these fast acquisition rates. Additionally, choosing the ideal methodology of sporozoite inoculation for imaging can be challenging. Mosquito bite studies are extremely difficult, as mosquitoes will not always bite, the number of sporozoites inoculated is not controlled, and one cannot reliably image bite sites immediately after mosquito probing. To overcome these limitations, our lab has utilized intradermal inoculation with a micro-syringe (World Precision Instruments, Nanofil syringe (#nanofil) with 36-gauge needle, #NF36BV) which provides reliable imaging sites [2]. However, these needles are about five times larger than the mosquito proboscis (Figure 3.1), and even with small volumes of inoculation, such as 0.2 μL, a non-physiological amount of fluid is injected into the tissue, which will likely impact tissue architecture and parasite behavior.

The experiments described below were focused on developing a system that would mimic mosquito inoculation of malaria parasites into a mouse and observing parasites directly after inoculation. We made appropriately sized, fluorescently labeled glass micro-pipettes to inject sporozoites within the field of view (FOV) of the fluorescent scope and then directly observe the injection and dissemination of the parasites within the skin. We planned to then use this system to conduct intravital imaging of the CSP repeat mutants described in Chapter 2, but were unable to do so due to lack of brightly fluorescent

parasites. However, this method allows us to probe yet unexplored questions of the sporozoite skin stage. While our focus was on application of this approach for understanding parasite transmission in the skin, this simple, inexpensive, reusable, and versatile fluorescent glass micro-pipette can be used to target injections to a specific location and simultaneously visualize injections using fluorescent excitation microscopy providing functionality in a breath of fields.

The glass micro-pipette is a basic tool in numerous types of microscopy studies: injection of drugs, markers, and cells as well as cellular manipulations. A particularly challenging procedure is to conduct intravital micro-pipette manipulations under microscopic guidance, because the optical monitoring is limited by the optical density of the tissue. Intravital confocal or multiphoton fluorescence techniques are utilized for numerous applications in cancer biology, neuroscience, cell physiology and infectious disease. However, the typical glass micro-pipette is undetectable with fluorescence, making positioning under the microscope difficult. Previous studies have tried to solve this problem with quantum dot coated micro-pipettes [4]. However, this method has proved limited as it requires specialized chemistry and the quantum dots can be partially lost during insertion into tissue [4]. We sought to improve upon this technique to make a more robust, inexpensive and simple method for a diverse range of laboratory applications. To this end, we undertook a broad survey of methods for labeling glass micro-pipettes with fluorescent probes commonly used for intravital studies and compatible with multiphoton and confocal microscopy.

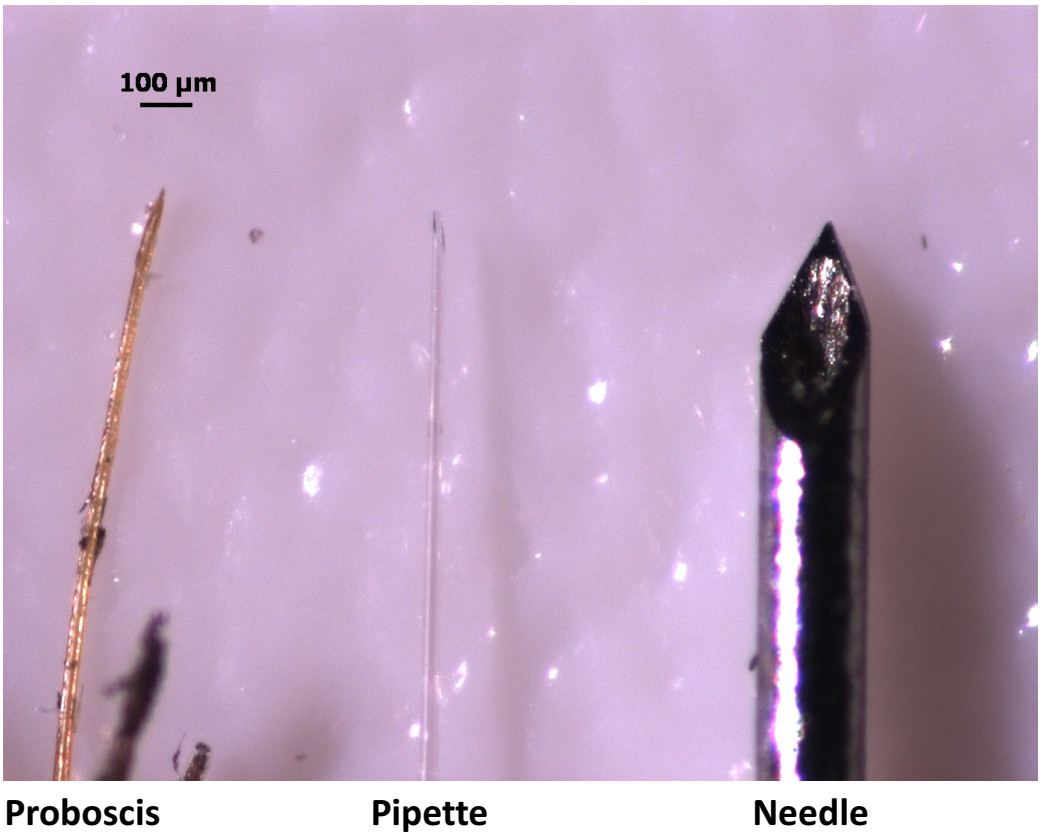

Figure 3.1: Mimicking the Mosquito Proboscis with Glass Pipettes. From left to right: mosquito proboscis, engineered glass pipette, and 36G needle previously used for intradermal inoculations. Scale bar = 100 μm.

3.2 Engineering Mosquito-mimic Glass Pipettes

We sought to attach or incorporate fluorescent moieties to glass micro-pipettes. Three strategies were evaluated for labeling glass pipets: fluorescent diamond incorporation into molten glass, ultraviolet (UV) curing glues, and heat curing enamels.

3.2.1 Fluorescent Coating of Micro-pipettes

Fluorescent nanodiamonds are an attractive fluorescent agent due to their high fluorescent efficiency as well as non-bleaching, non-blinking behavior [5]. Diamonds (80 to 90 nm diameter) for this study were obtained from Adamas Nanotechnologies with no chemical modifications. Difficulty arose in getting the diamonds to a sufficient density to use in a suspension of glue or enamel for application to the pipet. Since the diamonds are relatively heat stable we attempted another strategy, namely to attach the diamonds to the glass in a molten state. For this method, diamonds were concentrated in water and loaded into a micro-capillary tube by drawing the diamond solution into the capillary tube. Tubes with diamond solution were then dried at 100°C for several days until all water evaporated, leaving a concentrated diamond coating on the glass. The micro-forge element was placed over the dried diamond region within the pipet and pulled on a standard micro-forge (micro-forge setting and glass type see below). In the molten state the diamonds attached to the glass and were retained after vigorous washings with distilled water that removed the diamonds in the non-heated region of the pipet. This resulted in good but inconsistent internal labeling of the pipet as judged by

confocal microscopy using 638nm excitation and 2-photon microscopy using 980nm excitation (Figure 3.3). Thus, this approach might be most applicable for very small glass pipettes or microelectrodes where the probe efficiency is critical for detection, or where internal labeling is desired. This approach was not developed further for these pipettes.

3.2.1.1 UV Curable Glues

UV curable glues are used to bond glass structures via a UV catalyzed photoinitiator that generates local free radicals to initiate a polymerization process [6]. It was assumed that this approach could provide a robust attachment between the trapped fluorophore and the outer surface of the pipette [6]. Using UV curable glues varying from low (C.R. Laurence #UV601) to medium (C.R. Laurence #UV604L25) viscosities, as well as different UV curing conditions involving manipulation of coating methods, UV light source and coating times, we did not find these agents to provide a robust hard coating on the pipets. In addition, the UV curing bleached many of the fluorophores mixed into the glue. For these reasons this approach was abandoned.

3.2.1.2 Heat Cured Enamel

Heat cured enamels are commonly used to paint glass. We tried existing colored enamel that had intrinsic fluorescent properties as well as clear enamel to which we added well-characterized fluorophores. These enamels were then cured by heating the coated micro-pipette (190°C for 45 minutes). Overall, we found that this method was simple, gave uniform robust coating, was inexpensive and enabled a wide dynamic range of fluorescent emissions. It is

described in more detail below.

3.2.1.3 Fluorescent Enamel

Clear enamel (DecoArt, #DS89-30) was mixed with Alexa 488 (ThermoFisher, #A20000), 514 (ThermoFisher, #A30002), 532 (ThermoFisher, #A20001), or 610 (ThermoFisher, #A30050) succinimidyl ester dyes that were pretreated to cleave the ester bonds. These dyes are commercially available as hydrophobic esters for lipid membrane permeation that reduce maximum water solubility. To increase water permeability, the ester bonds were cleaved by hydrolyzing 1 mg dye in 0.5 mL 0.1 M HCl followed by 0.5 mL 0.1 M NaOH to neutralize the pH. Ester cleaved Alexa dyes were added to clear enamel (Decoart, #DS89-30) at a 1:1 ratio by volume and vortexed, resulting in a 0.5 mg dye/mL enamel:water. Enamel-Alexa solutions were stored at room temperature in the dark. Some colored enamel paints have intrinsic fluorescence. The best of those tested was the orange paint from the DecoArt Glass Paint Marker Multi-Pack (#13443247). It was brightly fluorescent and demonstrated a broad range of excitation and emission spectra (Figure 3.2). The orange enamel paint was diluted 1:50 or 1:100 in clear enamel paint prior to coating the pipets to optimize fluorescence intensity.

3.2.1.4 Coating Pipettes with Enamels

Pipettes were pulled from borosilicate glass capillary tubes (Sutter Instruments, #BF100-50-15) using a micro-forge (Sutter Instruments, #P-97) at the following settings: Heat=666, Pull=30, Velocity=120, Time=200, Pressure=200. Pulled pipettes were lightly coated in the different enamel mixtures by gently

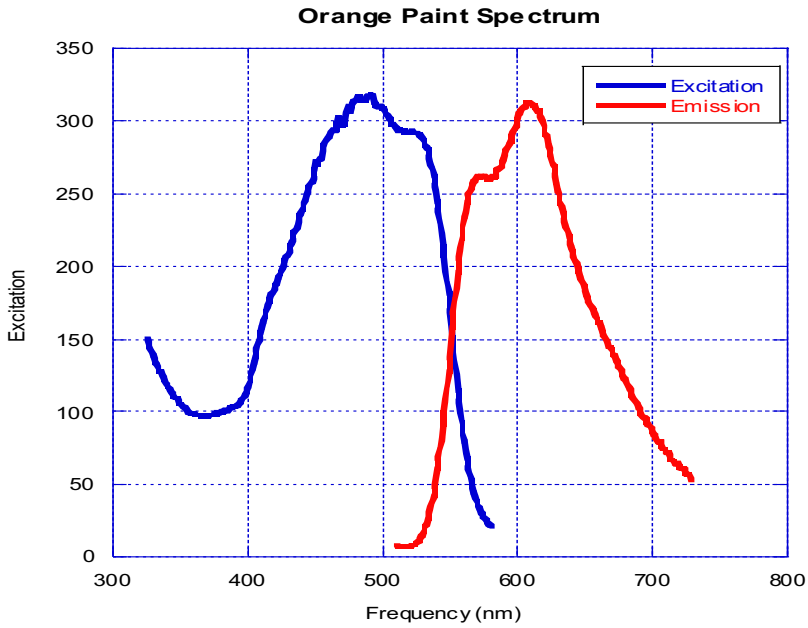

Figure 3.2: Emission Spectra of Orange Enamel. Emission spectra of the DecoArt orange enamel (#13443247) measured with a Shimadzu spectro fluorophometer (#RF-6000).

rolling the tip of the pipette in the paint. Coated pipettes were baked at 190°C for 45 minutes using a conventional oven and then allowed to cool at room temperature.

3.2.2 Pipette Shape

After cooling, the coated pipettes were beveled as previously described [6]. Briefly, pipettes were held at a 20° angle using a micromanipulator and brought down to a spinning hard drive that had been re-purposed by covering the hard drive with silicon carbide coated paper (Norton T402). A 20°

angle was found to be best suited for injection into the skin, however, other bevel angles can easily be made. Pipette tip size was confirmed to have a beveled opening between 60-65 μm and 30 μm wide which was comparable to the mosquito proboscis [7] and significantly smaller than the previously used 36-gauge needle (Figure 3.1). The robust nature of the coating was also demonstrated by the ability of the coated pipet to be beveled with no apparent damage to the fluorescent coating.

3.2.3 Imaging Pipettes

Pipettes coated with the heat cured enamels were imaged by confocal and 2-photon microscopy (Figures 3.3). In confocal, Alexa 488-enamel was excited using 488 nm excitation, Alexa 514-, 532-, and 555-enamels were exited at 514 nm excitation, and Alexa 610-enamel as well as the commercially available orange enamel were excited using 638 nm excitation. In 2-photon, 980nm excitation was used for all fluorophores. Emission in both the green (523-593nm confocal; 500-528nm 2-photon) and red (695-765nm confocal, 555-694nm 2-photon) spectra were collected.

To confirm durability of the pipettes, we inserted them into the dermis of a mouse ear 10 times monitoring the integrity of the coating (clear enamel with Alexa 514) between each trial. As seen in Figure 3.4, the coating was not affected by the insertions and was easily detected in the tissue after 10 trials. However, upon quantification of fluorescence intensity, we found that there is some loss of fluorescence after repeated injections as well as from photobleaching with extended imaging (Figures 3.5). This property permitted

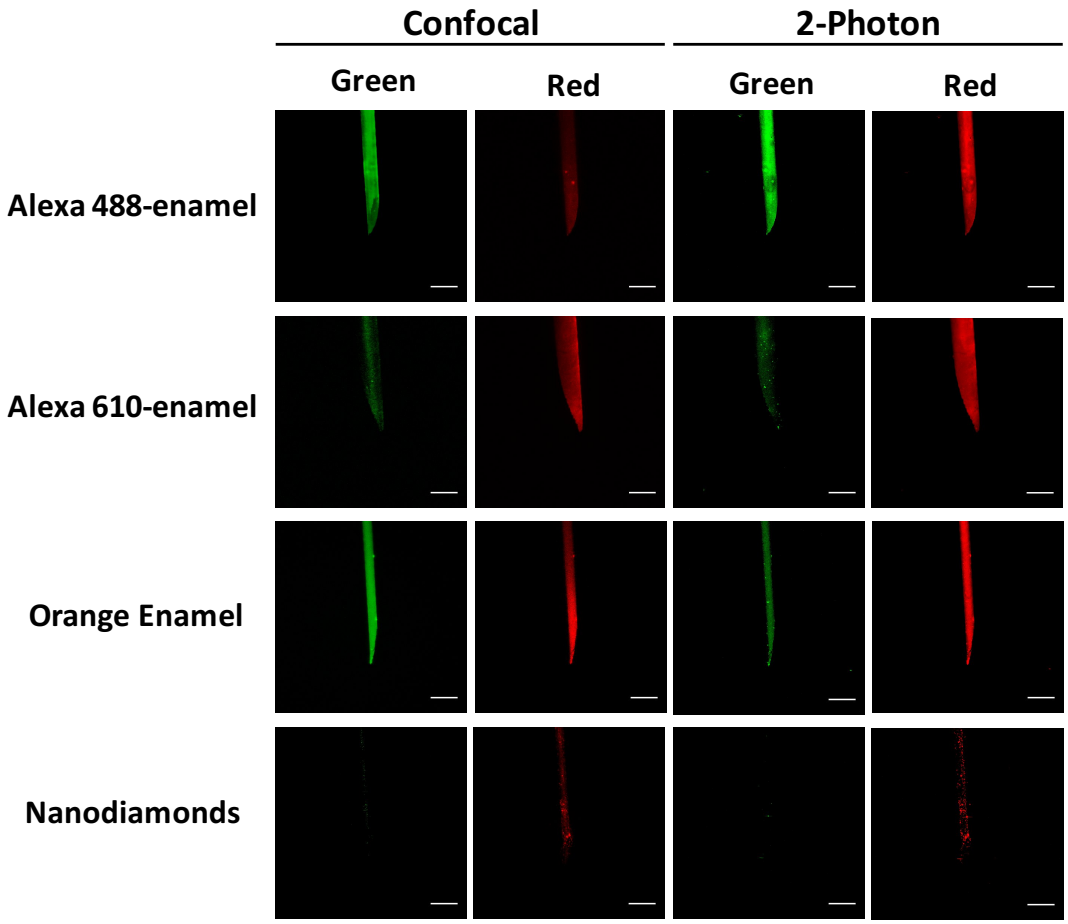

Figure 3.3: Fluorescently Labeled Pipettes. Representative labeled pipettes imaged by confocal and 2-photon microscopy. Pipettes are labeled with either Alexa Fluor 488 or 610 in enamel, orange-enamel (1:50 dilution in clear enamel), or nanodiamonds. For confocal imaging, Alexa 488-enamel pipette was excited at 488nm, while Alexa 610-enamel, orange-enamel, and nanodiamond pipettes were excited at 638nm. For 2-photon imaging, all pipettes were imaged using 980nm excitation. Emission spectra for all excitations were collected in the green (523-593nm confocal; 500-528nm 2-photon) and red (695-765nm confocal, 555-694nm 2-photon) channels. Scale bar = 50 μm.

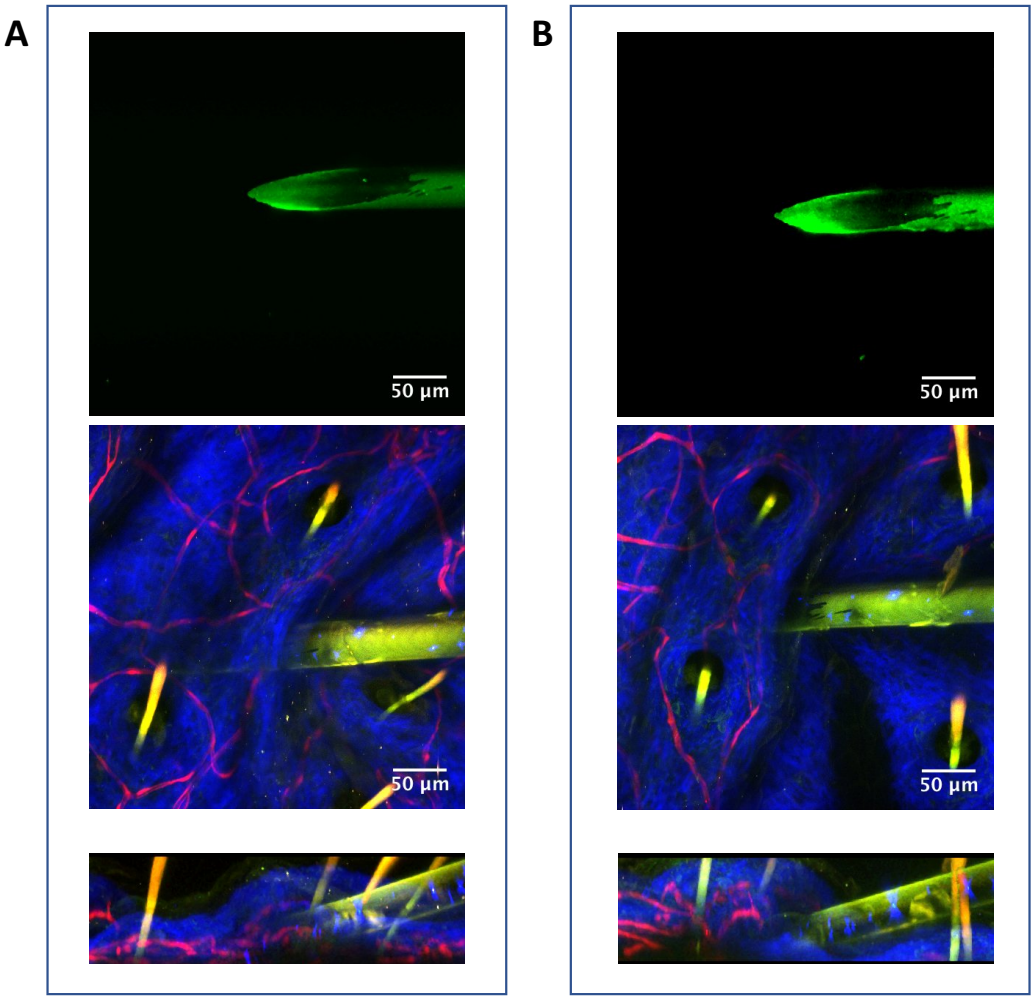

Figure 3.4: Durability of Fluorescent Labeling. A) 2-photon image of Alexa 514-enamel coated pipette before injections into skin (top) and during 1st injection into skin (XY and XZ planes, middle and bottom panels, respectively). B) 2-photon image of same pipette after 9 injections into skin (top) and during the 10^{th} injection into skin (XY and XZ planes, middle and bottom panels, respectively).

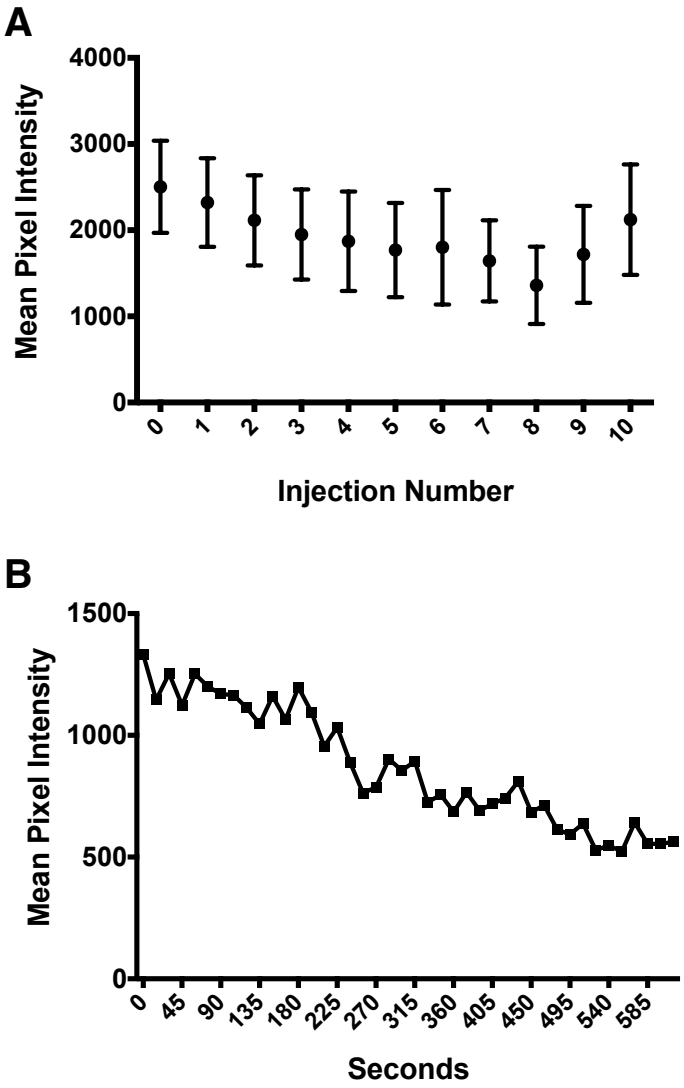

Figure 3.5: Quantification of Fluorescence Durability and Bleaching. A) An Alexa 532-enamel coated pipette was injected into the dermis of a mouse ear 10 times. Before any injections (injection 0) and following every injection, the pipette was imaged using 2-photon excitation as described in the methods. An ROI was created, over the same area of the pipette, on a maximum projection and mean +/- std fluorescence intensity was quantified in ImageJ. B) Mean pixel intensity of three small linear areas along the length of an Alexa-488-enamel coated pipette throughout a 10 minute time series of 2-photon excitation. Distance between data points (squares) is 14.987 seconds. Quantification was performed in ImageJ.

the re-use of a given pipet for many studies.

3.3 Mice and Parasites

Fms-like tyrosine kinase-dsRed (Flt:dsRed) mice from Jackson Labs (strain 400513), which have previously been shown to have fluorescently labeled blood vessels, were used for these studies [8]. During experiments mice were kept under isoflurane anesthesia using the Narishinge SGM-4 (Tokyo, Japan) head holder system on top of a 37°C water heated surgical bed (E-Z Anesthesia, EZ-211: Palmer, PA, USA) and monitored throughout the course of the experiment. Studies were conducted following animal research protocol NHLBI H-0299.

Transgenic parasites expressing green fluorescent protein (GFP) under the *hsp70* promoter [9] were used for intravital imaging. The sporozoite stage of the parasite was generated in *Anopheles* mosquitoes as previously described [10]. Prior to imaging, mosquito salivary glands were dissected in Lebowitz media (L-15, Sigma L4386), homogenized to release sporozoites and then subject to two 100 x g spins at 4°C to remove mosquito debris. The sporozoite suspension was then loaded into the pipette by negative pressure utilizing a hand pump (World Precision Instruments, UltraMicroPump III, UMP3: Sarasota, FL, USA).

3.4 Innoculation of Sporozoites

We monitored the initial inoculation of fluorescently labeled sporozoites using a 2-photon microscope. Injections were performed under the objective (25x 1.1 NA water immersion) of the 2-photon microscope (Leica DM 6 CFS: Wetzlar, Germany), using a customized stage with an attached custom designed micromanipulator and commercial mouse head holder/anesthesia system (Narishinge, SGM-4: Tokyo, Japan). A dissecting microscope (Leica M80: Wetzlar, Germany) on a swinging arm was used to guide the micro-pipette to the focal column of the microscope as well as guide the initial stages of the insertion (Figure 3.6A). Illumination of the stage for the dissecting scope and initial positioning was provided by a flexible light source (Heine HL 1200: Herrsching, Germany). The mouse ear was fixed to the head holder by use of adhesive putty on top of the ear pins (Figure 3.6B). Beveled pipettes preloaded with sporozoite suspension were mounted on the micromanipulator such that the needle was bevel up at a 20° angle with the dermis (Figure 3.6C). After dissecting scope guided penetration of the dermis by the beveled pipette (Figure 3.6D), the stage was brought up to the 2-photon objective. The transverse positioning of the pipet was adjusted initially by bright field through the oculars of the 2-photon using the flexible light source. Once observed to be in the proper location, 2-photon microscopy was utilized with collagen (via second harmonic generation:470-488nm) and blood vessels (fluorescence: 555-694 nm) as a guide for tissue depth, and the position of the pipette was finalized (Figures 3.4). This hybrid injection method, using the dissecting scope to guide the initial gross localization of the pipet, overcame the limitations of

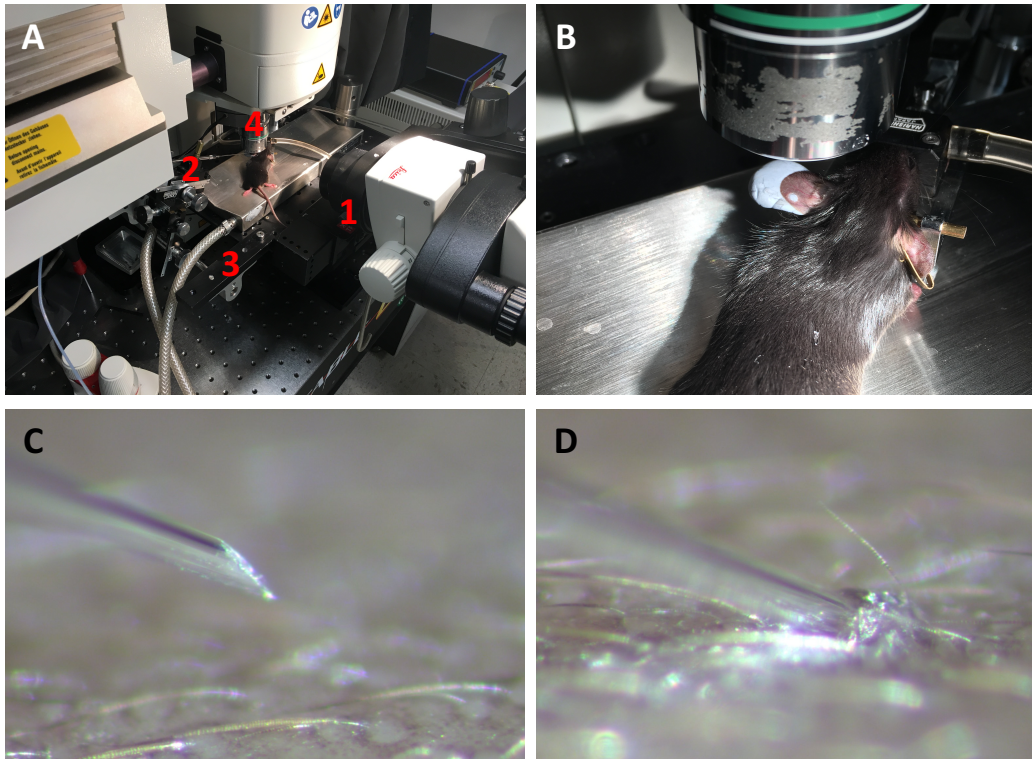

Figure 3.6: Injection System. A) Dissecting scope injection system with: 1 = dissecting scope, 2 = pipette, 3 = 2-photon stage, and 4 = 2-photon objective. B) Ear mounted for imaging using putty on ear pins of the mouse restrainer. C) Observation of pipette through the dissecting scope just prior to penetration. D) Observation of pipette through the dissecting scope after insertion into the skin.

FOV in high resolution fluorescence microscopy by assuring the alignment of the pipets with focal plane of the high-resolution objective. Sporozoites were then injected utilizing the same hand-pump used to load the pipette (Figure 3.7) and monitored by their genetically inserted GFP (fluorescence:500-528 nm). When injections were done with too much force or volume, disruption of the collagen structure was observed, with large holes in the collagen network (Figure 3.8), further validating the usefulness of our micropipette inoculation technique.

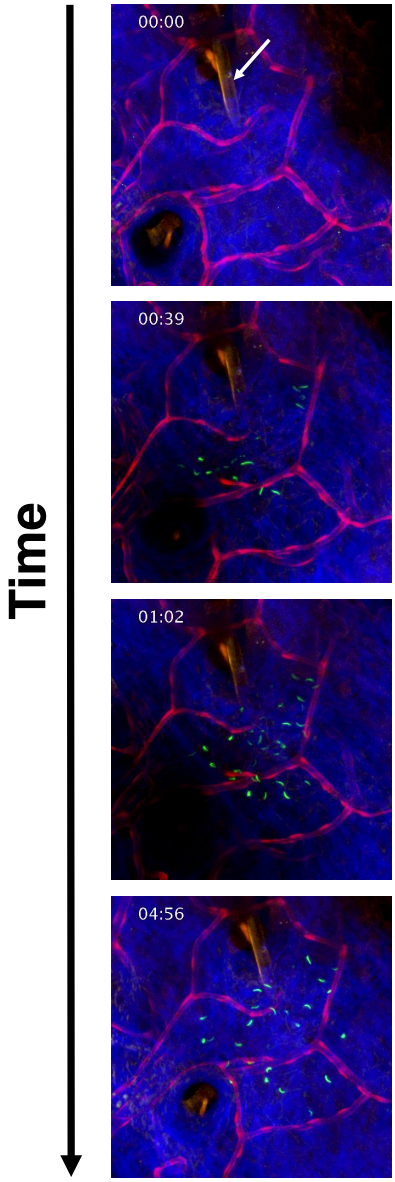

Figure 3.7: Sporozoite Inoculation into Dermis. 2-photon time series of injection into skin. The time series begins with pipette (coated in 1:50 orange enamel, indicated with white arrow) in the dermis before injection. Observation of sporozoite inoculation into dermis with just a few sporozoites trickling into the tissue at 39 seconds followed by bulk injection of sporozoites. XY maximum projection shown. Red channel= vasculature and pipette; blue channel = collagen; green channel = parasites and pipette. Timestamp in upper left corner.

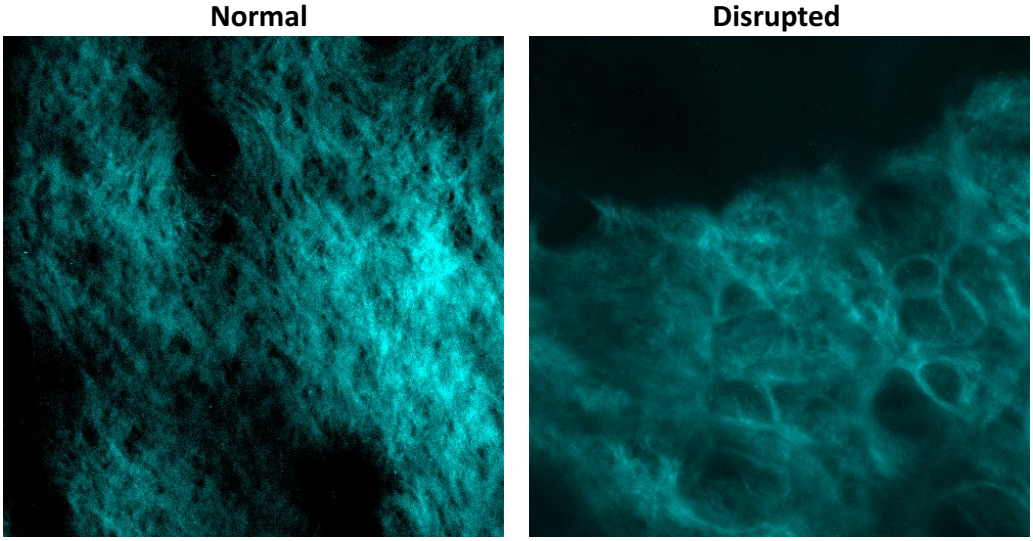

Figure 3.8: Disruption of Collagen Structure with High Force Injections. Standard deviation projections of collagen in untreated dermal tissue (labeled as "Normal") and at a site where an injection done with too much force (labeled as "Disrupted"). Large holes in the collagen structure can be observed when the collagen is disrupted.

As seen in Figures 3.4 and 3.7, the micro-pipet tip was placed in the collagen layer of the skin, which was used as a marker for the dermis, the site of mosquito inoculation of sporozoites. This was accomplished using the outline of the pipet which was readily identified with its fluorescent coating, with dye dilutions optimized to not overwhelm the other chromophores. Naturally, this dilution will depend on a given application. An example of a time course of inoculation of sporozoites is shown in Figure 3.7.

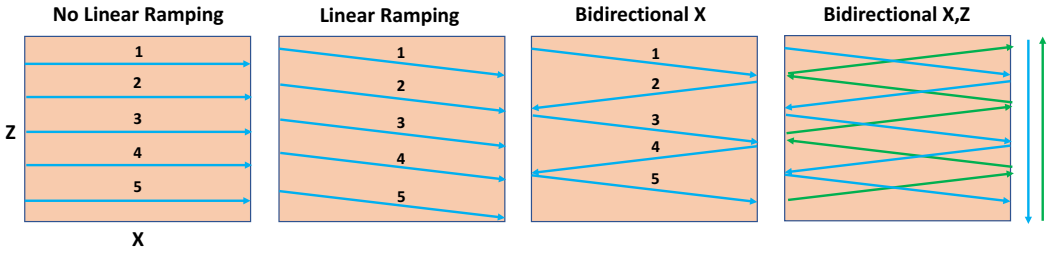

Figure 3.9: Scanning Through a Z-stack with Optimized Acquisition Parameters. Cartoon representation of scanning parameters. Orange box represents X,Z plane of tissue being sampled. Numbered arrows across the box indicates X,Y plane slices through the tissue. Numbers indicate slice number and arrow direction dictates scanning direction. Blue lines indicate moving down through Z, while green lines indicate moving up through Z. Each box is labeled with the acquisition optimization parameter influencing the scanning. Using bidirectional X,Z scanning with linear ramping means that up and down scans of the Z-stack sample different sections of the tissue, particularly at the edges of the X,Z plane.

3.5 Acquisition

Due to the speed of motile sporozoites, 3D spacial information about sporozoite motility in the skin has been limited. We were able to optimize acquisition parameters on this customized Leica DM6 2-photon microscope, such that 80 μm of tissue could be sampled for sporozoite imaging. We utilized a piezo objective scanner to perform linear ramping, such that the objective continuously moved through the specimen in the Z plane, as opposed to taking discrete steps (Figure 3.9), and resonant scanning, such that the laser scanning of the X/Y plane was optimized. On our scope, resonant scanning was at 8 Hz, allowing for approximately 30 frames per second on a 512 x 512 pixel image with bidirectional X scanning (Figure 3.9). To acquire stacks as quickly as possible, bidirectional Z scanning was also utilized (Figure 3.9).

Using these conditions, we tested two acquisition parameters to try and

optimize imaging for analysis: 1) optimized t-resolution and 2) optimized z-resolution. To optimize t-resolution we would need to capture 80 μm of tissue in approximately 1 second in order to ideally capture sporozoite movement. Our system can do this with roughly 30 slices per stack, equating to roughly 2.67 μm step sizes. This results in under sampling of the Z-plane, meaning not all of the tissue space in the Z-plane is represented, and thus, parasites or parasite interactions, could be missed. However, we theorized this would be unlikely as sporozoites are roughly 10-12 μm long and 1 μm wide, so unless they were situated parallel to the imaging plane, they should still be captured as they are longer than the step size. Nonetheless, we also imaged with an optimized z-resolution (0.5 μm step size) with 161 slices per 80 μm stack which took approximately 5.8 seconds per stack. At this time resolution, a sporozoite could potentially travel between 12-36 μm (1-3 body lengths), which could make tracking of sporozoites difficult, particularly at sites with lots of parasites. Given the potential pit-falls of each methodology, these data sets will be compared once we work out the analysis.

3.6 Analysis

Imaris was found to be the best analysis software for our purposes as it handled large data file sizes (20-36 GB) and was able to track moving sporozoites, surface render skin tissue, and quantify interactions between objects in different channels.

Automatic tracking of sporozoites *in vivo* was optimized in Imaris utilizing the ”Spots” function. Initial attempts were performed using the ”Surface”

Parameter	Setting
Enable Region Growing	false
Enable Tracking	true
Estimated Diameter	6.93 µm
Background Subtraction	true
Quality	Above automatic threshold
Tracking Algorithm	Brownian motion
Max Distance	40 µm
Max Gap Size	1

Table 3.1: Imaris Spots Function and Automated Tracking Parameters. Parameters found to be best for automated detection and tracking of sporozoites in Imaris.

function, but clustered sporozoites were frequently seen as a single object, making tracking more difficult. The ”Spots” function handled this discrepancy better and it was easier to manually fix tracks. The ”Spots” function parameters for spot detection and tracking are in Table 3.1. The ”Brownian motion” algorithm was better at tracking sporozoites than the ”Autoregressive motion” algorithm, due to the frequent directional changes of sporozoites. The ”Autoregressive motion” algorithm is better suited for objects following a linear path, as it uses the directionality of the tracked object to predict where the object will be next. The maximum distance permitted between frames for a sporozoite to move and still be recognized as the same sporozoite was set to 40 μm, which is substantially larger than the distance a sporozoite would be predicted to travel between frames, however, it permitted greater flexibility for tracking parasites which had changed directions between frames.

After automated tracking, manual alteration of tracks was still required

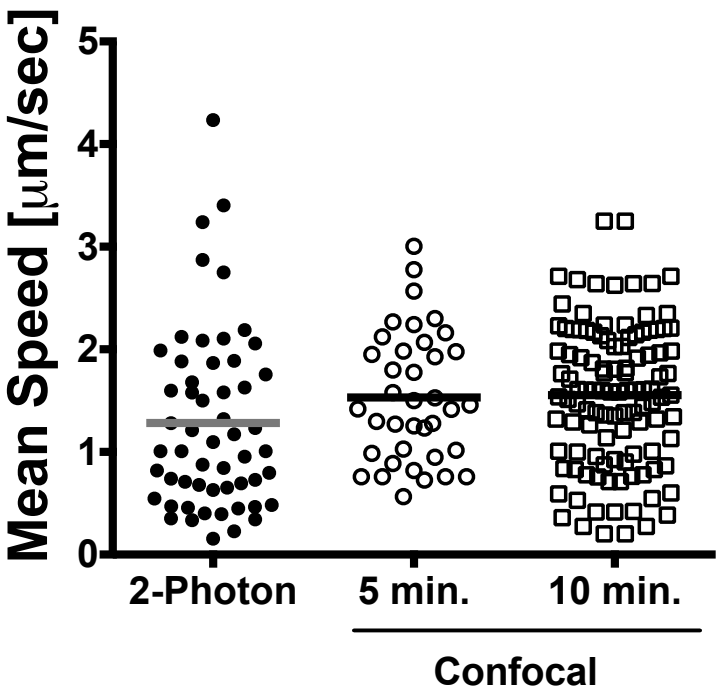

Figure 3.10: Mean Speed of Tracked Sporozoites. Mean speed of individual sporozoites from three 15 minute movies acquired with optimized Z-scan parameters and are labeled as ”2-photon” in the graph. n=55. Mean speeds observed in 2-photon acquisition are comparable to those previously recorded from 4 minute movies using confocal microscopy 5 or 10 minutes after injection of sporozoites. Confocal speed data taken from Hopp *et al.* [3].

as occasionally autoflourescent artifacts (especially hairs) were tracked or sporozoites were tracked incorrectly. At inoculation sites with a high density of sporozoites, it may be faster to manually track sporozoites due to the time required in manual alteration after automated tracking. Preliminary data shows that the average mean sporozoite speed was $\sim$1.3 μm\second (Figure 3.10), which is comparable to previously reported sporozoite speeds *in vivo* (Figure 3.10) [3].

To assess the interactions of sporozoites with blood vessels, I have conducted a preliminary analysis using the ”Kiss and Run” Xtension in Imaris

which connects to MatLab. This Xtension allows for the quantitative description of interactions between objects in different fluorescent channels. In our case, we are interested in the interactions of sporozoites in the green channel and blood vessels in the red channel. To utilize the Xtension, the blood vessels were modeled using the ”Surface” function. Then, using the blood vessel surfaces, and previously generated ”Spots” used to track sporozoites, the ”Kiss and Run” program was run. The program outputs the following data for describing sporozoite-blood vessel interactions: distance between sporozoites and a vessel, longest contact event, mean amount of contact time, number of contact events, number of prolonged contact events, and total time in contact. Pilot tests of this XTension on a small data set (shortened movie) worked nicely, but once applied to full length movies, Imaris struggled to complete the program, frequently freezing. The failure occured during the transfer of data between Imaris and MatLab. Further troubleshooting of these computational issues are required in order to troubleshoot this analysis method and extrapolate the desired data.

Confident quantification of sporozoite blood vessel invasion events were not possible due to the line scanning acquisition which prevented the observation of sporozoites inside of blood vessels. The topology of the skin was also problematic as blood vessels lay underneath the collagen I layer of the dermis (Figure 3.11) and are thus at the bottom of acquired z-stacks. This made determination of a sporozoite invasion event, versus leaving the FOV, impossible. Alternative imaging strategies would need to be utilized to observe sporozoite invasion of blood vessels.

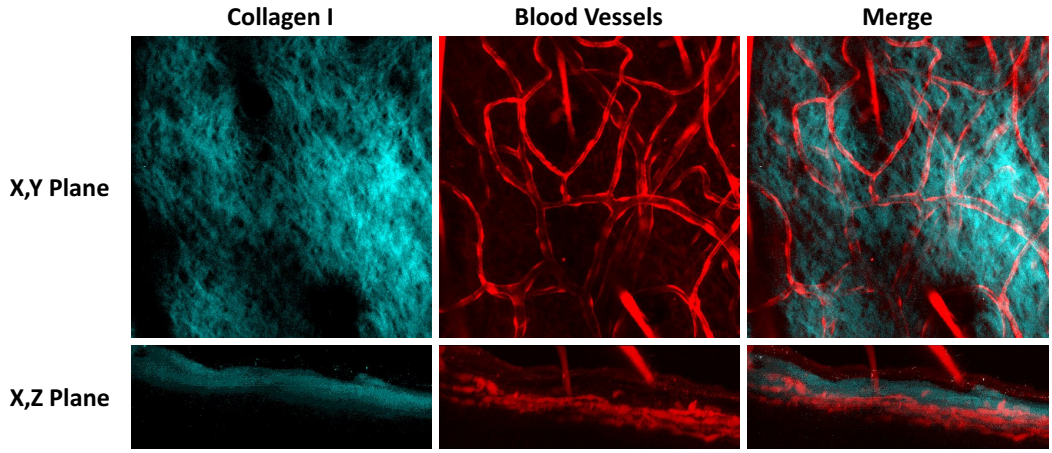

Figure 3.11: Topography of the Dermal Tissue. Projections of 2-photon image of dermal tissue in the ear of a mouse. Second harmonic generation (SHG) signal shows Collagen I in blue. dsRed labeled blood vessels are in red. X,Y (top) and X,Z (bottom) planes are shown.

We are also interested in using these data to describe sporozoite interactions with collagen in the skin, however the analysis of these interactions has proved difficult. For one, I have not been able to get a good rendering of the collagen using the "Surface" function in Imaris. This means that the use of the "Kiss and Run" Xtension that I plan to use on the blood vessels will not be usable for the characterization of sporozoite interactions with collagen. Qualitatively, I observed that sporozoites seem to track collagen I fibers and that in parts of the skin without collagen I, sporozoites seem to move in a more constrained fashion. I tried to quantitatively describe this phenomena by breaking the sporozoite tracks up into segments of linear and constricted periods of movement and then extrapolate the mean intensity of the collagen channel for each of these tracks, a statistic readily available through the tracks function of Imaris. This approach has proved to be somewhat subjective and

the intensity measurements of the collagen channel are low, and thus there is not a large enough dynamic range in the data to extrapolate differences. It is possible that image processing steps are required for this analysis to be informative.

3.7 Future Directions

We have developed a method for generating fluorescently labeled micropipettes for mimicking a mosquito bite into the dermis and significantly improved procedures for intravital imaging of these parasites in the skin (Figures 3.1 & 3.7). While our interests were focused on the malaria parasite, many other infectious disease studies will benefit from utilization of the described pipette system. Other pathogens transmitted by insect vectors such as *Leishmania* (parasite responsible for leishmaniasis), *Borrelia* (bacteria responsible for Lyme Disease), and dengue (virus responsible for dengue fever) can now be studied *in vivo* at the instant of inoculation into the skin. Studying vector born diseases in this fashion will expand our understanding of transmission and dissemination of these pathogens, enabling the design of new vaccines and control mechanisms. Non-vector born pathogens will also benefit from this approach due to enhanced control of inoculum. Additionally, this technique will prove valuable for the neuroscience and cancer biology communities. Using the fluorescent pipettes created herein, one can target a drug, compound, dye, or cell suspension to an area of interest while under direct microscopic observation, permitting instantaneous observation of behavior or response to inoculated elements. The capacity to do so provides an opening to answer yet

unexplored temporal and spacial questions in these fields.

In addition to our micro-pipette inoculation method, 4D analysis of sporozoite motility is accessible with the rapid acquisition speeds and parameters utilized on our system, but further troubleshooting of data analysis is required in order to process and analyze the large data sets acquired. From these data, we plan to describe parasite interactions with blood vessels and the extracellular collagen I network as well as a describe the motility of parasites immediately after inoculation into the skin. To supplement these data, *in vitro* assays comparing sporozoite motility in collagen I gels, in comparison to matrigel, would be of interest. Previous 3D *in vitro* motility assays with sporozoites have been conducted in matrigel [9, 11], a gelatinous protein mixture which is largely composed of laminin, collagen IV, and entactin and is used to mimic the basement membrane [12]. In these experiments, sporozoites corkscrew through the matrigel [9, 11], which may replicate their interactions with basement membrane, but not how they move in the skin. It would be interesting to see if in a collagen I gel, sporozoites move in a more linear fashion, tracking collagen I fibers, as has been observed with cancer cells [13]. For these studies, several collagen polymerization and density conditions should be tested to try and best mimic the collagen I structure of the skin. If successful, these assays could be used to probe sporozoite interactions and response to dermal tissue components. The rapid acquisition described above will also be particularly useful to study parasite interactions with blood vessels, a phenomena we know essentially nothing about. In conjugation with

specific receptor labeling, mutant parasites, and/or transgenic mice, dissecting sporozoite interactions with blood vessels is now possible and could lead to the development of new strategies to prevent malaria infection.

References

1. Yamauchi, L. M., Coppi, A., Snounou, G. & Sinnis, P. Plasmodium sporozoites trickle out of the injection site. *Cellular Microbiology* **9,** 1215–1222 (2007).
2. Amino, R. *et al.* Quantitative imaging of Plasmodium transmission from mosquito to mammal. *Nature Medicine* **12,** 220–224 (2006).
3. Hopp, C. S. *et al.* Longitudinal analysis of Plasmodium sporozoite motility in the dermis reveals component of blood vessel recognition. *eLife* **4,** e07789 (2015).
4. Andrasfalvy, B. K. *et al.* Quantum dot-based multiphoton fluorescent pipettes for targeted neuronal electrophysiology. *Nature Methods* **11,** 1237–1241 (2014).
5. Yu, S. J., Kang, M. W., Chang, H. C., Chen, K. M. & Yu, Y. C. Bright fluorescent nanodiamonds: no photobleaching and low cytotoxicity. *Journal of American Chemical Society* **127,** 17604–17605 (2005).
6. Goss, B. Bonding glass and other substrates with UV curing adhesives. *International Journal of Adhesion and Adhesives* **22,** 405–408 (2002).
7. Izumi, H., Suzuki, M., Aoyagi, S. & Kanzaki, T. Realistic imitation of mosquito's proboscis: electrochemically etched sharp and jagged needles and their cooperative inserting motion. *Sensors and Actuators A: Physical* **165,** 115–123 (2011).
8. Matsumoto, K. *et al.* Study of normal and pathological blood vessel morphogenesis in Flt1-tdsRed BAC Tg mice. *Genesis* **50,** 561–571 (2012).
9. Amino, R. *et al.* Host cell traversal is important for progression of the malaria parasite through the dermis to the liver. *Cell Host & Microbe* **3,** 88–96 (2008).
10. Vanderberg, J. P. & Gwadz, R. W. in *Pathology, Vector Studies, and Culture* 153–234 (Elsevier, 1980).

11. Akaki, M. & Dvorak, J. A. A chemotactic response facilitates mosquito salivary gland infection by malaria sporozoites. *Journal of Experimental Biology* **208,** 3211–3218 (2005).

12. Hughes, C. S., Postovit, L. M. & Lajoie, G. A. Matrigel: a complex protein mixture required for optimal growth of cell culture. *Proteomics* **10,** 1886–1890 (2010).

13. Wang, W. *et al.* Single cell behavior in metastatic primary mammary tumors correlated with gene expression patterns revealed by molecular profiling. *Cancer Research* **62,** 6278–6288 (2002).

Chapter 4

Probing CSP Macromolecular Structure

One of the important unknowns of malaria sporozoite biology is the how CSP is organized on the surface of the sporozoite. We attempted to probe CSP organization using two methods: blue native gel and electron microscopy.

4.1 CSP Blue Native Gel and Calcium Binding

The initial goals of analyzing CSP by native gel were a) to determine if CSP formed a multimer and b) to determine if CSP bound to calcium. Although it has been well estabilished that CSP forms a dense protein coat on the surface of the sporozoite, little is known about the interactions of CSP with surface molecules. It has been hypothesized that CSP could form multimers to create a meshwork on the surface, however, there has been no evidence of any CSP interactions to date. Evidence for CSP-calcium binding comes from nuclear magnetic resonance (NMR) or circular dichroism (CD) on CSP repeat peptides which provided evidence for calcium binding to the negatively charged

residues of the repeats inducing a β-turn confirmation [1, 2]. We hypothesized that the binding of calcium to the repeats could induce CSP repeat conformational changes during sporozoite migration leading to the changes in CSP terminal end exposures [3]. Interestingly, the calcium concentration of the various tissues and compartments in which the sporozoite travels varies. The calcium concentration in the blood is $\sim$2.25 mM, approximately 10^5 fold higher than intracellular concentrations (100 nM) [4]. It is possible that calcium binding to the repeat region of CSP changes as sporozoites travel from the blood into the hepatic sinusoid where they traverse sinusoidal barrier cells prior to productive hepatocyte entry.

4.1.1 Methods

4.1.1.1 Blue Native Gel

To optimize the blue native gel protocol and observe if CSP would run as a multimer, *Plasmodium falciparum* sporozoite lysates were used. Sporozoites were isolated and lysed using sonication in PBS with protease inhibitors (Roche #1836153). Lysates were centrifuged at 13,000 g for 20 minutes at 4°C and supernatant and pellet were separately analyzed. 4x native sample buffer (200 mM BisTris, 64.2 mM HCl, 4.3 M glycerol, 200 mM NaCl, and 60 mM Ponceau S) or 6x denaturing sample buffer (0.125 M Tris-HCl pH 6.8, 20% glycerol, 4% SDS, and 0.002% bromophenol blue) was added to a final concentration of 2x. For native protein sample conditions, 0.5% Coomassie G-250 (Sigma # 20279) was added before loading sample to the gel, to allow protein migration in an electric field. Samples were run on a handcast 10%

native gel at 150 V with Dark Cathode Buffer (50 mM BisTris, 50 mM Tricine, 1x Cathode Additive (Life Technologies #BN2002)) until the dye front reached a third of the way through the gel at which point the buffer was replaced with Light Cathode Buffer (50 mM BisTris, 50 mM Tricine, 0.1x Cathode Additive), with the same anode buffer used throughout the run (50 mM BisTris, 50 mM Tricine). After transfer, membranes were probed with monoclonal antibody 2A10, which targets the repeats of *P. falciparum* CSP.

4.1.1.2 Calcium Binding Blot

For this CSP-calcium binding analysis, CSP was immunoprecipitated from *P. berghei* sporozoites as previously described in Coppi *et al.* [5]. Immunoprecipitated CSP was eluted from beads with either denaturing (100 mM glycine pH 1.5 and 1% SDS) or native (100 mM glycine pH 2.3) conditions followed by 10 μl of native or denaturing sample buffer. For native protein samples, 0.5% Coomassie G-250 was added before loading sample to the gel. Additional controls included whole sporozoite lysate in 2x boiling denaturing sample buffer and 10 μg of Calmodulin (Sigma #C4874), a known calcium binding protein. Samples were run on a pre-cast 4-12% native gel (Life Technologies #BN1002) in duplicate so that samples could be probed by western blot and tested for calcium binding. For western blots, membranes were probed with 3D11 and the calcium binding assay was adapted from Tatsumi *et al.* [6]. Briefly, membranes were washed in deionized water and incubated with 1mM $CaCl_2$ for 1 hour at room temperature and then washed with 20% ethanol followed by deionized water. The membrane was then incubated with 1 mM quin-2, a fluorescent quinoline Ca indicator which excites under UV light,

for 1 hour at room temperature followed by deionized water washes. The membranes were allowed to dry and then imaged on a Gel Red imager with UV light.

4.1.2 Results and Discussion

4.1.2.1 CSP Migrates as a Monomer by Blue Native Gel

To solubilize membrane proteins for analysis by blue native gels, mild detergents that adequately solubilize but do not result in micelle formation must be found empirically [7, 8]. We found that digitonin alters the migration of CSP on a native gel, causing it to migrate at a higher molecular weight (Figure 4.1). Digitonin is known to cause anomalous migration of proteins due to the formation of micelles [9, 10] and this artifact could lead to misinterpretation of native gel results. In our studies, upon addition of digitonin, native CSP appears to migrate at a higher molecular weight than that of denatured CSP, suggesting that it could exist as a dimer on the sporozoite surface (Figure 4.1). However, addition of dodecyl-β-D-maltoside (12M), an alternative detergent with digitonin treated samples, led to a dose dependent decrease in native CSP migration and samples with 12M only resulted in CSP migration at the same molecular weight as denatured CSP (Figure 4.1). This suggests that CSP does not exist as a multimer on the sporozoite surface, or if so, has weak intermolecular interactions. Without any detergent in the CSP sample preparation, no protein was observed (Figure 4.1).

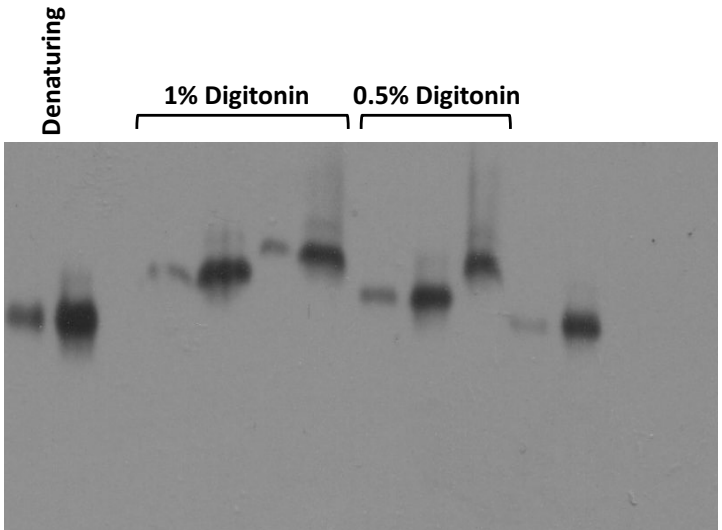

S	P	-	S	P	S	P	S	P	P	S	P	S	P	Pellet (P) or Supernatant (S)
-	-	-	+	+	-	-	+	+	-	+	+	-	-	1% 12M

Figure 4.1: ***Plasmodium falciparum*** **CSP Migrates as a Monomer on Blue Native Gel.** Western blot from 10% native gel run with denatured samples as well as various native sample conditions with different detergent conditions. Table below western blot indicates whether sample was from supernatant (S) or pellet (P) of sonicated fractions as well as whether 1% 12M was added. Above the blot, the reducing condition lanes are indicated as well as percentage of digitonin added. On right side of gel molecular weight markers from native gel ladder (Life Technologies #LC0725).

4.1.2.2 CSP-Calcium Blot

To assess calcium binding to CSP repeats, we utilized the native gel protocol established above, in order to maintain any structural features important for calcium binding. We also immunoprecipitated (IP) CSP to limit signal from other calcium binding proteins present in either the mosquito tissue or sporozoites. In a preliminary gel, we observe a faint band in the lane with CSP IP-ed under native conditions, but no clear signal in denatured sporozoite lysate or IP-ed CSP under denaturing conditions. We also saw signal in our positive control, calmodulin, which has a known structural calcium binding motif (EF hand). These data suggest that CSP binds to calcium in a conformationally dependent manner. However, the western blot component of this experiment was unsuccessful, so we cannot be certain the band observed is CSP.

Future experiments are needed to validate these results and optimize signal. Additionally, this assay should be done with the ΔDtoN parasite line, which has had the negatively charged residues (aspartic acids) mutated to neutral amino acids (asparagines). We would thus hypothesize that if calcium was binding to the repeats, that the negatively charged residues of the repeats are important for this coordination and without them, calcium would not bind. Thus, we would hypothesize that the ΔDtoN mutant CSP would not bind calcium in this assay. Additionally, it would be interesting to perform this assay with the ΔScr mutant CSP to explore the importance of repeat conformation for calcium binding.

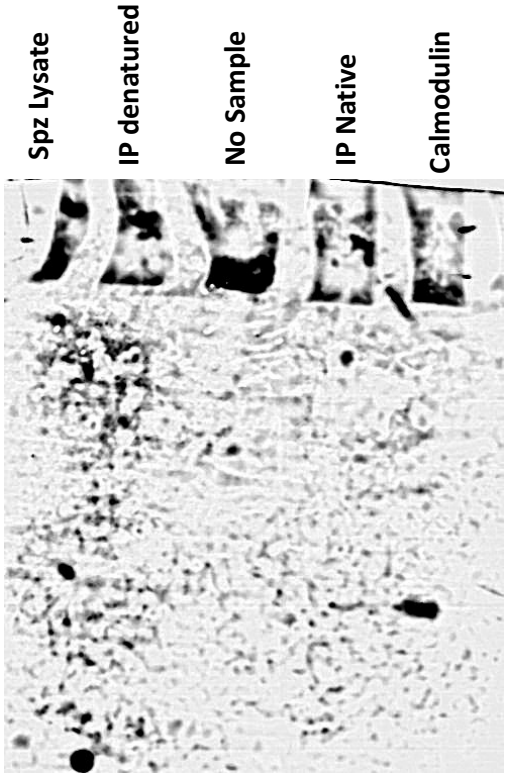

Figure 4.2: ***Plasmodium berghei*** **CSP-Calcium Blot.** Calcium chloride blot with Quin-2 demonstrating calcium binding to CSP. Signal is only seen with positive control, calmodulin, and IP-ed CSP under native conditions.

4.2 Negative Stain Transmission Electron Microscopy of Lysed Sporozoites

Another approach we took to look at CSP organization on the surface of the sporozoite, was electron microscopy (EM). These studies were conducted in collaboration with Dr. Egbert Hoiczyk, an expert in using electron microscopy to study surface protein structures. Our hypothesis was that CSP might form macromolecular complexes on the surface of the sporozoite visible by EM.

4.2.1 Methods

P. falciparum sporozoites were isolated from the salivary glands of *An. stephensi* mosquitoes Day 14-16 pbm. Sporozoites were purified twice on a 17% Accudenz (Accurate Chemical and Scientific Corporation #AN7050) density gradient. After purification, sporozoites were spun onto copper electron microscopy grids (Electron Microscopy Sciences #CF400-CU) and fixed/negative stained with 2% uranyl acetate. Initial experiments demonstrated that the sporozoites are very rigid and do no flatten on the EM grids, resulting in build up of negative stain along the edges of the sporozoites and preventing observation of surface architecture (Figure 4.3 A). Thus, a series of protocols for lysis and/or flattening of sporozoites was tested. These included freeze-thaw, votexing with beads, trifluralin (microtubule inhibitor, Sigma #45913), and ultrasonication. We found that lysis through glass beads or ultrasonication worked best and thus proceeded with this method.

4.2.2 Results and Discussion

Protein organization on the sporozoite surface was not visible (Figure 4.3 B & C), but microtubules and actin filaments present under the plasma membrane were visible (Figure 4.4). Microtubules measured approximately 24 nm in width (Figure 4.4D & E), as was expected, and structures identified as actin filaments measured less than 10 nm in width (Figure 4.4C). We were also able to nicely visualize the apical ring of the sporozoite, measuring approximately 200 nm (Figure 4.4F). However, we were unable to distinguish cytoskeletal components from the architecture of plasma membrane.

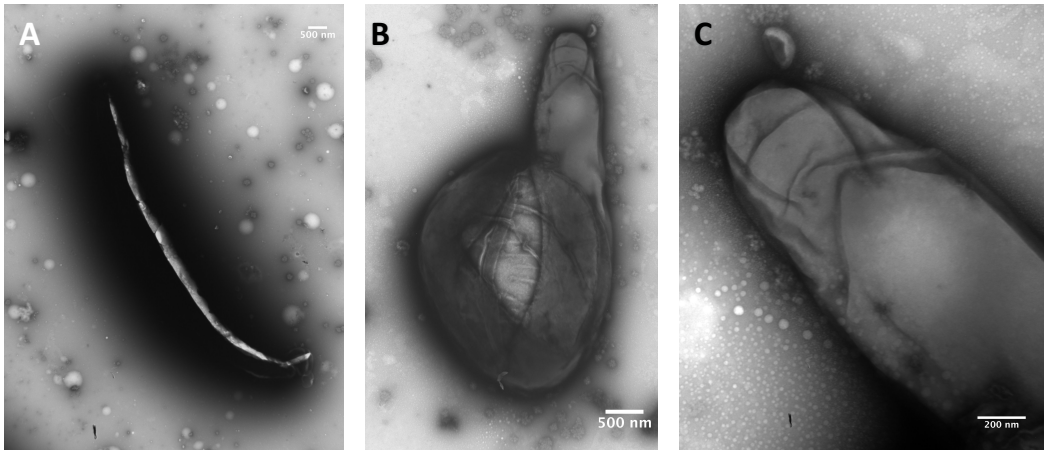

Figure 4.3: *Plasmodium falciparum* Negative Stain EM Requires Sporozoite Lysis. A) Negative stain build up on edges of unlysed sporozoite preventing observation of surface architecture B) Example of sporozoite after lysis without cytoskeletal components obstructing surface architecture C) Higher magnification of sporozoite in B).

There is currently little data on the structure of actin filaments in sporozoites, but they are predicted to be short [11]. Our images provide support for this hypothesis with examples of what are likley actin filaments, measuring 100-150 nm in length and 4-6 nm in diameter, outside of ruptured sporozoites, where microtubules could also be visualized (Figure 4.4). Interestingly, it also appears as though these filaments run longitudinally along the length of the sporozoite, providing new insight into actin filament organization in sporozoites (Figure 4.4 A & B).

Finally, we observed what appears to be a secreted body from the apical end of the sporozoite, with the apical end determined by the relationship to the nucleus (Figure 4.5). Previous studies have also seen apical secretions by EM that appeared to be membrane bound [12], however, it could be that the observation of these protrusions is an artifact of sample preparation.

Overall, while these studies did not provide insight into CSP macromolecular structure, novel observation of cytoskeletal components of the sporozoite was achieved. In particular, the potential observation of actin filaments is interesting and should be followed up for confirmation as the observed filaments could actually be intermediate filaments. If the observed filaments are indeed actin, this approach could allow for new insights on sporozoite actin.

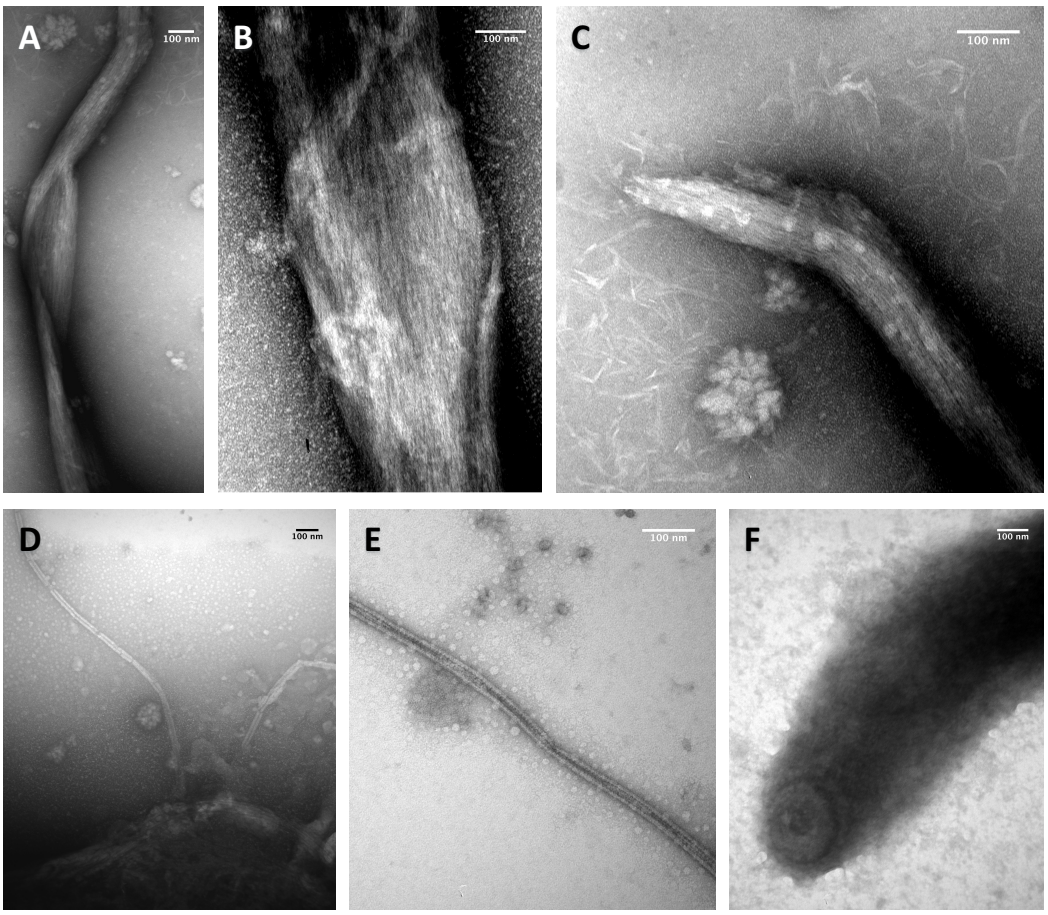

Figure 4.4: *Plasmodium falciparum* Cytoskeletal Structures. A) Flattened sporozoite with filaments running parallel to the longitudinal axis of the sporozoite. B) Higher magnification of filaments seen in A). C) Fractured sporozoite with released filaments surrounding it. Filaments are also visible in the sporozoite body D) Fractured sporozoite with microtubules released E) Higher magnification of of the microtubules in D). F) Apical pore of sporozoite. Scale bars are 100 nm.

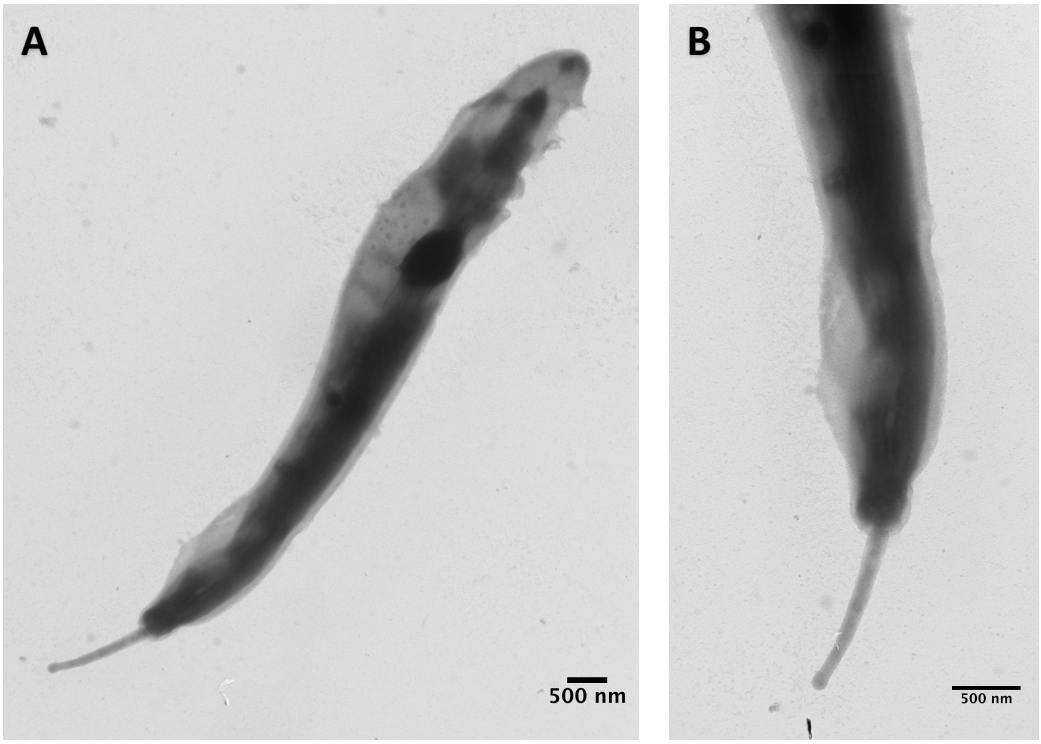

Figure 4.5: *Plasmodium falciparum* Anterior Protrusion. A) Example of full sporozoite with protrusion at the anterior end. Dark round nucleus marks the posterior end of the sporozoite. B) Higher magnification on anterior end protrusion seen in A)

References

1. Verdini, A. S., Chiappinelli, L. & Zanobi, A. Toward the eludicdation of the mechanism of attachment and entry of malaria sporozoites into cells: Synthetic polypeptides from circumsporozoite protein of Plasmodium falciparum bind Ca2+ and interact with model phospholipid membranes. *Biopolymers* **31,** 587–594 (1991).
2. Topchiy, E. & Lehmann, T. Chelation of Ca2+ ions by a peptide from the repeat region of the Plasmodium falciparum circumsporozoite protein. *Proteins* **59,** 828–839 (2014).
3. Coppi, A. *et al.* The malaria circumsporozoite protein has two functional domains, each with distinct roles as sporozoites journey from mosquito to mammalian host. *Journal of Experimental Medicine* **208,** 341–356 (2011).
4. Bronner, F. Extracellular and intracellular regulation of calcium homeostasis. *Science World Journal* **1,** 919–925 (2001).
5. Coppi, A., Pinzon-Ortiz, C., Hutter, C. & Sinnis, P. The Plasmodium circumsporozoite protein is proteolytically processed during cell invasion. *Journal of Experimental Medicine* **201,** 27–33 (2005).
6. Tatsumi, R., Shimada, K. & Hattori, A. Fluorescence detection of calcium-binding proteins with quinoline Ca-indicator quin2. *Analytical Biochemistry* **254,** 126–131 (1997).
7. Eubel, H., Braun, H. & Millar, A. H. Blue-native PAGE in plants: a tool in analysis of protein-protein interactions. *Plant Methods* **1,** 11 (2005).
8. Reisinger, B. & Eichacker, L. A. How to Analyze Protein Complexes by 2D Blue Native SDS-PAGE. *Proteomics* **7,** 6–16 (2007).
9. Crichton, P. G., Harding, M., Ruprecht, J. J., Lee, Y. & Kunji, E. R. S. Lipid, detergent, and coomassie blue G-250 affect the migration of small membrane proteins in blue native gels. *Journal of Biological Chemistry* **288,** 22163–22173 (2013).

10. Rath, A., Glibowicka, M., Nadeau, V. G., Chen, G. & Deber, C. M. Detergent binding explains anomalous SDS-PAGE migration of membrane proteins. *PNAS* **106,** 1760–1765 (2009).

11. Schmitz, S. *et al.* Malaria parasite actin filaments are very short. *Journal of Molecular Biology* **349,** 113–125 (2005).

12. Niz, M. D. *et al.* Progress in imaging methods: insights gained into Plasmodium biology. *Nature Reviews Microbiology* **15,** 37–54 (2017).

Chapter 5

Conclusion and Future Directions

This thesis has generated new hypothesis as to how the CSP repeats function and how sporozoites move.The explosion of microscopy techniques provides a particularly appealing avenue for the observation of sporozoite surface architecture and composition during motility. A first experiment would be to visualize CSP macromolecular structure on the surface of the sporozoite using an immunofluorescence assay with super resolution microscopy. However, the high abundance of CSP on the sporozoite surface, in addition to the large size of antibodies, may prevent observation of CSP organization. Thus, alternative methods for protein labeling should be considered, including click-chemistry [1] or leucine zipper domains [2], which use smaller fluorescent probes. These approaches could allow for the observation of CSP and other surface proteins in fixed cells or live sporozoites during gliding, providing new insights of surface protein dynamics. Förster resonance energy transfer (FRET) may also prove useful to observe surface protein and/or motor complex interactions. This approach could be used to look at inter- or intra-molecular interactions of CSP, or interactions between proteins of the motor complex, to define

molecular interactions during parasite gliding. This would be particularly interesting in conjugation with reflection interference contrast microscopy (RICM) to observe the localization of these interactions with respect to the adhesion sites. If any of these approaches work, they would vastly enhance our understanding of sporozoite biology.

In addition to dissecting the mechanisms underlying sporozoite motility *in vitro*, the relatively recent observations of sporozoite motility *in vivo* should be pursued further. Observations and characterization of sporozoite interactions *in vivo* will continue to drive hypotheses of how sporozoites leave the bite site and initiate an infection, providing new avenues of research and potential vaccine targets. Of particular interest is the interactions between sporozoites and blood vessels, but as blood vessel invasion events are rare events (<2% of sporozoites [3]), determination of what signals guide entry will be difficult.

Plasmodium sporozoites are heavily dependent on their motility machinery for their biological niche - infection of a vertebrate host. However, our current understanding of how sporozoites move is lacking and utilization of advanced microscopy techniques will enable a deeper understanding of the interactions driving sporozoite motility and a better understanding of protein function in motility.

References

1. Best, M. D. Click chemistry and bioorthogonal reactions: unprecedented selectivity in the labeling of biological molecules. *Biochemistry* **48,** 6571–6584 (2009).
2. Hayashi, A., Asanuma, D., Kamiya, M., Urano, Y. & Okabe, S. High affinity receptor labeling based on basic leucine zipper domain peptides conjugated with pH-sensitive fluorescent dye: Visualization of AMPA-type glutamate receptor endocytosis in living neurons. *Neuropharmacology* **100,** 66–75 (2016).
3. Hopp, C. S. *et al.* Longitudinal analysis of Plasmodium sporozoite motility in the dermis reveals component of blood vessel recognition. *eLife* **4,** e07789 (2015).

Amanda Balaban

E-mail: abalaba1@jhu.edu

615 N. Wolfe St.
Baltimore, MD 21205
(301)-466-9196

Education

Lafayette College, B.S. in Biology, Minor in Biotechnology **Easton, PA**
Cumulative GPA**:** 3.53 **Graduated May 2012**
Academic Honors**:** Dean's List (Fall 2009, Fall 2010, Fall 2011, Spring 2012), Willis Roberts Hunt Biology Prize (Spring 2012)

Johns Hopkins Bloomberg School of Public Health, PhD **Baltimore, MD**
Cumulative GPA**:** 3.69 **Graduate May 2018 (Expected)**
Academic Honors**:** Katharine E. Welsh Fellowship in Immunology and Infectious Disease (2013, 2014)

Other Honors: NIH Directors Award (Dr. Francis Collins) for contribution to NIH Library Team (2010)

Specialized Courses:
Wellcome Trust: Malaria Experimental Genetics **March 9-15, 2014**

PhD Thesis Research **Fall 2012-Present**

Johns Hopkins School of Public Health, Molecular Microbiology and Immunology, Baltimore, MD
Formulating a model for the role of the tandem amino acid repeat region of the major surface protein, circumsporozoite protein (CSP), of the malaria sporozoite using a mutagenesis approach in conjunction with other molecular and cellular biology techniques. Mutant parasites exhibited phenotypes within the mosquito and mammalian hosts, likely due to defects in parasite motility. **Technical focus was on**: live cell imaging, immunofluorescence assays, and intravital imaging requiring the mastery of various confocal, 2-photon, and widefield microscopes. ImageJ, Imaris, and NIS-Elements were used for image analysis. Other technical expertise includes: RT-qPCR, flow cytometry, ELISAs, transfections/molecular cloning, protein blotting, antibody development, and mosquito and mouse handling. Expertise was frequently required for new technique/protocol optimization and/or development.

Additional Research Experience

Research Internship, *NIH*, NICHD, Lab of Cellular & Molecular Biophysics, Bethesda, MD **Summers of 2009, 2010, 2011**
Worked with malaria (*Plasmodium falciparum*) investigating parasite egress from various hemoglobinopathies using live cell microscopy (confocal) to analyze egress, morphology, and parasite replication.

Independent Study, *Lafayette College*, Department of Biology, Easton, PA **Spring 2010-2012**
Worked with trematode parasite*, Echinostoma caproni*, in a snail model *(Biomphalaria glabrata*) developing culture conditions that were ideal for rearing neonatal *B. glabrata* and conducted studies on their susceptibility to infection with *E. caproni*.

Independent Study, *Lafayette College,* Department of Chemical and Biomolecular Engineering, Easton, PA **Fall 2011-2012**
Conducted confocal microscopy of cells grown on thermoresponsive polymers to begin phenotypic analysis of focal adhesions and cell morphology.

Future Research Interests

In my post-doc, I will train to think from a mechanics perspective, to think multi-dimensionally and tackle complex problems in cell biology.

- Cell mechanics
- Cell motility
- Microscopy
- Coding for image/data analysis

Publications

1) Glushakova, S., Humphrey, G., Leikina, E., **Balaban, A. E.**, Miller, J., Zimmerberg, J. (2010). New stages in the program of malaria parasite egress imaged in normal and sickle erythrocytes. *Current Biology, 20*(12), 1117-1121.

2) **Balaban, A.,** & Fried, B. (2011). Maintenance of *Biomphalaria glabrata* in artificial spring water, deionized water, and conditioned tap water. *American Malacological Newsletter, 42*(2), 8-9.

3) **Balaban, A.,** Fried, B., & Sherma, J. (2012). Thin-layer chromatographic analysis of neutral lipids in neonatal *Biomphalaria glabrata* snails maintained on a *Nostoc* sp. diet. *American Malacological Society Newsletter, 43*(1), 4-5.

4) **Balaban, A.,** & Fried, B. (2013). Infection of neonatal *Biomphalaria glabrata* with the miracidia of *Echinostoma caproni*. *Journal of Parasitology, 99*(3), 543.

5) Fried, B. & **Balaban, A**. (2013). The heart of *Biomphalaria glabrata* as a site for the localization of *Echinostoma caproni* sporocysts. *American Malacological Society Newsletter, 44*(1), 4-5.

6) **Balaban, A.,** & Fried, B. (2013). Maintenance of *Biomphalaria glabrata* infected with *Schistosoma mansoni* in artificial spring water, deionized water, or conditioned tap water. *Comparative Parasitology, 80*(1),118-119

7) **Balaban, A. E.,** & Fried, B. (2014). Effects of crowding on survival and growth of neonatal *Biomphalaria glabrata* snails maintained on a *Nostoc* sp. Diet. *The Veliger, 51*(4), 252-254.

8) Glushakova, S., **Balaban, A.**, McQueen, P., Coutinho, R., Miller, J. L., Nossal, R., Fairhurst, R. M., & Zimmerberg, J. (2014). Hemoglobinopathic erythrocytes affect the intraerythrocytic multiplication of *Plasmodium falciparum* in vitro. *Journal of Infectious Diseases, 210*(7), 1100-1109.

9) **Balaban, A. E.***, Ferguson, D. J. P.*, Patzewitz, E., Wall, R. J., Hopp, C. S., Poulin, B., Mohmmed, A., Malhotra, P., Coppi, A., Sinnis, P., Tewari, R. (2014). The repeat region of the circumsporozoite protein is critical for sporozoite formation and maturation in *Plasmodium*. *PLoS One, 9*(12), e113923 (*Co-first author).

10) Hopp, C.S., **Balaban, A. E.,** Bushell, E., Billker, O., Rayner, J. C., & Sinnis, P. (2016). Palmitoyl transferases have critical roles in the development of mosquito and liver stages of *Plasmodium*. *Cellular Microbiology, 18*(11), 1625-1641.

11) Pal, P., **Balaban, A. E.**, Diamond, M. S., Dorsey, D., Sinnis, P., Klein, R. S., & Goldberg, D. (2017). *Plasmodium falciparum* histidine-rich protein II causes vascular leak and exacerbates experimental cerebral malaria in mice. *PLoS One*, *12*(5), e0177142.

12) **Balaban, A. E.,** Neuman, K., Sinnis, P., & Balaban, R. S. (2018) Robust fluorescent labeling of micro-pipettes for use in fluorescence microscopy: application to the observation of a mosquito borne parasite infection. *Journal of Microscopy, 269*(1), 78-84.

In Submission

13) Flores, Y., Nasir, N., Hopp, C., Munoz, C., **Balaban, A.**, Zavala, F, & Sinnis, P. Protective antibodies against *Plasmodium* sporozoites have their greatest impact on sporozoites at the inoculation site.

In Preparation

14) Poti, K. E., **Balaban, A. E.,** Pal, P., Goldberg, D., Sinnis, P., & Sullivan, D. Investigating the kinetics of transgenic *Plasmodium falciparum* HRP2 protein produced by *Plasmodium berghei* in a novel murine model.

15) Vega-Rodriguez J., **Balaban, A. E.,** Radtke, A., Huang, W., Kizito, C., Germain, R., Sinnis, P., & Jacobs-Lorena, M. Malaria sporozoites hijack the fibrinolytic proteins to infect the host.

16) **Balaban, A. E.,** Shears, M., Vartak, N., Sinnis-Bourozikas, A., & Sinnis, P. The repeat region of the circumsporozoite protein has a functional role in sporozoite infectivity.

Presentations

Talks

1) **Balaban, A. E.,** & Fried, B. (2012, Mar.). *Infection of neonatal* Biomphalaria glabrata *with* Echinostoma caproni *miracidia*. Pennsylvania Academy of Science Conference, Allentown, PA.

2) **Balaban, A. E.,** Balaban, R. S., & Sinnis, P. (2016, Apr.). *Elucidating the function of the repeat region of the circumsporozoite protein*. Johns Hopkins Malaria Research Institute Seminar Series, Baltimore, MD.

3) **Balaban, A. E.,** & Sinnis, P. (2016, May). *The repeat region of circumsporozoite protein and sporozoite motility and infectivity*. EMBL Conference - Biology of the Malaria Parasite, Heidelberg, Germany.

4) **Balaban, A. E.,** & Sinnis, P. (2016, Sept.). *Elucidating the function of the malaria vaccine target: while surviving grad school*. Lafayette College (Invited Speaker), Easton, Pennsylvania.

5) **Balaban, A. E.,** Balaban, R. S., & Sinnis, P. (2016, Oct.). *Imaging parasite motility using advanced microscopy techniques.* Tropical Medicine Dinner Club (Invited Speaker), Baltimore, MD.

6) **Balaban, A. E.,** Balaban, R. S., & Sinnis, P. (2016, Nov.). *Elucidating the function of the circumsporozoite protein repeat region for sporozoite motility*. Future of Malaria Research Symposium, Rockville, MD.

7) **Balaban, A. E.,** Vartak, N., Sinnis-Bourozikas, A., & Sinnis, P. (2017, Nov.). *Repeat region of the circumsporozoite protein has a functional role in sporozoite motility*. Future of Malaria Research Symposium, Baltimore, MD.

Posters

1) **Balaban, A**., Glushakova, S., Miller, J., & Zimmerberg, J. (2010, Aug.). *New stages in the program of malaria parasite egress imaged in normal and sickle erythrocytes.* NIH Summer Research Program Poster Day, Bethesda, MD.

2) **Balaban, A**., Glushakova, S., Miller, J., & Zimmerberg, J. (2011, Aug.). *The end of the malaria parasite cycle in sickle erythrocytes has a well-masked defect.* NIH Summer Research Program Poster Day, Bethesda, MD.

3) **Balaban, A. E.,** Patzweitz, E., Poulin, B., Hopp, C., Coppi, A., Tewari, R., & Sinnis, P. (2013, Sept.). *Phenotype of* Plasmodium berghei *circumsporozoite protein mutants in the investigation of the role of the central repeat region*. Molecular Parasitology Meeting, Woods Hole, MA.

4) **Balaban, A. E.,** & Sinnis, P. (2015, Jul.). *Elucidating the function the repeat region of the circumsporozoite protein*. FASEB – Microbial Pathogenesis: Mechanisms of Infectious Disease, Keystone, CO.

5) **Balaban, A. E.**, Vartak, N., Sinnis-Bourozikas, A., Shears, M., Sinnis, P. (2017, Apr.). *Repeat region of the circumsporozoite protein has a functional role in sporozoite motility.* World Malaria Day: Vaccine Symposium, Baltimore, MD.

6) **Balaban, A. E.**, Vartak, N., Sinnis-Bourozikas, A., Shears, M., Sinnis, P. (2017, June). *Repeat region of the circumsporozoite protein has a functional role in sporozoite motility.* GRC: Cell Contact and Adhesion, Andover, NH.

Reviewer

- Winter/Spring 2016 for eLIFE - malaria paper
- Winter 2017 for Journal of Microscopy –imaging of mosquitoes

Teaching Experiences

- **Teaching Assistant, General Biology Lab,** *Lafayette College*, Easton, PA **Fall 2009- 2012**
  Undergraduate level teaching. Assisted students with their introductory biology lab. Responsibilities included assistance with concepts and laboratory assignments, holding review sessions before practicals, and grading of assessments.
- **Direct Laboratory Mentor,** *Johns Hopkins School of Public Health*, Baltimore, MD **Spring 2014-Present**
  Mentored three master's students and two undergraduate students on laboratory projects and served as a general source for mentorship for all students in the lab.

Leadership Positions

- **President, Department (MMI) Student Group** (2013-2014)
- **Conference Organizer** (Oct. 23rd, 2015)
- **Student-Faculty Liaison** (2015-2016)
- **Board Member: Tropical Medicine Dinner Club** (2016-Present)

Grants and Fellowships

Travel Grant: Wellcome Trust - Malaria Experimental Genetics Course (Cambridge, England). March, 2014
Travel Grant: Johns Hopkins Student Association Travel Fund – 2015
Travel Grant: FASEB - Molecular Pathogenesis: Mechanisms of Infectious Disease (Keystone, Colorado), July 2015
JHMRI Pre-doctoral Fellowship: January 2016 – January 2018

Association Membership

American Society for Microbiology (ASM): (2012-Present)
Johns Hopkins Malaria Research Institute (JHMRI): (2012-Present)
Tropical Medicine Dinner Club: (2012-Present)

References

Photini Sinnis
Bloomberg School of Public Health
615 N. Wolfe St.
Suite E4626
Baltimore, MD 21205
410-502-6918
psinnis1@jhu.edu

Fidel Zavala
Bloomberg School of Public Health
615 N. Wolfe St.
Suite E4630
Baltimore, MD 21205
410-287-1769
fzavala1@jhu.edu

Sean Prigge
Bloomberg School of Public Health
615 N. Wolfe St.
Suite E4628
Baltimore, MD 21205
410-502-6918
sprigge2@jhu.edu